Tunable Surface Hydrophobicity and Fluid Transport through Nanoporous Membranes

by

Joseph H.J. Ostrowski

B.S., University of Minnesota, 2009

A thesis submitted to the

Faculty of the Graduate School of the

University of Colorado in partial fulfillment

of the requirements for the degree of

Doctor of Philosophy

Department of Chemistry and Biochemistry

2014

ProQuest LLC.
789 East Eisenhower Parkway
P.O. Box 1346
Ann Arbor, MI 48106 - 1346

This thesis entitled:
Tunable Surface Hydrophobicity and Fluid Transport through Nanoporous Membranes
written by Joseph H.J. Ostrowski
has been approved for the Department of Chemistry and Biochemistry

_____

Joel D. Eaves

_____

Robert P. Parson

Date _____

The final copy of this thesis has been examined by the signatories, and we find that both the content and the form meet acceptable presentation standards of scholarly work in the above mentioned discipline.

Ostrowski, Joseph H.J. (Ph.D., Chemical Physics)

Tunable Surface Hydrophobicity and Fluid Transport through Nanoporous Membranes

Thesis directed by Joel D. Eaves

There are more than three billion people across the globe that struggle to obtain clean drinkable water. One of the most promising avenues for generating potable water is through reverse osmosis and nanofiltration. Both solutions require a semipermeable membrane that prohibits passage of unwanted solute particles but allows passage of the solvent. Atomically thin two-dimensional membranes based on porous graphene show great promise as semipermeable materials, but modeling fluid flow on length scales between the microscopic (nanometer and smaller) and macroscopic (micron and larger) regimes presents formidable challenges. This thesis explores both equilibrium and nonequilibrium aspects of this problem and develops new methodology for simulating systems away from thermal equilibrium.

First, we hypothesize that there is a wetting penalty for water as it tries to breach a sheet of graphene that should be naturally hydrophobic. By using equilibrium molecular dynamics simulations, we show that the hydrophobicity depends sensitively on the degree of electrical doping, offering an opportunity to tune the hydrophobic effect of graphene using small amounts of doping. The wetting contact angle, a measure of hydrophobicity, changes dramatically with the voltage applied to single layer graphene. We find that the sensitivity of the hydrophobic effect to voltage depends not on hydrogen bonding motifs at the interface between graphene and water, but instead on a phenomenon known as electrowetting. The theory of electrowetting predicts that the difference in surface tensions that defines the contact angle is quartic in the voltage, rather than quadratic, as it would be in bilayer graphene or in a two-dimensional metal.

To explore the nonequilibrium aspects of fluid passage through atomically thin membranes, we developed a molecular dynamics methodology for simulating fluid flow at constant flux based on Gauss's principle of least constraint. This method develops microscopic equations of motion

that satisfy specified constraints on the kinetic temperature and total mass flux. As a proof of principle, we simulate the flow of a simple monoatomic fluid and observe emergent and collective behaviors consistent with both known hydrodynamic solutions and expectations for velocity distributions from statistical mechanics. We compare results from the Gauss method simulations with that of a method commonly used in the literature. By computing the relationship between the pressure drop across a pipe-like region and the fluid current through it, we find that these two methods agree quantitatively with one another and comment on the advantages and disadvantages for both methods.

Acknowledgements

My education in the sciences birthed from a general inquisitiveness for the universe around us. My academic journey through my undergraduate and graduate careers has not satisfied this inquisitiveness, as luckily, there are too many interesting things to see and study. The universe is composed of extraordinary phenomenon and extraordinary people.

I would like to thank Joel Eaves and his research group for their conversations about science and life during graduate school. In particular, I would like the thank Dr. Mark Sweeney and Paul Teichen. They were always available to discuss any and all science, even if it wasn't related to the projects they were currently working on.

I thank the Department of Chemisty and Biochemistry for the opportunity to teach and conduct research at the University of Colorado at Boulder. When interacting with students, one inevitably learns something more about the subject matter, or at the least walks away with an appreciation for different perspectives brought to light from conversations with students.

Lastly I would like to thank my family for their never ending support. My mother and father, Darlene and George, have always supported me in my academic adventures. Never have they pushed me to think about this or that, but have simply allowed me to carry life out as I see fit. I am thankful to my brother Tom, for his support, and for his companionship in childhood when we would wade through the creeks, looking for creatures we had not yet seen. I am still looking for things I haven't seen, I just have to search a little harder.

Contents

Chapter

Tables

Table

Figures

Figure

Chapter 1

Introduction

In the coming years, the world will be faced with shortages of potable water on a massive scale.[19;21;60] Collecting clean drinkable water is particularly a challenge due to current strain on the limited freshwater resources across the globe. Desalination of seawater involves separating water from salt ions and other unwanted particulates or molecules typically using nanoporous membranes to obtain potable water.[8;12;20;60]

Membranes with nanoscopic pores can separate unwanted solutes from gases or liquids.[2;30;41] In its simplest form, nanoporous semipermeable membranes operate by size exclusion, prohibiting passage of solute particles based on particle or molecular size while still allowing passage of solvent particles.[29] The efficiency of a membrane to purify a fluid or gas is intimately determined by the size of the nanopore relative to the size of the solute and solvent molecular dimensions. Fluid behavior near the surface of membranes and inside nanopores or nanochannels is also determined by interactions between fluid molecules or particles with the membrane. Fluid-membrane interactions could be specific to the functionalization around the entrance of a nanopore,[50] or particular to the surface of the material.[23] We are interested in atomically thin membranes because of their potential utility in nanofiltration applications and unique surface properties. In this thesis we will focus on both the equilibrium and nonequilibrium properties of thin membranes.

What causes a surface to be hydrophobic? It has been shown that the liquid-solid interface is distinct from that of a liquid-vapor interface in the case of water near a solid substrate.[9;57;58] The hydrogen bond between oxygen and hydrogen in water is approximately six times the avail-

able thermal energy at room temperature.[17] Altering surface composition or properties can start to compete with the hydrogen bonding network within water.[58] However, we will show in Chapter 2 that in the case of electrodoping a graphene surface the main contribution to surface hydrophobicity is due to a collective effect known as electrowetting.[40]

According to the predictions of hydrodynamics, the rate of fluid mass flow through a semipermeable membrane is inversely proportional to the thickness of the membrane,[13;33] making atomically thin materials advantageous for filtration purposes. A balance must be struck between the percentage of solute exclusion and the amount of fluid throughput desired for a given application. If the nanopore is too large, both the solute and solvent may pass freely through the nanopore. In the other extreme, if the nanopore is too small neither the solute or solvent may pass through the nanopore, and very little to no purified solvent can be obtained.[10;25]

Water desalination is one of the most important applications of nanoporous membranes.[39;50] However, in modern desalination plants it is difficult to maintain a high level of salt exclusion while still retaining a high production rate of water.[14;19] Despite the worldwide interest in developing thin semipermeable membrane technologies for the purposes of desalinating seawater as well as other applications, room remains for making significant contributions through the use of models of fluid flow through nanoscopic channels and pores.

There are two primary issues pertinent for simulating and modeling nonequilibrium mass transport through nanopores. The first pertains to relevant time and length scales. Results from continuum hydrodynamics start to break down for fluid flow through small nanochannels with widths on the order of several molecular diameters.[53] This is not surprising because a continuum description does not apply to the limiting case where single fluid molecules or particles occupy a nanochannel. Continuum theories require mild oscillations in quantities such as the density and pressure. On the microscopic scale this will not be the case for fluids near a membrane. Describing both continuum-like fluid properties and nanoscopic dynamics is therefore beyond the scope of continuum theory, but well suited to molecular dynamics simulations. In these simulations the fluid is modeled as a collection of discrete particles, whose motion is propagated according to the

numerical integration of Newton's equations of motion.[18]

The second issue pertains to details of simulating a fluid flow. Flow of a fluid is a nonequilibrium process. The fluid has a net mass transport in a given direction because of some type of gradient. This gradient could be in the density, pressure, temperature, or chemical potential. Maintaining fluid flow in molecular dynamics simulations is nontrivial. In the case of a fluid flowing through a membrane, fluid collisions with the membrane dissipate momentum from the fluid. In order to maintain fluid transport, an external driving force must be applied. Applying an external driving force to the simulation requires the use of a thermostat to act as a heat bath.[15] However, it is unclear how equilibrium-thermostats interact with out-of-equilibrium driving forces in molecular dynamics simulations.[5]

We have developed a methodology for simulating nonequilibrium flow through a semipermeable membrane using Gauss's principle of least constraint (Chapter 3). We have computed the flow of a Lennard-Jones fluid through a pipe-like region. Our results show that the behavior of the fluid agrees well with that predicted by from continuum hydrodynamics[13;31] and with expectations for velocity distributions from statistical mechanics.[34]

1.1 Nonequilbrium Fluid Flow

Motivated by applications to water desalination, we will first discuss the basic principles of reverse osmosis. This discussion will further motivate the role of membrane geometry and surface properties. We will also discuss current simulation methodology and the necessity of developing an alternative method for maintaining nonequilibrium fluid flow in simulations.

1.1.1 Reverse Osmosis With Semipermeable Membranes

The desalination of saltwater requires isolation of water from a source of varying salinity, typically seawater or coastal ground water, the latter of which is also termed brackish water.[19;24;29] The semipermeable membrane ideally allows passage of water molecules while restricting passage of salt ions such as Ca^{2+}, Mg^{2+}, K^{+} based on solvated ion size.[19;24] The problem therefore remains

to somehow force the water to leave the side of the membrane with a high concentration of salt ions, typically called the feed source, to the other side where pure water can be obtained.

As an example, consider a saltwater feed source on one side of a semipermeable membrane, with a pure water solution on the other side (Figure 1.1). The unequal ion concentrations on the two sides of the membrane cause a gradient in the chemical potential of the solvent, water, between the two sides. The entropy due to mixing of the salt ions with water lowers the chemical potential on the feed-source side of the membrane.[1;34]

When a pressure is applied to the feed source side of the membrane (Figure 1.1), the chemical potential is raised on this side of the membrane. The pressure at which the chemical potentials for each side of the membrane are equal is known as the osmotic pressure.[19] If the applied pressure is equal to the osmotic pressure, no water will flow and the system is at equilibrium with no net flow of water through the membrane in either direction. For pressures above the osmotic pressure, the chemical potential of the feed source reservoir is larger than the pure water reservoir. Again the system moves to minimize the chemical potential difference, but in the case of an applied pressure, water flows through the semipermeable membrane from the feed source solution to the pure water side. This process is known as reverse osmosis, and can be used to isolate water from a source of salt solution.[12;19;21;24]

The higher the salt concentration, the higher the osmotic pressure required to achieve reverse osmosis.[19;24] The pressure required to achieve reverse osmosis depends on the water feed source. Seawater sources typically require applied pressures of $55 - 65$bar, and brackish water sources require pressures of $10 - 15$bar.[19]

One can use thermodynamic arguments to estimate the theoretical minimum cost in energy for water desalination. Equating the chemical potentials of the solvent on both sides of Figure 1.1 leads to the van't Hoff equation for the osmotic pressure of an ideal solution.[48] The osmotic pressure, Π, for an ideal solution is

$$\Pi = \nu MRT \tag{1.1}$$

where ν is the van't Hoff factor, which for NaCl is ≈ 2, M is the concentration in moles of solute per liter of solvent, R is the ideal gas constant, and T is the temperature. For a salt solution concentration of 35 g/L, the osmotic pressure is approximately 30 bar. Provided the work is done at constant pressure and the van't Hoff equation holds throughout, the cost for desalination is approximately 1 kWh/m^3 of water. Desalination plants using reverse osmosis reach efficiencies around 7 kWh/m^3.[19*] Assuming an average cost of electricity of 15 $¢/kWh$, and assuming that an average family of four uses 1.5 m^3 of water per day, in a year the ideal solution estimated cost is approximately \$700, compared to current desalination plant cost of nearly $\$5,000$.

Hagen-Poiseuille's law from continuum hydrodynamics predicts that the volumetric flow rate of water through a pipe scales linearly with the pressure and inversely with the membrane thickness.[3;33] Importantly, this means that the thinner the membrane, the smaller the required applied pressure to achieve a given volumetric flow rate. Therefore, we are primarily interested in atomically thin membranes. Thin membranes are particularly interesting because their degree of hydrophobicity can be easily altered, as we will discuss next.

* This cost is taken for the highest salinity data pertaining to seawater feed sources.[19]

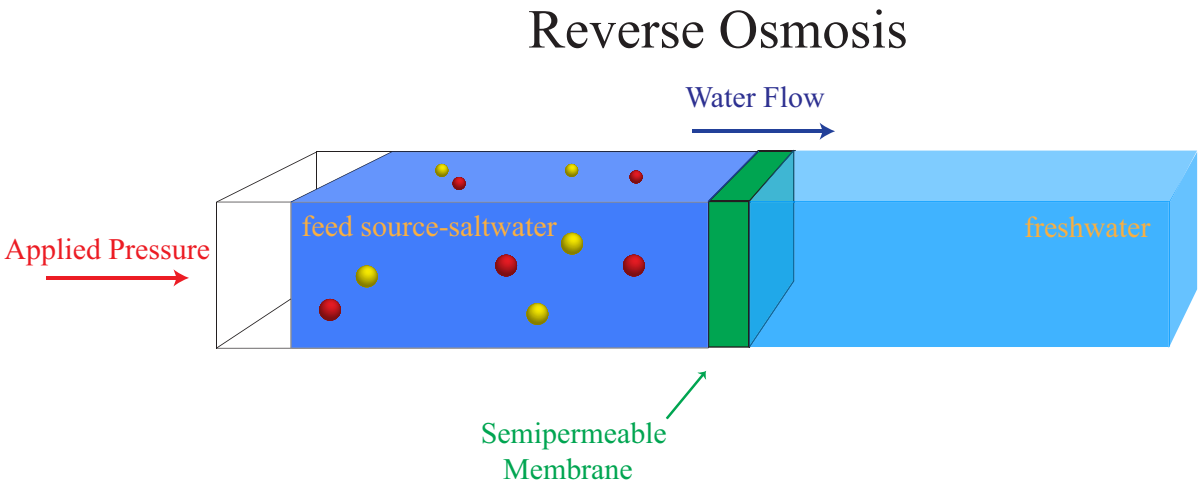

Figure 1.1: Reverse osmosis. To desalinate water, a nanoporous semipermeable membrane may be used to restrict passage of the solute thereby allowing purification of the fluid. The entropy of mixing salt ions with water lowers the chemical potential.[1;34] The feed source with the higher concentration of salt ions therefore has a lower chemical potential than the side with predominantly pure water. When a pressure is applied to the feed saltwater solution, the chemical potential of the salt solution increases. The pressure at which the chemical potentials for the two solutions on each side of the membrane are equal is termed the osmotic pressure.[19] For applied pressures greater than the osmotic pressure, water flows from the high salinity side to the low salinity side, as required for water purification purposes. This process is known as reverse osmosis.[19;24] The figure was adopted from Reference 19.

1.1.2 Simulating Fluid Passage

Nanofluidic flow through nanopores is in a regime between the macroscopic ($\gtrsim \mu$m) and the microscopic ($\lesssim$nm).[42] Continuum theories applicable on the macroscopic length scale, such as the Navier-Stokes equations, require that fluctuations in density and pressure be mild, and can therefore not be expected to hold on atomic length scales.[6] We present a methodology capable of describing fluid in both the atomistic and macroscopic regimes (Figure 1.2).[27;35;54]

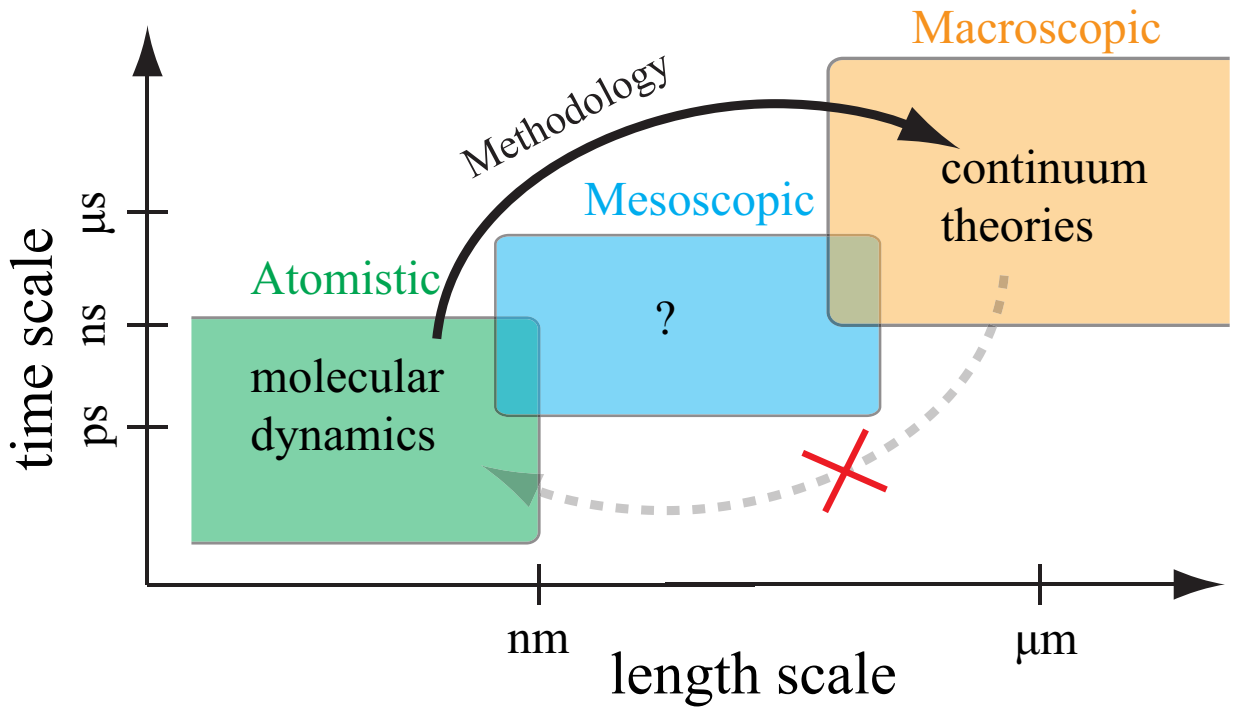

Figure 1.2: Fluid dynamic models for various time and length scales. Continuum theories can be applied on macroscopic length scales on the order of a micrometer. Due to current computational limitations, atomistic simulations can be applied to system sizes with a length scale on the order of a nanometer. Macroscopic continuum theories require mildly varying densities and therefore are not applicable to systems on the atomistic length scale. We will develop an atomistic methodology that, given large enough length scales, will give results commensurate with continuum theories.

While linear response theories can connect calculations in equilibrium simulations to transport phenomena close to equilibrium,[61] in practice they average poorly for water passage when pores are on the order of a nanometer. Thus, to simulate fluid flow in these systems, one needs

an appropriate methodology away from equilibrium. In a typical molecular dynamics simulation, one solves Newton's equation of motion at fixed energy, volume, and number of particles.[18] This connects to the microcanonical ensemble in statistical mechanics.[34] To perform simulations at constant temperature, one has to couple the microscopic system to a heat bath.[15] While there are several different ways to do this, one can show that any reasonable protocol generates the canonical distribution at equilibrium. An external force must drive a system away from equilibrium. In addition, to achieve a steady state, one must also dissipate energy. The way that heat baths, or thermostats, couple to a system away from equilibrium is poorly understood. Naïve applications of the equilibrium thermostats, for example, give rise to a number of erroneous and spurious behaviors.[5;16]

In molecular dynamics simulations an external force is used to drive the system and maintain fluid flow. One of the most common methods used for inducing flow of a fluid through a nanochannel uses a piston placed on one side of the simulation box (Figure 1.3A).[11;51] The piston is treated as a rigid wall of particles impenetrable to fluid particles. A constant force is applied to the piston wall which thereby exerts a force onto the fluid. The fluid will exert a force back on the piston due to interatomic interactions between the fluid particles and the particles composing the piston wall. As long as the force applied to the piston is large enough, the piston compresses the fluid and moves towards the center of the simulation box by forcing fluid particles through the membrane. The compressing piston has the effect of creating a pressure gradient across the membrane, thereby driving flow of the fluid particles from one side of the membrane to the other.

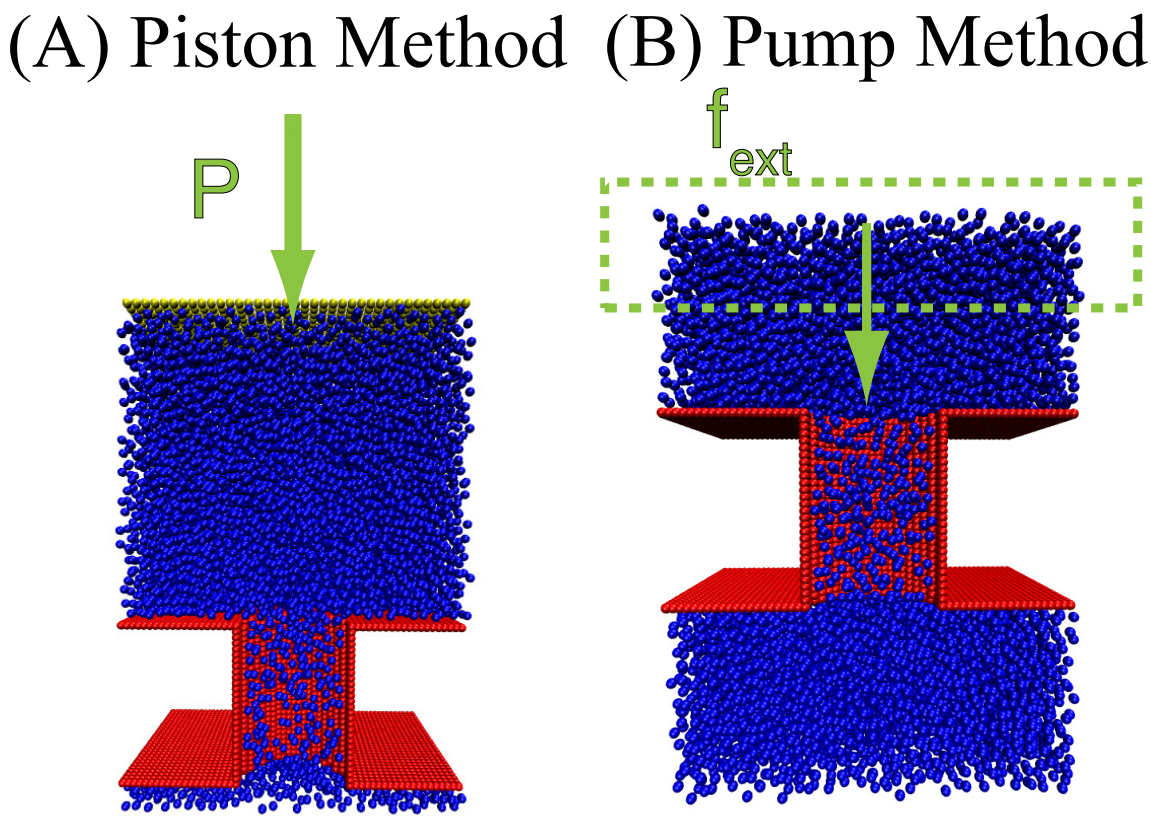

Figure 1.3: Piston and pump methods for simulation of nonequilibrium fluid flow through a nanopore. (A) A piston composed of a wall of particles is placed on one end of the simulation box. A constant pressure, P, is applied to the rigid piston wall which thereby exerts a force on the fluid and pressure gradient across the membrane. The fluid flows through the membrane until the piston depletes the reservoir of fluid particles. The simulation is nonperiodic for the dimension in the direction of fluid flow. (B) A pump region is defined away from the membrane. An external force, $\mathbf{f}_{ext}$, is applied to particles occupying the pump region that drives fluid flow through the membrane.

The piston method, while it seems to relatively work well in practice,[11;51] suffers from the deficit that it cannot be used to continually collect data because of the nonperiodicity in the direction of flow. For long enough simulation times, the piston will eventually reach the membrane, i.e. the fluid reservoir on the high pressure side of the membrane will eventually be depleted. The volume of fluid on the high pressure side of the simulation changes throughout the course of the

simulation. As a steady-state flow of fluid particles develops, fluid velocity streamlines develop near the entrance and exit of the nanochannel. For large enough fluid flow, the fluid velocity streamlines can extend well into the fluid reservoirs on either side of the nanochannel (see e.g. Figure 3.4). As the size of the fluid reservoir decreases, the piston will begin to enter the volume occupied by these velocity streamlines, and could affect passage dynamics in an uncontrolled manner.

Another common method used to create a steady-state nonequilibrium fluid flow defines a pump region, typically defined to be near the edge of one end of the simulation box.[28;49;50;62] Particles occupying the pump region are subjected to an additional constant force (Figure 1.3B). This method will be referred to as the "pump" method. We will compare simulations using the pump method to the nonequilibrium method developed in chapter 3. The pump method, in contrast to the piston method discussed above, allows for periodic boundaries in all dimensions and avoids the complication of a decreasing fluid reservoir volume in the piston simulations.

Particles entering or exiting the pump region experience a discontinuity in potential due to the external force added when particles occupy the pump region. Near the pump region, this means that particle motion is not time-reversible. However, if the pump region is far from the nanochannel, it is reasonable to assume that this is inconsequential to fluid behavior inside and near the channel, and that a steady-state local equilibrium can be assumed away from the pump region.

One advantage of the pump method is that it allows for periodic boundaries in all dimensions, in contrast to the piston method. However, fluid flow inside the channel is not totally independent of the pump region size.[28] One must prescribe the width of the region and its distance away from the membrane. The method that we will develop in chapter 3 avoids prescribing any artificial regions.

In Chapter 3, we develop a methodology for simulating nonequilibrium steady states based on microscopic equations of motion. We will include a constraint on the total flow of the fluid into the equations of motion using Gauss's principle of least constraint. We will compare results from our Gauss method with those of the pump method for pipe-like simulations. Importantly, we will

show that both methods give results commensurate with that expected from continuum predictions while maintaining velocity distributions from statistical mechanics. Our method will simulate nonequilibrium fluid flow with minimal parameter input. Local velocity profiles will develop in response to the fluid-membrane interactions and the pipe-like geometry. This will allow for further exploration of fluid flow through nanoscopic channels as a function of fluid-surface interactions. Future studies will be able to easily explore the role of membrane functionalization or surfaces with varying hydrophobicity.

1.2 Equilibrium Studies of Surface Hydrophobicity

Surface hydrophobicty as it applies to semipermeable membrane applications remains to be investigated. Changing the hydrophobicity of a surface has additional applications ranging from electronic displays to so-called "lab-on-chips," that move various materials around a circuit based on alterations to the solid-liquid interface.[37] Applications such microfluidic circuits and electronic displays require surfaces capable of modifying liquid-surface hydrophobicity "on-command."[4;26;56] In chapter 2 we will focus on the liquid-solid interface between that of water and graphene. We show that the degree of hydrophobicity changes dramatically upon electrostatic doping. The same ideas and discussion should be applicable to a wide range of other systems.

1.2.1 Characterizing Hydrophobicity

Surface hydrophobicity is commonly altered using either chemical modifications[23;45] or electrowetting on dielectrics.[36;38;52] Experiments and simulations typically measure surface hydrophobicity in terms of the contact angle.[7;23;43] The contact angle, θ, is the angle at which the fluid meets a solid surface (Figure 1.4).[59] At equilibrium, the contact angle is described by Young's equation,[44;59]

$$cos\theta = \frac{\gamma_{SV} - \gamma_{SL}}{\gamma_{LV}} \tag{1.2}$$

where $\gamma_{SV}, \gamma_{SL}, \gamma_{LV}$ are the solid-vapor, solid-liquid, and liquid-vapor surface tensions respectively. The various surface tensions correspond to the energy required to alter the surface area between the two corresponding phases. The liquid-solid and solid-gas surface tensions and thereby the contact angle change upon alteration of the solid surface properties. Fluid contact angles greater than 90 degrees are considered hydrophobic. Contact angles greater than 120 degrees are termed superhydrophobic, and anything less than 90 degrees is considered nonhydrophobic or wetting.[32;55]

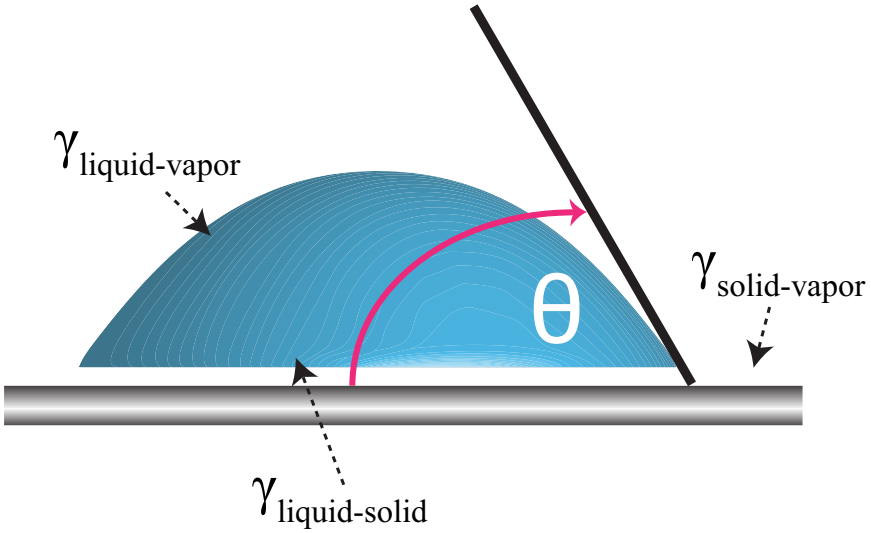

Figure 1.4: Definition of the contact angle, θ, to measure hydrophobicity. The contact angle is the angle at which the fluid meets the solid surface. The contact angle is a function of the surface tensions $\gamma_{SV}, \gamma_{SL}, \gamma_{LV}$, the solid-vapor, solid-liquid, and liquid-vapor surface tensions respectively. At equilibrium, the contact angle is described by Young's equation, Equation (1.2).

The surface tensions can be thought of as quantifying the intermolecular interactions between the various phases. If the solid-liquid interactions are modified such that γ_{SL} is minimized, the right-hand side of Young's equation is maximized, and $cos\theta$ is large (θ approaches a minimum). In this situation, the energy penalty for the fluid droplet to spread is minimized and the fluid disperses over the surface of the solid. In the other extreme, if the solid-liquid interactions become unfavorable and γ_{SL} becomes large, the right-hand side of Young's equation is minimized, and θ

becomes large. In this case the fluid droplet becomes extremely hydrophobic and avoids contact with the solid surface.

1.2.2 Methods of Modifying Surface Hydrophobicity

As mentioned above, the extent of fluid hydrophobicity on a surface is intimately determined by the type and magnitude of the interactions between a solid and the fluid.[9] As we will discuss, the hydrophobicity of a solid surface is not determined only by those interactions near a solid-liquid interface, but is instead a collective effect (Chapter 2). Two primary methods for altering the hydrophobicity of a liquid-solid interface are through chemical modification[23;45] and electrowetting.[7;22;36;52;56]

Chemical functionalization has been shown to change the hydrophobicity of surfaces dramatically.[23;46;47] Godawat et al. studied the wetting properties of self-assembled alkane-thiol monolayers functionalized using a variety of polar and nonpolar functional groups. The contact angle varies over a wide range depending on the surface modification (Figure 1.5). As expected from physical intuition, the polar functional groups caused water to spread out over the surface of the monolayer. As discussed above, if the liquid-solid surface tension is minimized, the fluid will spread out over the solid surface. In this case, the favorable Coulomb interactions between the polar head group of the solid layer and water lower the surface tension and decrease hydrophobicity. Similarly, nonpolar functional groups cause water to minimize its surface area nearest the monolayer, and form a water droplet due to the lack of favorable interactions with the surface.

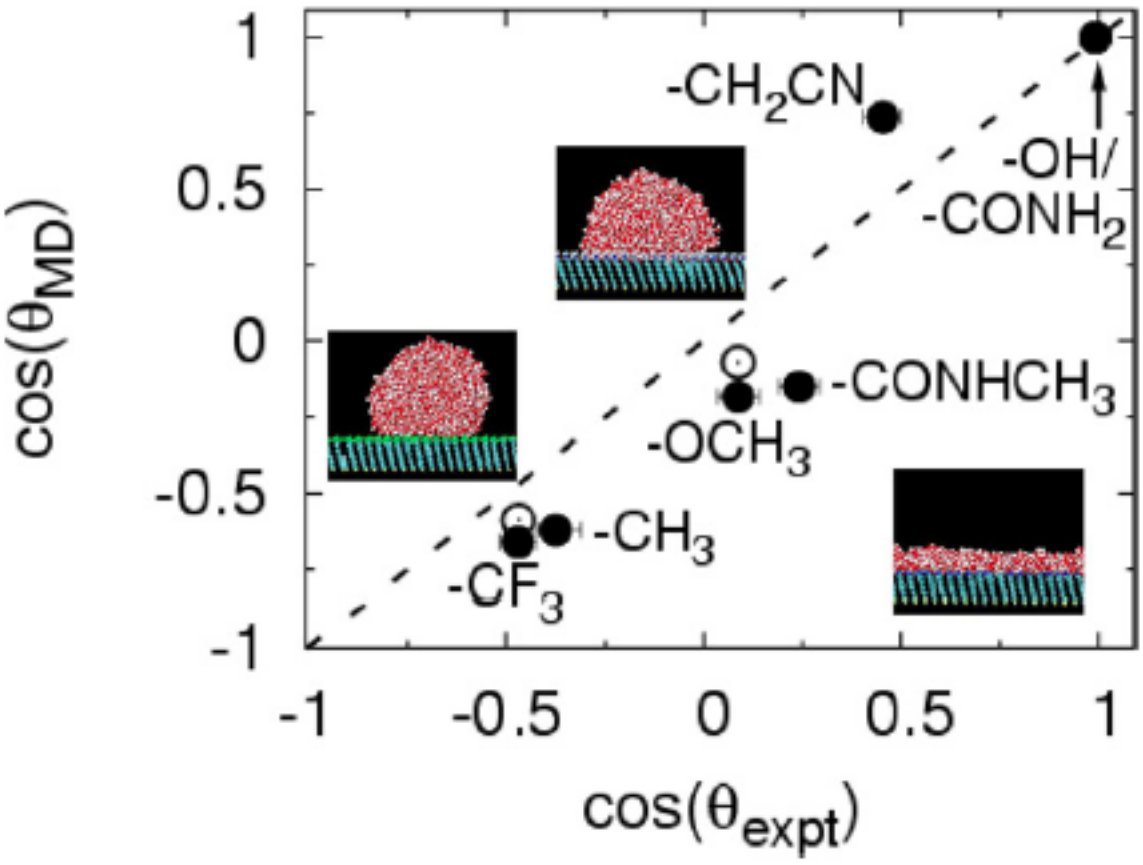

Figure 1.5: Altering hydrophobicity of an alkane-thiol surface via chemical modification. The contact angle, which quantifies the degree of hydrophobicity, from simulations (θ_{MD}) and experiments (θ_{expt}) are compared. The polar functional groups cause water to wet the solid surface. Nonpolar functionalization of the surface causes water to minimize its surface area on the solid, causing the water to "bunch up", and form a droplet. Figure from Reference 23. Molecular dynamics simulation and experimental data are taken from References 46 and 47 respectively. The open circles are for droplets with a diameter of $\approx$ 5Å, and the filled circles are for droplets in the macroscopic limit.[23]

While the hydrophobicity of a surface can be altered dramatically using chemical functionalization, it suffers from the limitation that once the surface is prepared it is not easily altered thereafter. Additionally, the degree of hydrophobicity is limited by the types of chemistry possible at the interface, i.e. there are only so many types of functional groups that can be added to a given surface, and therefore only so many different levels of hydrophobicity obtainable. Electrowet-

ting, whereby an applied electric field induces changes in wetting properties, excels at achieving a greater tunability of hydrophobic character.[36–38]

In chapter 2 we present a method whereby we take advantage of the electronic density of states for graphene. Applying a voltage to the two-dimensional lattice of carbon atoms places an excess amount of negative (n-doped) or positive (p-doped) charge on the carbon atoms. We show that the contact angle and extent of hydrophobicity for water on graphene changes dramatically upon electrical doping. The results are shown to be consistent with a modified version of Young's equation describing electrowetting.

1.3 Organization of the Thesis

Chapter 2 presents the hydrophobicity of graphene with applied electrostatic voltage. Electrodoping graphene is a tunable means to alter the wetting properties of the graphene surface. The wetting contact angles for water droplets on monolayer graphene were calculated using molecular dynamics under various applied voltages between ±1/3 volt. Using the low-energy and low-temperature limits for the density of electronic states in monolayer graphene, excess discrete partial charge was placed on the carbon atom centers. The contact angle of the water droplet on monolayer graphene follows closely a modified Young-Lippmann equation that describes the contact angle of a droplet on a surface in an applied electric field. Our simulations agree with our prediction that the contact angle of water on graphene scales quartically with the voltage.

In chapter 3 a nonequilibrium method of simulating fluid flow through a nanopore is presented. Using Gauss's principle of least constraint, the total flow of a fluid was held constant throughout molecular dynamics simulations of fluid passage through a channel. Using the proposed method, a fluid and channel system modeled with Lennard-Jones particles was studied for two pipe-like configurations. We found that the developed method gives similar results to those observed for a pump method commonly used in the literature,[28;49;50;62] whereby an additive force is applied to fluid particles near the edge of the simulation box. Both simulation methods give results commensurate with Hagen-Poiseuille's law for the fluid velocity profile and maintain the

Maxwell-Boltzmann distribution of velocities.

Bibliography

[1] P. W. Atkins and J. De Paula. Physical chemistry. Oxford University Press, Oxford, 1994.

[2] L. A. Baker and S. P. Bird. Nanopores: A makeover for membranes. Nat. Nanotechnol., 3(2):73–74, 2008.

[3] C. O. Bennett and J. E. Myers. Momentum, heat, and mass transfer. McGraw-Hill New York, 1982.

[4] B. Berge and J. Peseux. Variable focal lens controlled by an external voltage: An application of electrowetting. Eur. Phys. J. E, 3(2):159–163, 2000.

[5] S. Bernardi, B. Todd, and D. J. Searles. Thermostating highly confined fluids. J. Chem. Phys., 132(24):244706, 2010.

[6] M. K. Borg, D. A. Lockerby, and J. Reese. Coupled continuum hydrodynamics and molecular dynamics method for multiscale simulation. In 3rd Micro. Nano Flows Conf., MNF11, 2011.

[7] D. Bratko, C. D. Daub, K. Leung, and A. Luzar. Effect of field direction on electrowetting in a nanopore. J. Am. Chem. Soc., 129(9):2504–2510, 2007.

[8] T. Y. Cath, A. E. Childress, and M. Elimelech. Forward osmosis: principles, applications, and recent developments. J. Membr. Sci., 281(1):70–87, 2006.

[9] D. Chandler. Hydrophobicity: Two faces of water. Nature, 417(6888):491–491, 2002.

[10] D. Cohen-Tanugi and J. Grossman. Water desalination across nanoporous graphene. Nano Lett., 12(7):3602–3608, 2012.

[11] D. Cohen-Tanugi and J. C. Grossman. Water permeability of nanoporous graphene at realistic pressures for reverse osmosis desalination. J. Chem. Phys., 141(7):074704, 2014.

[12] D. Cohen-Tanugi, R. K. McGovern, S. H. Dave, J. H. Lienhard, and J. C. Grossman. Quantifying the potential of ultra-permeable membranes for water desalination. Energy Environ. Sci., 7(3):1134–1141, 2014.

[13] W. M. Deen. Analysis of transport phenomena, volume 3. Oxford University Press, New York, 1998.

[14] M. Elimelech and W. A. Phillip. The future of seawater desalination: energy, technology, and the environment. Science, 333(6043):712–717, 2011.

[15] D. J. Evans and B. L. Holian. The nose–hoover thermostat. J. Chem. Phys., 83(8):4069–4074, 1985.

[16] D. J. Evans and G. P. Morriss. Shear thickening and turbulence in simple fluids. Phys. Rev. Lett., 56(20):2172, 1986.

[17] M. W. Feyereisen, D. Feller, and D. A. Dixon. Hydrogen bond energy of the water dimer. J. Phys. Chem., 100(8):2993–2997, 1996.

[18] D. Frenkel and B. Smit. Understanding molecular simulation: from algorithms to applications. Acadmic Press: San Diego, CA, 2001.

[19] C. Fritzmann, J. Löwenberg, T. Wintgens, and T. Melin. State-of-the-art of reverse osmosis desalination. Desalination, 216(1):1–76, 2007.

[20] Q. Ge, M. Ling, and T.-S. Chung. Draw solutions for forward osmosis processes: developments, challenges, and prospects for the future. J. Membr. Sci., 442:225–237, 2013.

[21] A. M. Gilau and M. J. Small. Designing cost-effective seawater reverse osmosis system under optimal energy options. Renewable Energy, 33(4):617–630, 2008.

[22] N. Giovambattista, P. G. Debenedetti, and P. J. Rossky. Effect of surface polarity on water contact angle and interfacial hydration structure. J. Phys. Chem. B, 111(32):9581–9587, 2007.

[23] R. Godawat, S. N. Jamadagni, and S. Garde. Characterizing hydrophobicity of interfaces by using cavity formation, solute binding, and water correlations. Proc. Natl. Acad. Sci. USA, 106(36):15119–15124, 2009.

[24] L. F. Greenlee, D. F. Lawler, B. D. Freeman, B. Marrot, and P. Moulin. Reverse osmosis desalination: water sources, technology, and today's challenges. Water Research, 43(9):2317–2348, 2009.

[25] J. Han, J. Fu, and R. B. Schoch. Molecular sieving using nanofilters: past, present and future. Lab Chip, 8(1):23–33, 2008.

[26] R. A. Hayes and B. Feenstra. Video-speed electronic paper based on electrowetting. Nature, 425(6956):383–385, 2003.

[27] P. Hoogerbrugge and J. Koelman. Simulating microscopic hydrodynamic phenomena with dissipative particle dynamics. Europhys. Lett., 19(3):155, 1992.

[28] C. Huang, P. Y. Choi, and L. W. Kostiuk. A method for creating a non-equilibrium NT(P1-P2) ensemble in molecular dynamics simulation. Phys. Chem. Chem. Phys., 13(46):20750–20759, 2011.

[29] J. Johnson and M. Busch. Engineering aspects of reverse osmosis module design. Desalin. Water Treat., 15(1-3):236–248, 2010.

[30] T. Z. Jubery, A. S. Prabhu, M. J. Kim, and P. Dutta. Modeling and simulation of nanoparticle separation through a solid-state nanopore. Electrophoresis, 33(2):325–333, 2012.

[31] G. Karniadakis, A. Beskok, and N. Aluru. Microflows and nanoflows: fundamentals and simulation, volume 29. Springer, 2006.

[32] A. Lafuma and D. Quéré. Superhydrophobic states. Nat. Mater., 2(7):457–460, 2003.

[33] H. K. Lonsdale. The evolution of ultrathin synthetic membranes. J. Membr. Sci., 33(2):121–136, 1987.

[34] D. McQuarrie. Statistical mechanics. University Science Books: Sausalito, CA, 2000.

[35] E. Moeendarbary, T. Ng, and M. Zangeneh. Dissipative particle dynamics: introduction, methodology and complex fluid applicationsa review. Int. J. Appl. Mech., 1(04):737–763, 2009.

[36] H. Moon, S. Cho, R. Garrell, and C.-J. Kim. Low voltage electrowetting-on-dielectric. J. Appl. Phys., 92(7):4080–4087, 2002.

[37] F. Mugele and J.-C. Baret. Electrowetting: from basics to applications. J. Phys. Condens. Matter, 17(28):R705–R774, 2005.

[38] W. Nelson and C.-J. Kim. Droplet actuation by electrowetting-on-dielectric (ewod): A review. J. Adhes. Sci. Technol., 26(12-17):1747–1771, 2012.

[39] A. Nicolaï, B. G. Sumpter, and V. Meunier. Tunable water desalination across graphene oxide framework membranes. Phys. Chem. Chem. Phys., 16(18):8646–8654, 2014.

[40] J. H. Ostrowski and J. D. Eaves. The tunable hydrophobic effect on electrically doped graphene. J. Phys. Chem. B, 118(2):530–536, 2014.

[41] A. S. Prabhu, T. Z. N. Jubery, K. J. Freedman, R. Mulero, P. Dutta, and M. J. Kim. Chemically modified solid state nanopores for high throughput nanoparticle separation. J. Phys. Condens. Matter, 22(45):454107, 2010.

[42] T. Qian and X.-P. Wang. Driven cavity flow: from molecular dynamics to continuum hydrodynamics. Multiscale Model. Simul., 3(4):749–763, 2005.

[43] J. Rafiee, X. Mi, H. Gullapalli, A. V. Thomas, F. Yavari, Y. Shi, P. M. Ajayan, and N. A. Koratkar. Wetting transparency of graphene. Nat. Mater., 11(3):217–222, 2012.

[44] P. Roura and J. Fort. Local thermodynamic derivation of young's equation. J. Colloid Interface Sci., 272(2):420–429, 2004.

[45] F. Rupp, L. Scheideler, N. Olshanska, M. De Wild, M. Wieland, and J. Geis-Gerstorfer. Enhancing surface free energy and hydrophilicity through chemical modification of microstructured titanium implant surfaces. J. Biomed. Mater. Res., Part A, 76(2):323–334, 2006.

[46] N. Shenogina, R. Godawat, P. Keblinski, and S. Garde. How wetting and adhesion affect thermal conductance of a range of hydrophobic to hydrophilic aqueous interfaces. Phys. Rev. Lett., 102(15):156101, 2009.

[47] G. B. Sigal, M. Mrksich, and G. M. Whitesides. Effect of surface wettability on the adsorption of proteins and detergents. J. Am. Chem. Soc., 120(14):3464–3473, 1998.

[48] D. Simon and J. McQuarrie. Physical chemistry: a molecular approach. University Science Books: Sausalito, CA, 1997.

[49] M. Suk and N. Aluru. Molecular and continuum hydrodynamics in graphene nanopores. RSC Adv., 3(24):9365–9372, 2013.

[50] M. E. Suk and N. Aluru. Water transport through ultrathin graphene. J. Phys. Chem. Lett., 1(10):1590–1594, 2010.

[51] H. Takaba, Y. Onumata, and S.-i. Nakao. Molecular simulation of pressure-driven fluid flow in nanoporous membranes. J. Chem. Phys., 127(5):054703, 2007.

[52] X. Tan, Z. Zhou, and M. M.-C. Cheng. Electrowetting on dielectric experiments using graphene. Nanotechnology, 23(37):375501, 2012.

[53] K. P. Travis, B. Todd, and D. J. Evans. Departure from navier-stokes hydrodynamics in confined liquids. Phys. Rev. E, 55(4):4288, 1997.

[54] P. B. Warren. Dissipative particle dynamics. Curr. Opin. Colloid Interface Sci., 3(6):620–624, 1998.

[55] T. Werder, J. Walther, R. Jaffe, T. Halicioglu, and P. Koumoutsakos. On the water-carbon interaction for use in molecular dynamics simulations of graphite and carbon nanotubes. J. Phys. Chem. B, 107(6):1345–1352, 2003.

[56] A. R. Wheeler. Putting electrowetting to work. Science, 322(5901):539–540, 2008.

[57] A. P. Willard and D. Chandler. Instantaneous liquid interfaces. J. Phys. Chem. B, 114(5):1954–1958, 2010.

[58] A. P. Willard and D. Chandler. The molecular structure of the interface between water and a hydrophobic substrate is liquid-vapor like. J. Chem. Phys., 141(18):18C519, 2014.

[59] T. Young. An essay on the cohesion of fluids. Philos. Trans. R. Soc. London, 95:65–87, 1805.

[60] Q. Zaib and H. Fath. Application of carbon nano-materials in desalination processes. Desalin. Water Treat., 51(1-3):627–636, 2013.

[61] F. Zhu, E. Tajkhorshid, and K. Schulten. Collective diffusion model for water permeation through microscopic channels. Phys. Rev. Lett., 93(22):224501, 2004.

[62] F. Zhu, E. Tajkhorshid, and K. Schulten. Theory and simulation of water permeation in aquaporin-1. Biophys. J., 86(1):50–57, 2004.

Chapter 2

Tunable Surface Hydrophobicity

2.1 The Tunable Hydrophobic Effect on Electrically Doped Graphene

Using molecular dynamics simulations, we study the hydrophobic effect on electrically doped single layer graphene. With doping levels measured in volts, large changes in contact angle occur for modest voltages applied to the sheet. The effect can be understood as a renormalization of the surface tension between graphene and water in the presence of an electric field generated by the dopant charge, a collective effect termed electrowetting. Because the electronic density of states scales linearly with energy in the vicinity of the Fermi energy, the cosine of the contact angle scales quartically with the applied voltage rather than quadratically, as it would for a two-dimensional metal or in multiple layer graphene. While electrowetting explains the phenomenon, it does not account for the slight asymmetry observed in the hydrophobic response between n- and p-doping.

The contents of this chapter have been adapted from the paper titled "The Tunable Hydrophobic Effect on Electrically Doped Graphene", published in January 2014 in the *Journal of Physical Chemistry B*.[50] Additional simulation data not included in the original publication is provided in the appendix to this section.

2.1.1 Introduction

Graphene, an allotrope of carbon that is one atom thick, is a material with high mechanical strength[24] and many novel electronic properties that emerge from the dispersion relationship of

electrons near the Fermi energy[7;11;47]. These properties can be tuned by doping the material away from the Fermi level by adding charge carriers, electrons or holes, either chemically or electrostatically (Figure 2.1).[3;4;18;40;43] Recent experiments using chemical doping[21;41;51;67] have explored energies on the order of 1 eV above and below the Fermi energy, corresponding to excess carrier densities on the order of $10^{12} - 10^{13} cm^{-2}$.[67] Even larger densities, $\approx 10^{14} cm^{-2}$, have been reported for electrostatically doped graphene on insulating substrates[37].

While the lion's share of work to date has focused on the optical and transport properties of doped graphene, we show that electronic doping changes the material's hydrophobicity in a tunable manner. Because a pristine graphene sheet should be hydrophobic[23;53;57], these results may have impact on applications that use nanoporous graphene as a semipermeable membrane for liquids and gases.[10;35]

The fidelity of a semipermeable membrane is rooted in intermolecular interactions, both local and collective, between the membrane and the fluid. Recent work by Baker et al. have shown that hydrophobicity at the air-water interface is an interplay between local hydrogen bonding interactions and collective capillary wave motions[1]. In applications of single-walled carbon nanotubes to water desalination, the throughput and rejection ratio is a strong function of both the specific molecular interactions that exclude salt ions and the collective motion of "single-file" water in the tube.[36] Understanding how local and collective molecular motions control hydrophobicity and aqueous transport, particularly at charged interfaces and in confined environments, is a topic of timely and fundamental importance.

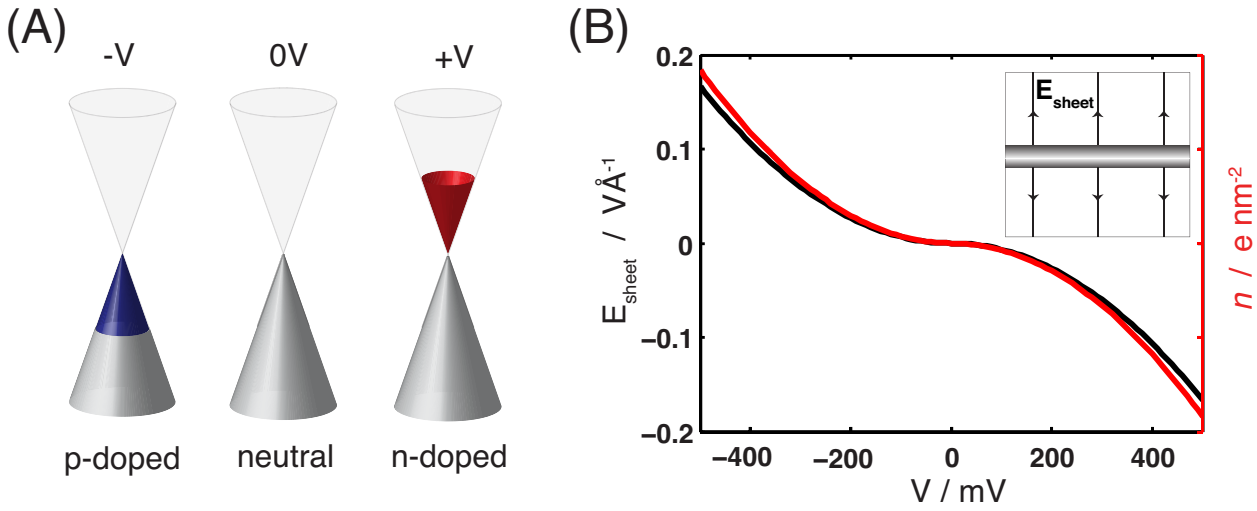

Figure 2.1: Neutral single layer graphene is a semimetal, where there is no energy gap between the filled valence bands and empty conduction bands at the high symmetry points K, K'. (A) The electronic dispersion relationship in the vicinity of the Fermi energy is a cone-shaped function of k_x, k_y wavevectors. Emptying and filling the electron population with a negative, zero, and positive applied voltage. (B) The electric field magnitude of an infinite uniformly charged sheet, E_{sheet}, is proportional to the excess charge density, n, as a function of applied voltage. The inset shows the graphene layer (gray rectangle), with the electric field lines normal to the sheet.

Doping in experiments can be modeled by fixing the electronic chemical potential of graphene relative to the Fermi energy. The excess chemical potential is eV, where e is the (positive) fundamental charge and V is the voltage. Positive voltages correspond to additional electrons (n-doping) and negative voltages correspond to additional holes (p-doping). A drop of liquid water placed on a doped graphene sheet experiences molecular and collective interactions. At the molecular level, the excess carriers on the graphene surface are exposed and can allow hydrogen bonds between the carbon atoms and the water molecules. But the excess charge generates an electric field that acts collectively and polarizes the water leading to a phenomenon called electrowetting. Both effects can profoundly change the wetting properties of the surface.[8;26;27]

The measure of a surface's hydrophobicity that we employ is the wetting contact angle between the droplet's edge and the solid surface, θ, first suggested by Young[66] and recently shown to

be a semiquantitative measure of hydrophobicity in nanoscale molecular dynamics simulations[27]. A contact angle greater than 90 degrees indicates that the surface is hydrophobic, while complete wetting corresponds to a contact angle of zero (Figure 2.2A). The Helmholtz free energy of a droplet on a surface is a function of the contact angle and three surface tensions.[55;59] In the absence of an applied electric field, Young's equation balances the various surface tensions at equilibrium, and yields for the contact angle, $cos\theta = \frac{\gamma_{SV}-\gamma_{SL}}{\gamma_{LV}}$, where $\gamma_{SV}, \gamma_{SL,}\gamma_{LV}$ are the surface-vapor, surface-liquid, and liquid-vapor surface tensions, respectively. In the presence of an applied electric field, the free energy acquires an additional term that describes the reversible work associated with applying a field to the liquid;[15;60] Young's equation becomes the Young-Lippmann equation, but the form of it depends on the details of the experiment or simulation. As we will show, the field-dependent term has the effect of renormalizing γ_{SL}, thus making the contact angle a strongly monotonically decreasing function of the voltage, V. The contact angle in our simulations varies markedly with respect to voltages that are routine in experiments.

If one can tune the contact angle by tens of degrees then electrowetting has applications in microfluidic biological sensors[56;62], adjustable optical lenses[6] and electronic paper.[30] One experimental method to control wetting is through electrowetting on a dielectric, EWOD, where a liquid drop rests on top of a dielectric layer.[44–46;57]. The droplet and the dielectric layer are connected in series between two electrodes held at a fixed voltage. For water droplets without a dielectric layer present, the presence of an electrode in the droplet limits the voltage to the electrolysis threshold of water at $\approx 1.24\ V$.[39] The dielectric blocks current and prevents electrolysis. In practice, EWOD experiments with water require very large voltages, on the order of tens or hundreds of volts to achieve appreciable contact angle changes.[38;57;58] In our study, the water droplet rests directly on single layer graphene. We find changes in the contact angle for water on graphene that are on the order of 15 degrees, but with voltages over a factor of three less than water's oxidation potential. The natural hydrophobicity of graphene provides a liquid-vapor interface that is both hydrophobic and insulating. It is not breached by the application of a field, and in many ways plays the role of the insulating dielectric layer in EWOD experiments.

2.1.2 Model and Theory

We compute the contact angle for water on a doped graphene sheet using molecular dynamics simulations with the LAMMPS package,[52] modified to properly compute forces in a non-neutral, nonperiodic simulation, as discussed below.[2] All simulations were performed with a fixed number of particles, volume, and energy (NVE) for average temperatures of 300 K. All reported results are simulations of 2000 water molecules, corresponding to a droplet roughly 6 nm in diameter. We did not observe any qualitative changes in the contact angles for simulations with between 2000 and 17,600 molecules. Thirty-two trajectories were collected and analyzed for each voltage studied. Each trajectory began with water molecules arranged in a box-like geometry that was equilibrated for 350 ps using NVE molecular dynamics prior to data collection for 1 ns. The simulations model doped graphene by placing a partial charge on the carbon atoms so that the sheet has the same mean charge density as it would at fixed chemical potential. This is equivalent to introducing a "quasi Fermi level," which is standard in semiconductor physics.[34] Scanning tunneling microscopy studies report that carrier density in graphene localizes at carbon atoms or along bonds between carbon atoms,[64] so this approximation should be reasonably faithful to the microscopic electronic configuration of doped graphene. Even when graphene is doped chemically, the excess charge carriers tend to delocalize throughout the sheet.[67] By fixing the partial charge on a carbon atom, we ignore fluctuations in the charge density that would be present in the grand canonical ensemble at fixed chemical potential. This approximation is justifiable because the electric field generated by the droplet at the graphene surface is many orders of magnitude smaller than the smallest electric fields used here.

We modeled the system using the SPC/E potential[5] for water and a Lennard-Jones (LJ) potential between the oxygen and carbon atoms, where the carbon-oxygen LJ parameters were chosen to match experimental data on measured contact angles.[61] Consistent with the high mechanical strength of graphene, the carbon atoms were held fixed. Hydrogen bonding in the SPC/E potential is a balance between the LJ oxygen-oxygen forces and the favorable electrostatic hydrogen-oxygen

interaction. Excess charges on the carbon atoms do, in principle, allow for the same kind of hydrogen bond formation between oxygen and carbon as the SPC/E potential would describe. As the magnitude of the carbon atom's partial charge increases, the carbon atoms can disrupt the hydrogen bond structure at the water surface. One could imagine that these effects might depend sensitively on the location of the carbon partial charges, but placing the excess charge above or below the sheet by $\approx$ 1Å, near where the π-electron density would peak in graphene, does not change our results quantitatively. This result foreshadows a relatively weak contribution to the hydrophobic effect from the molecular hydrogen bonding at the surface.

The appropriate boundary conditions for our simulation are periodic in the plane of the sheet, which we take as the x and y axes, but nonperiodic in the direction normal to the sheet, here taken to be the z-direction. The graphene sheet is centered at $z = 0$. This "slab" geometry is typical in studies of interfacial phenomenon[63] and can be challenging to simulate efficiently.[2] Simulations of charged systems in the slab geometry must be done with care.[2] For charged systems that are periodic in all three dimensions, it is conventional to use Ewald sums with a counter charge distributed uniformly in space, similar to the jellium model of the homogeneous electron gas. In this case the background charge modifies the energy, but not the forces.[2] In the Yeh-Berkowitz slab summation method[65] applied to a charged system, this is no longer true and the forces on charged particles must be corrected.[2] A vacuum layer sits between images in the nonperiodic direction and the Ewald sum includes a correction to forces on charged particles so that there are no interactions between replicas in this direction.[2] We employ the EW3DC methodology as modified for a non-neutral system, using a suitably designed geometry for the Ewald sum.[2;65] Additional simulation details appear in the Supporting Information.

2.1.3 Results and Discussion

The linear approximation for the low energy electronic dispersion relationship in graphene is excellent for the voltage ranges explored here.[13] The excess charge density on graphene at tem-

perature T and voltage V is

$$n(V,T) = -e \int_0^\infty d\epsilon \; f(\epsilon, V, T) g(\epsilon) \tag{2.1}$$

where f is the Fermi occupation factor, $f(\epsilon, V, T) = sign(V) \left(\exp\left[\{\epsilon - e|V|\}/k_B T\right] + 1\right)^{-1}$ that exploits particle-hole symmetry. The energy, ϵ, is relative to the Fermi energy, $V > 0$ for electrons (n-doping), $V < 0$ for holes (p-doping), and k_B is the Boltzmann constant. $g(\epsilon) = \frac{8\pi|\epsilon|}{(hv_F)^2}$ is the density of states per unit area including spin and valley degeneracies.[47] h is Planck's constant and $v_F = 10^6 m/s$ is the Fermi velocity in graphene.[47] The excess charge density per fundamental charge varies over a range of $\pm 2 \times 10^{13} cm^{-2}$ for V between -500 and 500 mV, which is well within the range accessible via chemical doping.[67] Equation (2.1) can be expressed exactly in terms of the polylog function. However, the zero-temperature approximation to $n(V,T)$ gives a very simple form and shows that $n(V,0) \propto V^2$. At $T = 300$ K, this approximation holds well for voltages exceeding about 200 mV.

At distances from the sheet large enough that the lattice structure of graphene cannot be resolved, continuum electrostatics predicts the electric field is directed along the surface normal with a constant field strength of $E_{sheet} = \frac{n}{2\epsilon_0}$, where ϵ_0 is the vacuum permittivity. Interestingly, the electric field in our simulations shows that for distances from the sheet in the z-direction larger than about 2 Å, the continuum electrostatic description is extremely accurate (Figure 2.2B). This is significant because there is not appreciable water density near graphene for z less than 3 Å.

Computational feasibility limits these simulations to thousands of water molecules and nanoseconds of simulation time. Electrovaporization of nanodroplets on this length scale restricts the electric field to values of $|E_{sheet}| \lesssim 0.1 \; V/\text{Å}$ [12;14]. Voltages in the domain of -354 to 354 mV correspond to a maximum $|E_{sheet}|$ of 0.085 $V/\text{Å}$ and fall below this threshold. At these field strengths, far below what water molecules exert on one another in bulk water,[19] a polarizable water model is not required[31].

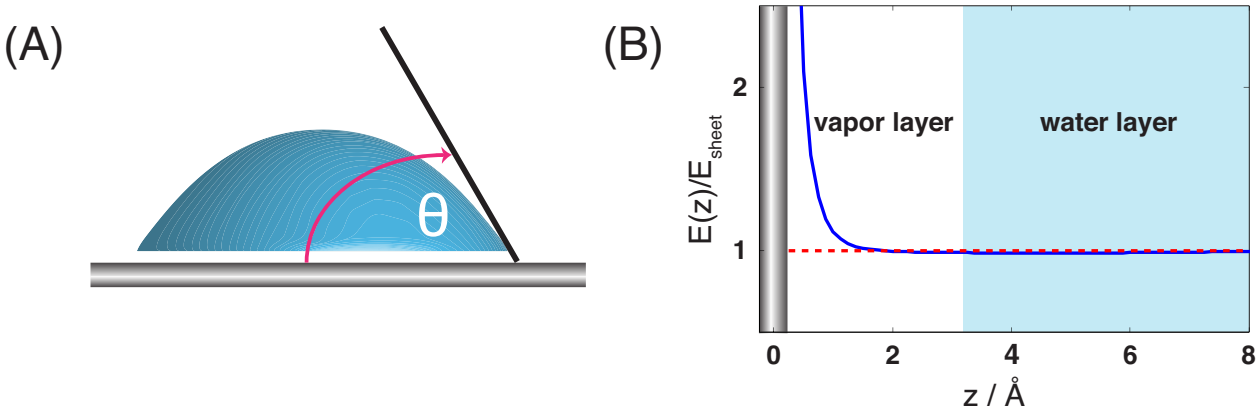

Figure 2.2: (A) The droplet edge, extrapolated to the graphene sheet (gray rectangle), gives the contact angle, θ. (B) The electric field above a charged graphene sheet from molecular dynamics simulations of a charged system in the slab geometry. The electric field rapidly converges to that of an infinite charged sheet, E_{sheet}, in the vapor layer that intervenes between the water and the graphene sheet.

The water density in cylindrical coordinates is $\rho(r,z) = \sum_l \frac{1}{2\pi r}\langle\delta(r-r_l)\delta(z-z_l)\rangle$, where δ is the Dirac delta function, r_l is the radius with respect to the droplet center of mass and z_l is the z coordinate of oxygen atom l. The brackets denote an average over all configurations sampled. The density was evaluated by histogramming the position data in 1 Å intervals for both r and z. We defined the droplet edge as the values for r and z at which $\rho(r,z) = \rho_B/2$ where ρ_B is the bulk density of water.[61] The droplet edges were determined by two-dimensional linear interpolation of the computed $\rho(r,z)$ and are shown in Figure 2.3.

Obtaining the contact angle from the droplet edge contours is a nonlinear fitting procedure that is prone to uncertainty because one needs to retrieve the inverse tangent function near $\pi/2$. Our method differs from others reported in the literature.[8;15;61] We used a procedure chosen for both its robustness and numerical stability that we gauged using the jackknife method on the contour data.[20] The chosen method involves both a linear regression and an extrapolation. Recognizing that the droplet shapes are elliptical, we fit the droplet to the linear function $R = aZ + b$ where $R(r) = r^2$ and $Z(z) = (z - z_0)^2$. a, b are fit parameters determined by linear regression for fixed z_0, and the

parameters of best fit, a, b, and z_0 simultaneously minimize χ^2.[54] The contact angle is related to the slope of the contour extrapolated to $z = 0$, which yields $\tan(\theta) = \left.\frac{dz}{dr}\right|_{z=0} = \frac{\sqrt{az_0^2+b}}{az_0}$. Fitting the edge contours using a polynomial fit[8] changes the value of the angles, but does not change their relative difference observed over the voltage range studied. Contour data near the surface with $z < 8$Å were excluded from the fit.[61]

Figure 2.3 displays the droplet contours for both n- and p-doped graphene as a function of the voltage. The contact angles change by about 15 degrees for voltages in the range -354 to 354 mV (Figure 2.4A). Accompanying the change in angle, the droplet elongates in the direction of the electric field, similar to the case of pure electrowetting on graphite, corresponding to an external electric field applied to a neutral simulation.[15] To compare the case of pure electrowetting to electrically doped graphene, we repeated the simulations using neutral graphene in the slab geometry with a constant electric field applied in the z-direction chosen to match E_{sheet} at the same voltage in Figure 2.3. The results are virtually identical (Supporting Information). This is highly suggestive that the hydrophobic effect on electrically doped graphene is dominated by pure electrowetting, an entirely collective effect.

To further examine this hypothesis, consider the Helmholtz free energy of a droplet, approximated as a uniform isotropic dielectric box with base area A_{SL} and height ℓ, on a surface with a uniform electric field applied to it. As the droplet polarizes in response to an applied electric field, E, the internal energy of the entire system, including the electric field, decreases by an amount proportional to E^2. The free energy is

$$F = F_0 + \Phi, \tag{2.2}$$

where F_0 is the free energy (ignoring the Laplace pressure and the line tension[61]) in absence of the field, $\Phi = -CE^2A_{SL}$ is the reversible work to polarize the droplet, and C is a constant that accounts for the capacitance of the droplet. After constraining the total volume and temperature to be constant, and using that $dA_{LV} \cong \cos(\theta)dA_{SL}$,[55] the differential Helmholtz free energy is

$$dF = \left[(\gamma_{SL} - CE^2) - \gamma_{SV} + \gamma_{LV}cos(\theta)\right] dA_{SL}. \tag{2.3}$$

The two terms in parentheses comprise the effective surface tension between the liquid and the surface. It is a strongly monotonically decreasing function of the field strength. As this surface tension gets smaller and smaller relative to γ_{SV}, the droplet will minimize its free energy by wetting the surface. Minimizing the free energy in Equation (2.3) yields the Young-Lippmann equation for the contact angle,

$$\cos(\theta) = \cos(\theta_0) + \frac{C}{\gamma_{LV}} E^2, \tag{2.4}$$

where θ_0 is the contact angle in absence of the field. This is the appropriate Young-Lippmann equation for pure electrowetting in our configuration and describes how the electric field renormalizes the surface-liquid surface tension.[45]

Local molecular interactions can also renormalize the surface tension. To judge their significance we make a scaling argument. The electric field depends linearly on the charge density, which in the zero temperature limit depends on the voltage squared, so that $E \propto V^2$ in graphene, or that $\cos(\theta) \propto V^4$. The scaling relationship with respect to voltage for other materials, such as bilayer graphene, is different because the density of states is different.[49] Bilayer graphene is a two dimensional gapless material with a quadratic energy dispersion relationship.[13]. The density of states is independent of the energy, as in the case of a two dimensional metal. In bilayer graphene, $\cos(\theta)$ would be proportional to V^2. For single layer graphene, the hydrophobicity is a strong function of the voltage because the density of states is linear in the vicinity of the Fermi energy.

Figure 2.4B displays $\cos(\theta)$ as a function of V^4. Over the range of voltages studied, the scaling argument given above matches the data well. The sign of the voltage determines the direction of the field but not its magnitude. Naively, one would expect to see identical results for droplet morphologies with voltages of equal magnitudes but opposite sign (Figure 2.3). The data show, however, a small asymmetry between n- and p-doping.

We attribute the asymmetry in the contact angle between positive and negative applied voltages to a difference in C for n- and p-doped graphene.[8] The slopes for the cosine of the angle scaling with V^4 for n- and p-doped graphene are statistically different to within a 95% confidence

interval. Because C depends on the static dielectric constant, which in turn depends strongly on the orientational susceptibility of the molecular dipoles, one can understand the results as a difference in the orientational stiffness of how the molecules respond to an applied field. The density in the z-direction, $\rho(z) = 2\pi \int dr\ r\rho(r, z)$, is not uniform for water against an interface, but instead displays peaks as a function of z, similar to the pair-density correlation function in the bulk liquid.[61] The differences in molecular arrangements between n- and p-doped graphene will be most pronounced at the graphene-water interface, or within the first effective water monolayer, which we define as all z values below the first minimum in $\rho(z)$, or $0 \leq z \leq 3$ Å, akin to how one classifies the first solvation shell in the bulk liquid.[29] Because the free energy of the droplet is invariant to rotation around the z-axis, the orientation of molecules about the z-axis should be irrelevant. We thus characterize the arrangements of water molecules in the first monolayer using two direction cosines of the water molecule relative to the z-axis that account for the C_{2V} symmetry of water. These quantities are the projection of the dipole moment and the hydrogen-hydrogen, HH, vector along z (Figure 2.5A).

In Figure 2.5B, and C we compare the molecular orientations in the first water monolayer between neutral and electrically doped graphene at the largest voltage magnitudes studied. The molecular orientations are similar between the neutral and p-doped cases. The n-doped case differs the most. The carbon atoms of n-doped graphene attract hydrogen atoms in the first monolayer, and the water dipole moment orients towards graphene (Figure 2.5B). The probability density for the dipole moment projection shifts and broadens more strongly in n-doped graphene compared to the neutral and p-doped cases, indicating that as the average orientation changes, fluctuations of the dipole moment in the z-direction are more facile. For neutral and p-doped graphene the most probable orientations are those with water in the plane of the graphene sheet (Figure 2.5C). But for n-doped graphene there is little preference for the molecule to lie in the plane, and here too, fluctuations occur easily about the molecular C_2 axis.

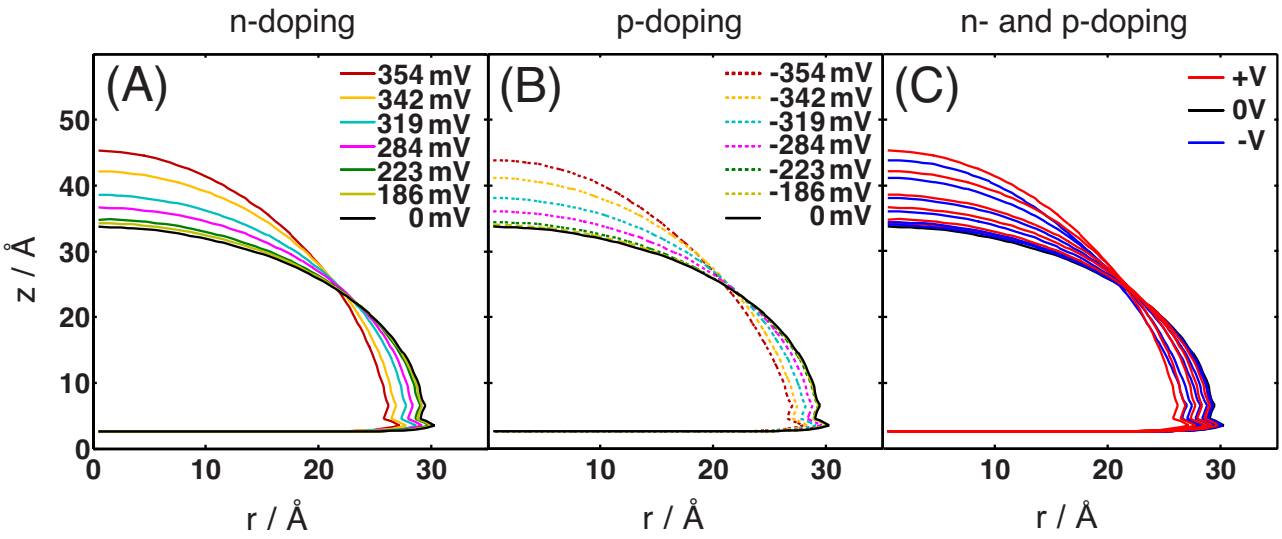

Figure 2.3: The droplet contour lines at half the bulk density of water depicting the liquid-vapor interface for various applied voltages from simulation. The r dimension is taken with respect to the droplet center of mass, and $z = 0$ is the location of the graphene plane. (A,B) Liquid-vapor interface for positive and negative applied voltages. (C) Red and blue colors correspond to voltages of equal magnitude voltages but opposite sign.

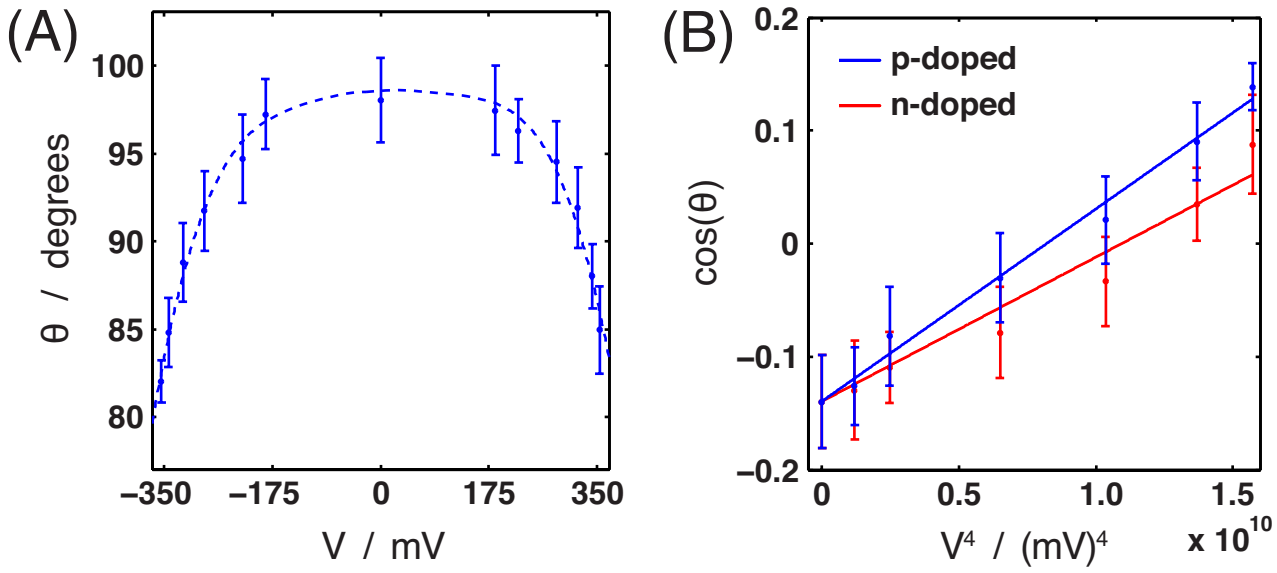

Figure 2.4: (A) Contact angle as a function of applied voltage. Neutral graphene has the highest contact angle, or most hydrophobic surface. Away from neutrality, the hydrophobicity decreases rapidly with voltage. The dashed line is a guide for the eye. (B) Cosine of the contact angle as a function of voltage. The modified Young-Lippmann equation predicts that $cos\,(\theta) \propto V^4$ if the electrowetting contributions dominate. The slopes for n- and p-doped graphene are statistically different to within 95% confidence using a statistical t-test. All error bars are one standard-deviation.

2.1.4 Conclusion

In this work, we presented simulations of the hydrophobic effect on electrically doped single layer graphene. Our results show that, for voltages applied to the sheet about 1/3 of a volt in magnitude, the contact angle changes by nearly 15 degrees for either n- or p-doping. Electrically doped single layer graphene becomes significantly less hydrophobic. A number of phenomena in liquid water, from the hydrophobic effect[9] to electron transfer[42] and vibrational dephasing,[19;48] come from a competition between local and collective effects. Understanding these relationships quantitatively can be very challenging. In the case studied here, we show that the hydrophobicity of electronically doped graphene can be understood as pure electrowetting, an entirely collective effect. We come to this conclusion by noting that the results for the contact angle are robust to

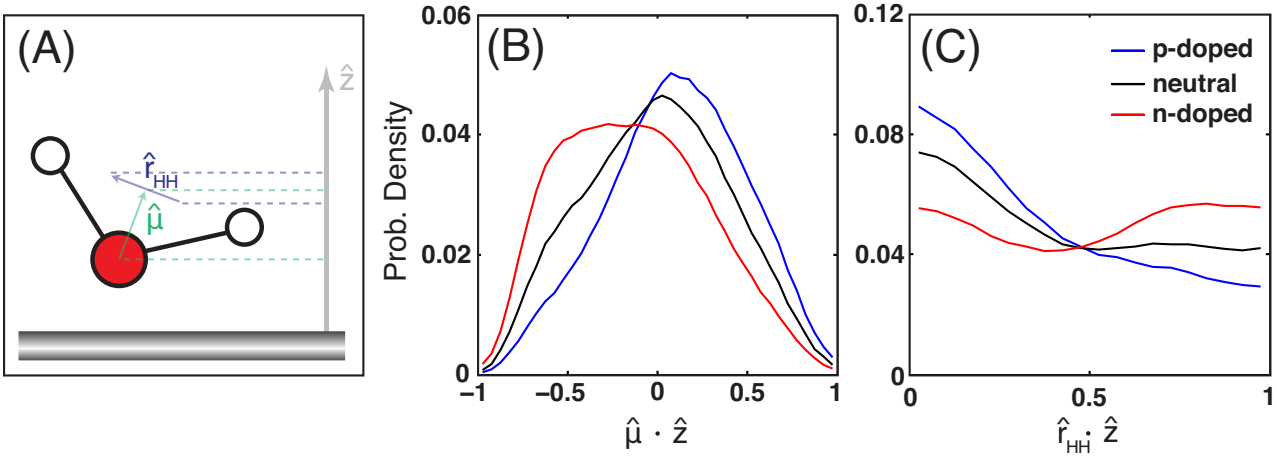

Figure 2.5: Molecular orientations in the first effective monolayer. (A) Z-projection of the dipole moment, μ, and hydrogen-hydrogen, HH vector. (B) Probability densities for the dipole moment and (C) hydrogen-hydrogen vector for waters in the first solvation shell for neutral (black), -354 mV (blue) and 354 mV (red) voltages. The standard error is smaller than the width of the lines.

variations in the placement of the charge on the carbon atoms, can be reproduced quantitatively by removing the charge and in its place applying a constant electric field at the equivalent strength of E_{sheet}, as done in Reference 15, and can be explained using a thermodynamic theory of electrowetting. While the phenomenon can be understood from a purely collective perspective, interfacial molecular orientational responses may differentiate the slopes in Figure 2.4.

Many of single layer graphene's novel properties emerge from the cone-shaped electronic dispersion relationship near the Fermi energy (Figure 2.1A). The same is true here. The graphene density of states implies that the cosine of the contact angle scales not like V^2, as it would in a two dimensional metal or in few-layer graphene, but instead like V^4. We expect that this scaling should be testable in experiments that compare doped bilayer and single layer graphene. The electric field we consider is generated by surface charge. Unlike the typical EWOD experiment, electrowetting on single layer graphene does not require an additional dielectric layer, nor does it require that an electrode be placed in the droplet. We expect that these features, in addition to the extreme sensitivity of the hydrophobic effect for voltages that are easily attainable in current experiments, will enable many applications.

2.2 Appendix

2.2.1 Low Temperature Charge Density of Infinite Graphene Sheet

Treat the graphene monolayer as an infinite, uniformly charged sheet. The electric field above an infinite sheet is[28]

$$E_{sheet}(V,T) = \frac{n(V,T)}{2\epsilon_0} \tag{2.5}$$

where n, the excess charge density, is a function of applied potential V and temperature T, and ϵ_0 is the permittivity of free space. The excess charge density can be calculated

$$n(V,T) = -e\int_0^\infty dE\, f(E,V,T)g(E) \tag{2.6}$$

where $g(E)$ is the density of electronic states as a function of energy. The Fermi distribution, f, can be written

$$f(E,V,T) = sign(V)\frac{1}{exp\left[\{E - e|V|\}/k_BT\right]+1} \tag{2.7}$$

where k_B is Boltzmann's constant, e is the fundamental (positive) charge, and we have exploited particle-hole symmetry. When $V > 0$, electrons are deposited onto the graphene and the monolayer is n-doped. Similarly, when $V < 0$, electrons leave the graphene layer leaving excess positive charge, and the monolayer is p-doped. In the low-temperature limit,

$$f(E,V,T \to 0) = sign(V)\Theta\left(e|V| - E\right) \tag{2.8}$$

where the Heaviside theta function, $\Theta(x) = 1$ for $x \geq 0$, and 0 otherwise. Inserting the density of electronic states, $g(E) = \frac{8\pi}{\left(hv_f\right)^2}E$,[47] Equation 2.6 becomes

$$\Rightarrow n(V,T \to 0) = -e\int_0^{e|V|} dE\ sign(V)\frac{8\pi}{\left(hv_f\right)^2}E \tag{2.9}$$

$$= -e\ sign(V)\frac{4}{\left(hv_f\right)^2}(eV)^2. \tag{2.10}$$

Finally, in the low temperature limit, for an infinite graphene sheet, the electric field is given by

$$E_{sheet}(V,T \to 0) = -sign(V)\frac{2e\left(eV\right)^2}{\epsilon_0\left(hv_f\right)^2} \tag{2.11}$$

$$\Rightarrow E_{sheet}(V,T \to 0) \propto V^2. \tag{2.12}$$

Importantly, we note that the electric field is proportional to the square of the applied potential.

2.2.2 Additional Simulation Details

Our simulations used the particle-particle/particle-mesh method to numerically calculate the Coulomb potential, with a real space cutoff $r_c = 20$ Å.[16;32] A reciprocal space mesh was chosen with $32 \times 32 \times 75$ points in the k_x, k_y and k_z directions, respectively, with a screening parameter

of 0.1253 $Å^{-1}$.[16] The angle and bond lengths of water were constrained using the SHAKE algorithm.[25] The particle equations of motion were numerically integrated using the Velocity-Verlet algorithm[17] with a timestep of 2 fs. Velocities were rescaled every 10 ps to maintain an average temperature of 300 K.

The x and y dimensions were treated periodically for all graphene-water simulations. The z dimension was treated nonperiodically using the slab summation procedure,[65] with a total length of 600 Å. The graphene layer spanned the entire simulation cell in the x and y directions which both had lateral dimensions of 200 Å. A preequilibrated cubic bulk volume of 2000 SPC/E waters[5] was used as the initial water configuration and was placed in the middle of the graphene sheet.[61] The carbon-oxygen Lennard-Jones parameters of Reference 61, case 28, were chosen. Molecular dynamics simulations agree with the experimental contact angle for water on neutral graphene when extrapolated to macroscopic droplets using these parameters.[61] The graphene-water system was equilibrated for 350 ps. Atomic positions were written every picosecond for a total of one nanosecond.

2.2.3 Boundary Conditions and Error in Simulations

In the slab geometry one dimension is treated nonperiodically, which we take as the z dimension. In the language of Yeh and Berkowitz, we employ the slab summation "EW3DC" method,[65] adopted for nonneutral simulations.[2] The length of the z dimension includes a sufficient amount of vacuum such that the interactions between slab images can be removed by correcting the forces on charged particles.[2;65] The force on the i^{th} charged particle was corrected by including

$$F_i = -\frac{4\pi}{\Omega}\left(M_z - Q_{tot} z_i\right) q_i \hat{e}_z \tag{2.13}$$

where Ω is the volume of the simulation box, M_z is the z component of the total dipole moment for the simulation, Q_{tot} is the total charge of the simulation, z_i is the z coordinate, and q_i is the charge of particle i.[2;65]

It is informative to compare the magnitude of the electric field, E, of a charged simulation to

the electric field of a homogeneously charged infinite sheet, E_{sheet}, at equivalent voltages (see main text). Figure 2.6 shows the percent difference, $\Delta E = \frac{\sqrt{E - E_{sheet}}}{E_{sheet}} \times 100\%$. The simulation parameters were chosen based on numerical accuracy and speed. We observe that ΔE is less than 2% for $z \gtrsim 2$ Å, the relevant region of the simulation occupied by water. ΔE is independent of the excess charge magnitude, or non-neutrality of the system. The results presented in Figure 2.6 have a negligible dependence on the x, y dimensions.

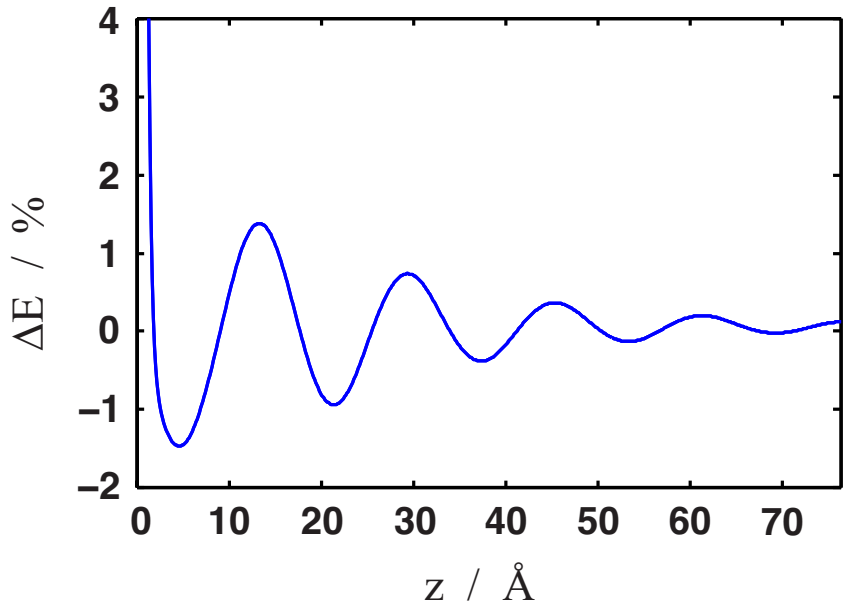

Figure 2.6: The percent difference, ΔE, between the electric field in a charged simulation and E_{sheet} (see main text). Note that the percent error in the force is independent of the magnitude of the applied voltage, and is determined by the simulation parameters used for numerical evaluation of the Coulomb potential.

2.2.4 Contact Angles for Charged and Constant Electric Field Simulations

To assess molecular contributions to electrowetting, we performed constant electric field simulations. Instead of doping the carbon atoms with excess charge, a constant electric field, E_{sheet}, was applied normal to the graphene surface. The liquid-vapor interfaces are nearly indistinguishable for the charged and constant electric field simulations. Therefore, the contact angles for the

charged and constant electric field simulations are identical (Figure 2.7).

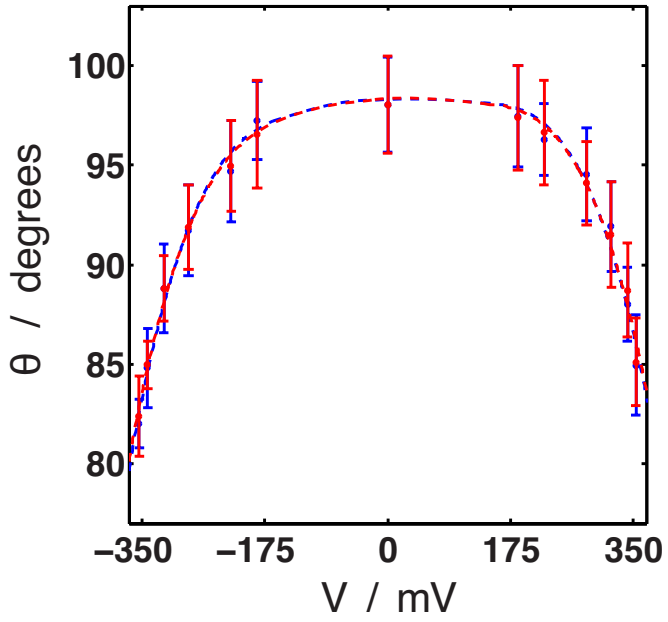

Figure 2.7: Contact angle as a function of applied voltage for the charged (blue) and constant electric field (red) simulations. The contact angles are identical for the charged and constant electric field simulations. These results imply that there is little contribution to electrowetting from molecular bonding with the discrete carbon lattice. The dashed lines are a guide for the eye.

2.2.5 Additional Physical Quantities

Oxygen, Hydrogen Density

The oxygen and hydrogen density calculated within a cylindrical subvolume of the droplet is shown in Figure 2.8. The excess doping type is indicated to aid in thinking about the density layering near the graphene. Both densities show very small changes for the voltage range studied. The hydrogen density nearest the graphene layer is as physically expected. For n-doped graphene, the hydrogen density is enhanced near the graphene layer, and similarly for p-doped graphene the hydrogens move away from the graphene layer as compared to the neutral sheet case.

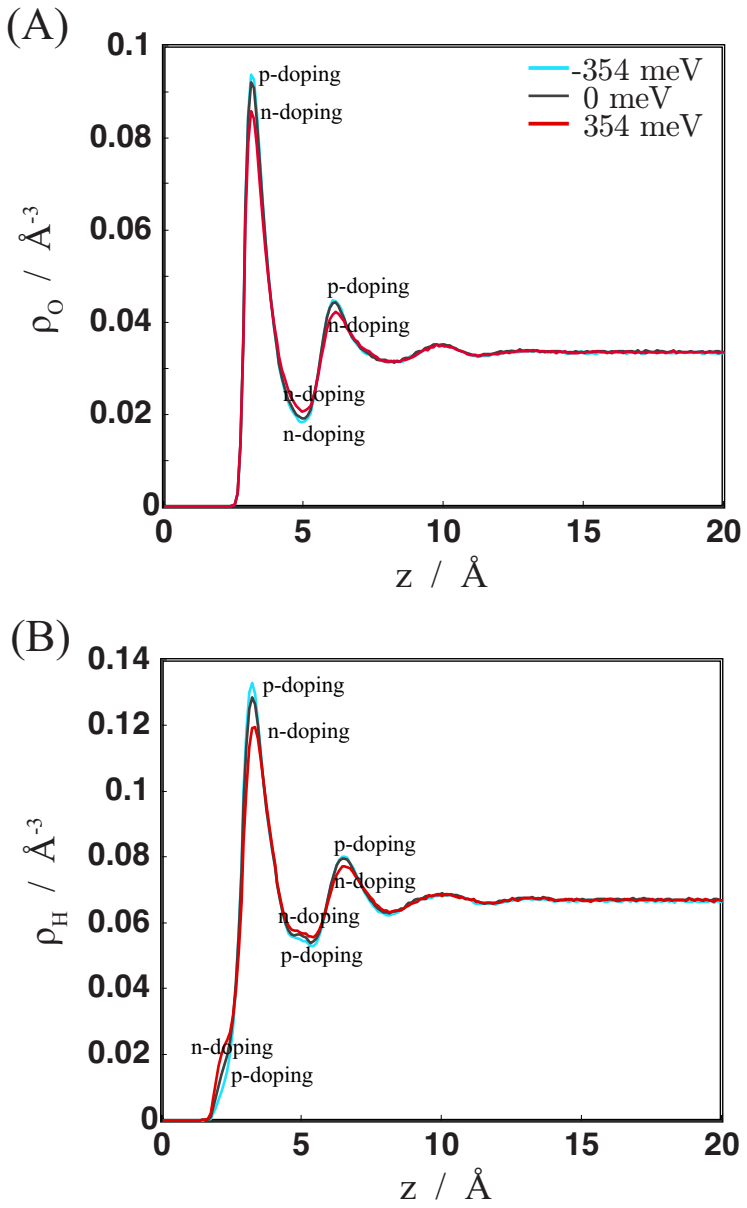

Figure 2.8: (A) Oxygen and (B) hydrogen density for select voltages as a function of distance above the graphene surface, z. Despite varying the voltage from nearly $\pm 1/3$ of a volt, there are very small changes in the densities throughout our simulations. The excess doping type is indicated to aid in thinking about the density layering near the graphene. The oxygen density is depleted nearest the graphene layer for n-doped graphene, as expected from physical intuition. Similarly the hydrogen density is enhanced nearest the graphene sheet for n-doped graphene. The peaks and valleys of the density are labeled for illustrative purposes. This data was taken for a droplet subvolume defined by water molecules with oxygen coordinates $r \leq 20$Å.

Hydrogen Bonding

Similar to the oxygen and hydrogen densities, the number of hydrogen bonds changes very little in the range of applied voltages studied. The hydrogen bonds were found using the geometric criterion, that sets stipulations on the distances.[22] The geometric criterion defines hydrogen bond as having distances $R(O\ldots O) \leq 3.5$Å, $R(O\ldots H) \leq 2.6$Å and the angle $H - O\ldots O \leq 30^o$. The average number of hydrogen bonds approaches ≈ 3.5 as expected for SPC/E water several angstroms away from the graphene surface.

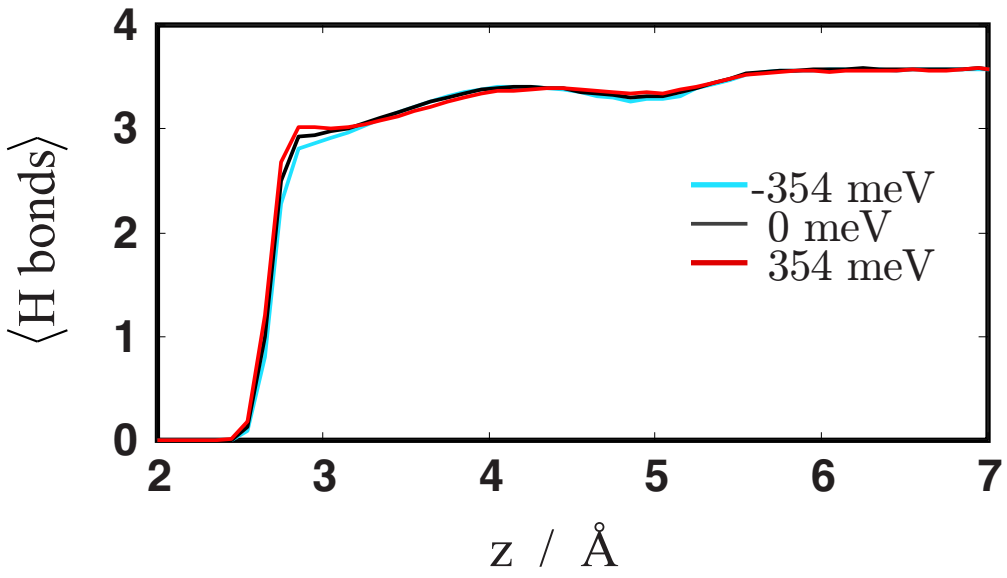

Figure 2.9: Hydrogen bonds as a function of z using the geometric criteria for three voltages. The graphene surface is located at $z = 0$. The number of hydrogen bonds is slightly depleted for p-doped graphene. As shown in Figure 2.8, the oxygen density is slightly enhanced near p-doped graphene, therefore leaving less oxygen atoms available for hydrogen bonding. Similarly, the average number of hydrogen bonds is slightly enhanced for n-doped graphene. This data was taken for a droplet subvolume defined by water molecules with oxygen coordinates $r \leq 20$Å.

Water Orientation: Conditional Probability of OH Bonds

In order to determine the water orientation relative the graphene surface, the conditional probability for orientation of both the OH bonds in water was calculated using

$$P(u,u'|z) = \frac{1}{\rho(z)} \sum_{i=1}^{N} \langle \delta\left(u - cos\theta_i^{(1)}\right) \delta\left(u' - cos\theta_i^{(2)}\right) \rangle \tag{2.14}$$

where $\rho(z)$ is the water density, $\theta_i^{(1)}$ is the angle of one of the OH bonds, and $\theta_i^{(2)}$ is the second OH bond of the ith water molecule.[63] u, $u' = 1{,}0$, or -1 and represent OH bonds pointing perpendicular towards, parallel, and perpendicular away from the graphene layer respectively.

Figure 2.10 shows the conditional probability for OH bond orientations nearest the graphene layer ($z = 2.8$Å) and near the first hydration shell ($z = 3.2$Å). The conditional probability for p-doped graphene is qualitatively similar to the neutral case, where most of the probability lies in the center where $u = u' \cong 0$, corresponding to a water molecule lying in a plane parallel with the graphene surface. The other areas of high probability correspond to the case where one of the OH bonds is perpendicular oriented away from the graphene layer ($u, u' \cong 1$) and consequently the other OH bond is pointed slightly downwards toward the graphene layer.

Water molecules near neutral graphene are most likely to lie perpendicular to the graphene layer with both OH bonds parallel the graphene surface, with the next most probable orientation having one OH bond pointing towards the graphene layer. For the negative (positive) applied potential, there is little (high) probabilty for observing an OH bond pointing towards the graphene layer, as one would expect from intuition. As the graphene is n-doped, the hydrogen atoms reorient so as to be nearer the graphene layer.

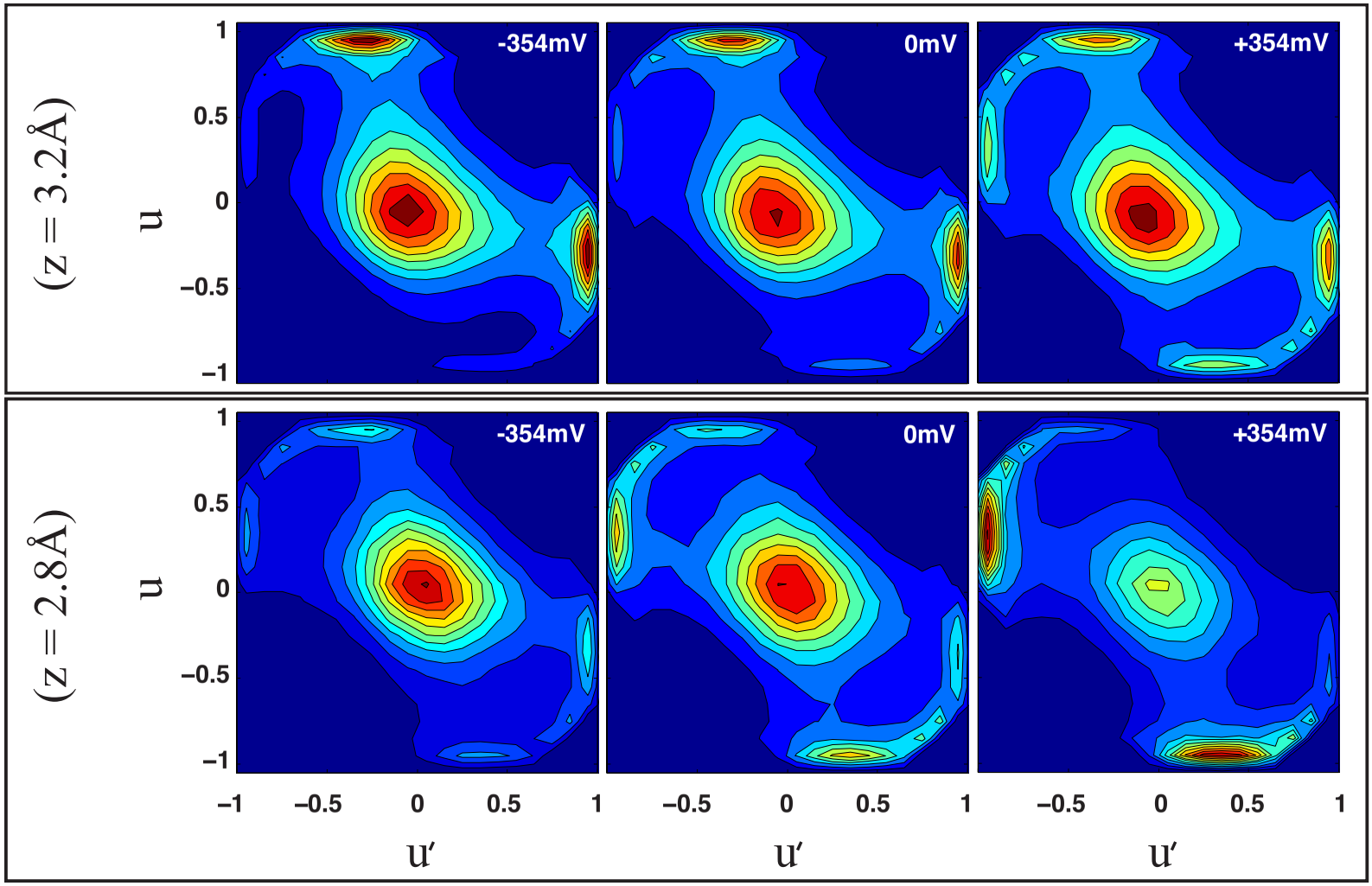

Figure 2.10: OH bond orientation conditional probability for the neutral and select applied potentials. (Top Panel) Conditional probability close to the first peak of the first hydration shell, z = 3.2Å. (Bot Panel) z slice nearest the graphene monolayer, z = 2.8Å.

2.2.6 Young's Equation

Young's equation describes the wetting contact angle, θ, for a droplet in contact with a surface, and was originally formulated by Thomas Young in 1805.[66] The tensions acting on a droplet near the surface are illustrated in Figure 2.11. What follows is the so-called "local-derivation" of the contact angle.[55]

Young's equation is an equilibrium statement pertaining to the balance of the three surface tensions, γ_{SL}, γ_{LV}, γ_{SV} corresponding to the solid-liquid, liquid-vapor, and solid-vapor surface tensions respectively. The surface tensions have units of energy per unit area, and correspond to the energy required to deform the droplet surface area.

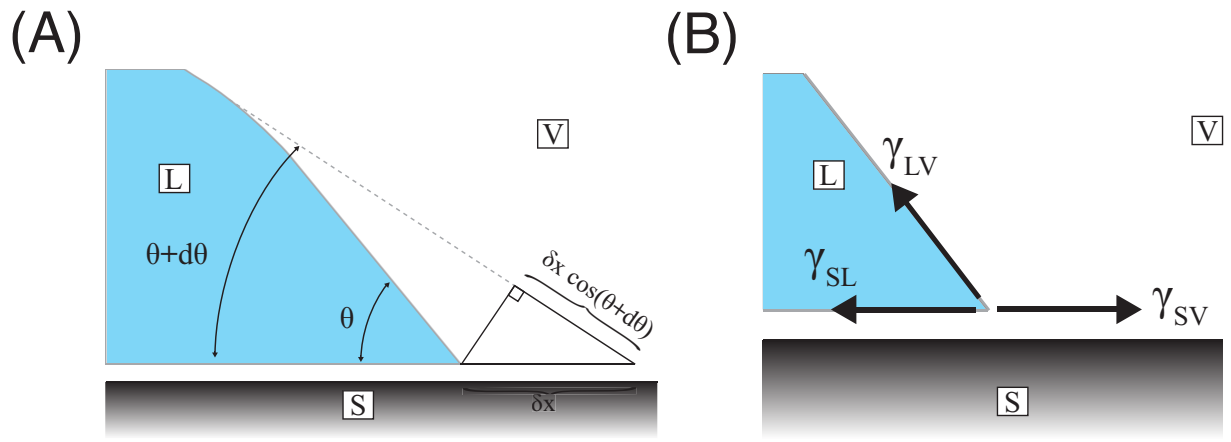

Figure 2.11: (A) Differential area and length changes used in the "local-derivation" of Young's equation for wetting. (B) Surface tensions on a droplet at the three-phase contact line. $\gamma_{SL}, \gamma_{LV}, \gamma_{SV}$ correspond to the solid-liquid, liquid-vapor, and solid-vapor surface tensions respectively. The surface tension has units of energy per unit area, and describes the amount of energy required to deform the surface area.

Consider that the contact angle, θ, undergoes a differential change to $\theta + d\theta$ (Figure 2.11). If the droplet has a large enough curvature, we may write the ratio of the infinitesimal area change as

$$\frac{\delta A_{LV}}{\delta A_{SL}} = cos\,(\theta + \delta\theta) \sim cos\theta \tag{2.15}$$

$$\Rightarrow \delta A_{LV} = \delta A_{SL} cos\theta. \tag{2.16}$$

At constant volume and temperature, the differential of the Helmholtz free energy is

$$\Rightarrow dF_0 = \gamma_{SL} dA_{SL} - \gamma_{SV} dA_{SL} + \gamma_{LV} dA_{LV} \tag{2.17}$$

$$= \gamma_{SL} dA_{SL} - \gamma_{SV} dA_{SL} + cos\theta \gamma_{LV} dA_{SL} \tag{2.18}$$

$$= (\gamma_{SL} - \gamma_{SV} + cos\theta \gamma_{LV})\, dA_{SL}. \tag{2.19}$$

At equilibrium

$$\Rightarrow dF = 0 = (\gamma_{SL} - \gamma_{SV} + cos\theta \gamma_{LV}) \tag{2.20}$$

$$\Rightarrow cos\theta = \frac{\gamma_{SV} - \gamma_{SL}}{\gamma_{LV}} \qquad \text{“Young's Equation”.} \tag{2.21}$$

Next we will modify Young's equation in the presence of an electric field.

2.2.7 Young's Equation In an Electric Field

Young's equation, Equation 2.21, must be modified if an electric field is applied. Assume for simplicity that the droplet can be approximated by a rectangular volume (Figure 2.12).

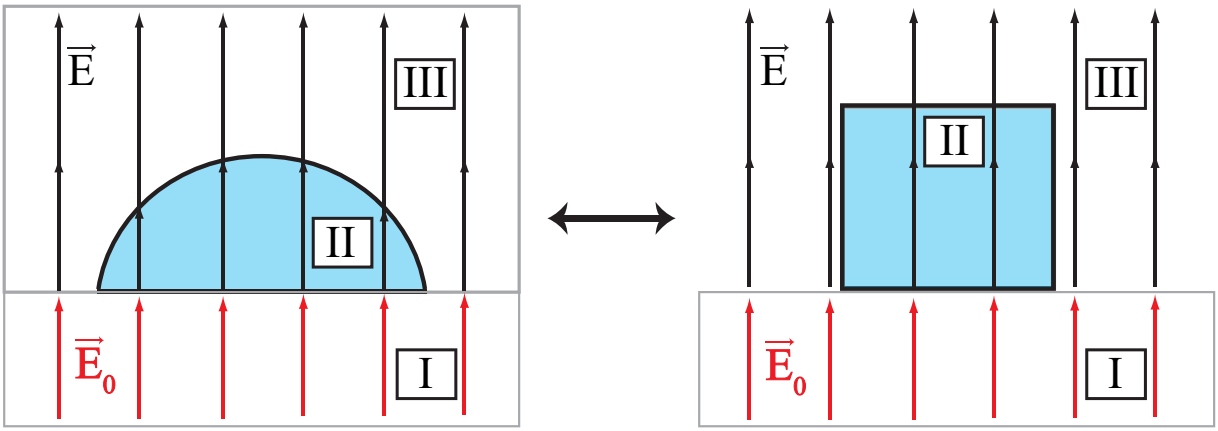

Figure 2.12: Volume of water in an externally applied electric field, $\mathbf{E}_0$. The screened electric field strength is **E**. The droplet (Left) for simplification can be considered as a rectangular volume (Right), thereby ignoring any effects due to the droplet morphology. In this picture, how the external field is created is immaterial to the problem, that is, it does not matter if the electric field is created inside a parallel plate capacitor or some other configuration. Region I corresponds to vacuum, with other regions defined accordingly.

A boundary condition on the displacement field perpendicular the interface between regions I and II is written as (Reference 28, Equation 4.26)

$$D_{\perp,II} - D_{\perp,I} = \rho_f \tag{2.22}$$

where ρ_f is the free charge at the interface. Since there is no free charge in the case of pure water (no ions), $\rho_f = 0$,

$$D_{\perp,II} = D_{\perp,I} \tag{2.23}$$

$$\epsilon E_{\perp,II} = \epsilon_0 E_0 \tag{2.24}$$

$$E_{\perp,II} = \frac{\epsilon_0}{\epsilon} E_0 = \frac{1}{\epsilon_r} E_0 \tag{2.25}$$

where $\epsilon_r = \frac{\epsilon}{\epsilon_0}$ is the dielectric constant, ϵ is the permittivity of water, and the last line assumed that water acts as a linear dielectric, $\mathbf{D} = \epsilon \mathbf{E}$. The Helmholtz free energy for the droplets is

$$F = F_0 + U_{electrostatic} \tag{2.26}$$

where $U_{electrostatic}$ is given by Equation (2.40), and F_0 is the non-electrostatic contributions to the Helmholtz free energy,

$$F_0 = U - TS \tag{2.27}$$

$$\Rightarrow dF_0 = \sum_{l=SL,LV,SV} \gamma_l dA_l. \tag{2.28}$$

Write the energy for composing the dielectric material in an external field (Reference 33, Equation 4.83)

$$U_{electrostatic} = \int_{all\ space} d\mathbf{x}\ \Phi(\mathbf{x}) \rho(\mathbf{x}) \tag{2.29}$$

where Φ is the spatial-dependent potential, and ρ is the charge density. We choose an ensemble where the charges fluctuate while the potential stays fixed. Because we only have bound charge, write the variation of the energy

$$\delta U_{electrostatic} = \int_{all\ space} d\mathbf{x}\ \Phi(\mathbf{x}) \delta\rho_B(\mathbf{x}) = \int_{all\ space} d\mathbf{x}\ \Phi(\mathbf{x}) \left(-\nabla \cdot \delta\mathbf{P}\right) \tag{2.30}$$

where **P** is the polarization of the dielectric. Make use of

$$\nabla \cdot (\Phi \delta \mathbf{P}) = \Phi \nabla \cdot (\delta \mathbf{P}) + \delta \mathbf{P} \cdot (\nabla \Phi) \tag{2.31}$$

$$\Rightarrow \Phi \nabla \cdot \delta P = \nabla \cdot \Phi \delta P - \delta P \cdot \nabla \Phi = \mathbf{E} \cdot \delta \mathbf{P} + \nabla \cdot (\Phi \delta \mathbf{P}) \,. \tag{2.32}$$

Now

$$\delta U_{electrostatic} = - \int_{all\ space} d\mathbf{x}\ (\mathbf{E} \cdot \delta \mathbf{P}) - \int_{all\ space} d\mathbf{x}\ (\nabla \cdot (\Phi \delta \mathbf{P})) \,. \tag{2.33}$$

The last term vanishes, as the integral is over all space. Using the divergence theorem

$$\int_{all\ space} d\mathbf{x}\ (\nabla \cdot (\Phi \delta \mathbf{P})) = \int dA\ \mathbf{n} \cdot (\Phi \delta \mathbf{P}) = 0. \tag{2.34}$$

In linear response $\mathbf{P} = \alpha \mathbf{E}$, where α is the (isotropic) polarizability. The integral over all space reduces to the region of space occupied by the droplet,

$$\delta U_{electrostatic} = - \int_{drop} d\mathbf{x}\ \mathbf{E} \cdot \delta \mathbf{P} \tag{2.35}$$

$$= - \alpha \int_{drop} d\mathbf{x}\ \mathbf{E} \cdot \delta \mathbf{E} \tag{2.36}$$

$$= - \frac{\alpha}{2} \delta \int_{drop} E^2. \tag{2.37}$$

$$\implies U_{electrostatic} = - \frac{\alpha}{2} E^2 V_{drop} \tag{2.38}$$

$$= - \frac{\alpha}{2} E^2 A_{SL} H \tag{2.39}$$

where A_{SL} and H is the area of a solid-liquid surface with height H. Now substitute (cf. Equation 2.25) $E = \frac{\epsilon_0}{\epsilon} E_0 = \frac{1}{\epsilon_r} E_0$, where E_0 is the external field produced by the graphene layer, which we approximate as a parallel plate capacitor, and the work of polarizing the dielectric media reads

$$U_{electrostatic} = - \frac{\alpha}{2 \epsilon_r^2} E_0^2 A_{SL} H. \tag{2.40}$$

Now the Helmholtz free energy is,

$$F = \gamma_{SL} A_{SL} + \gamma_{LV} A_{LV} + \gamma_{SV} A_{SV} - \frac{\alpha}{2} E^2 A_{SL} H. \tag{2.41}$$

The preceding equation is analogous to Young's equation in the absence of a field, except for the last term which accounts for the polarization of the water due to the applied electric field. This last term renormalizes the surface tension between water and grapheme and is responsible for the tunable hydrophobic effect. Following similarly to the derivation of Young's Equation 2.21, at equilibrium

$$dF = \gamma_{SL} dA_{SL} + \gamma_{LV} dA_{LV} + \gamma_{SV} dA_{SV} - \frac{\alpha}{2} E^2 dA_{SL} H \tag{2.42}$$

$$= \left[\gamma_{SL} + cos\theta \gamma_{LV} - \gamma_{SV} - \frac{\alpha H}{2} E^2 \right] dA_{SL} = 0 \tag{2.43}$$

$$\Rightarrow cos\theta = \frac{\gamma_{SL} - \gamma_{SV}}{\gamma_{LV}} - \frac{\alpha H}{2\gamma_{LV}} E^2 = cos\theta_0 + \mathscr{C} E^2 \tag{2.44}$$

where $cos\theta_0$ is Young's equation in the absence of an electric field (Equation 2.21), and $\mathscr{C} = \frac{-\alpha H}{2\gamma_{LV}}$ has units of capacitance. Since the electric field is proportional to the square of the potential (cf. §2.2.1),

$$cos\theta = cos\theta_0 + \mathscr{C}' V^4 \tag{2.45}$$

where $\mathscr{C}' = -sign(V) \frac{2e(eV)^2}{\epsilon_0 (h v_f)^2} \mathscr{C} = sign(V) \frac{e\alpha H (eV)^2}{\epsilon_0 \gamma_{LV} (h v_f)^2}$, having used Equation (2.11). For graphene, according to Equation 2.45, the cosine of the contact angle will scale as the fourth power of the applied potential.

Bibliography

[1] J. L. Baker, A. Widmer-Cooper, M. F. Toney, P. L. Geissler, and A. P. Alivisatos. Device-scale perpendicular alignment of colloidal nanorods. Nano Lett., 10(1):195–201, 2009.

[2] V. Ballenegger, A. Arnold, and J. Cerda. Simulations of non-neutral slab systems with long-range electrostatic interactions in two-dimensional periodic boundary conditions. J. Chem. Phys., 131:094107, 2009.

[3] W. Bao, G. Liu, Z. Zhao, H. Zhang, D. Yan, A. Deshpande, B. LeRoy, and C. N. Lau. Lithography-free fabrication of high quality substrate-supported and freestanding graphene devices. Nano Res., 3(2):98–102, 2010.

[4] W. Bao, K. Myhro, Z. Zhao, Z. Chen, W. Jang, L. Jing, F. Miao, H. Zhang, C. Dames, and C. N. Lau. In situ observation of electrostatic and thermal manipulation of suspended graphene membranes. Nano Lett., 12(11):5470–5474, 2012.

[5] H. Berendsen, J. Grigera, and T. Straatsma. The missing term in effective pair potentials. J. Phys. Chem., 91(24):6269–6271, 1987.

[6] B. Berge and J. Peseux. Variable focal lens controlled by an external voltage: An application of electrowetting. Eur. Phys. J. E, 3(2):159–163, 2000.

[7] A. W. Bott. Electrochemistry of semiconductors. Curr. Sep., 17:87–92, 1998.

[8] D. Bratko, C. D. Daub, K. Leung, and A. Luzar. Effect of field direction on electrowetting in a nanopore. J. Am. Chem. Soc., 129(9):2504–2510, 2007.

[9] D. Chandler. Hydrophobicity: Two faces of water. Nature, 417(6888):491–491, 2002.

[10] D. Cohen-Tanugi and J. Grossman. Water desalination across nanoporous graphene. Nano Lett., 12(7):3602–3608, 2012.

[11] M. Craciun, S. Russo, M. Yamamoto, and S. Tarucha. Tuneable electronic properties in graphene. Nano Today, 6(1):42–60, 2011.

[12] T. Cramer, F. Zerbetto, and R. García. Molecular mechanism of water bridge buildup: Field-induced formation of nanoscale menisci. Langmuir, 24(12):6116–6120, 2008.

[13] S. Das Sarma, S. Adam, E. H. Hwang, and E. Rossi. Electronic transport in two-dimensional graphene. Rev. Mod. Phys., 83:407–470, May 2011.

[14] C. Daub, D. Bratko, and A. Luzar. Electric control of wetting by salty nanodrops: Molecular dynamics simulations. J. Phys. Chem. C, 115(45):22393–22399, 2011.

[15] C. D. Daub, D. Bratko, K. Leung, and A. Luzar. Electrowetting at the nanoscale. J. Phys. Chem. C, 111(2):505–509, 2007.

[16] M. Deserno and C. Holm. How to mesh up ewald sums. ii. an accurate error estimate for the particle–particle–particle-mesh algorithm. J. Chem. Phys., 109:7694–7701, 1998.

[17] A. M. . T. D.J. Computer simulation of liquids. Oxford University Press: New York, 1989.

[18] X. Du, I. Skachko, A. Barker, and E. Y. Andrei. Approaching ballistic transport in suspended graphene. Nat. Nanotechnol., 3(8):491–495, 2008.

[19] J. D. Eaves, A. Tokmakoff, and P. L. Geissler. Electric field fluctuations drive vibrational dephasing in water. J. Phys. Chem. A, 109(42):9424–9436, 2005.

[20] B. Efron. The jackknife, the bootstrap and other resampling plans. Society for Industrial and Applied Mathematics: Philadelphia, 1982.

[21] D. B. Farmer, R. Golizadeh-Mojarad, V. Perebeinos, Y.-M. Lin, G. S. Tulevski, J. C. Tsang, and P. Avouris. Chemical doping and electron-hole conduction asymmetry in graphene devices. Nano Lett., 9(1):388–392, 2008.

[22] M. Ferrario, M. Haughney, I. R. McDonald, and M. L. Klein. Molecular-dynamics simulation of aqueous mixtures: Methanol, acetone, and ammonia. J. Chem. Phys., 93:5156, 1990.

[23] F. Fowkes and W. Harkins. The state of monolayers adsorbed at the interface solid-aqueous solution. J. Am. Chem. Soc., 62(12):3377–3386, 1940.

[24] I. Frank, D. M. Tanenbaum, A. Van der Zande, and P. L. McEuen. Mechanical properties of suspended graphene sheets. J. Vac. Sci. Technol. B, 25(6):2558–2561, 2007.

[25] D. Frenkel and B. Smit. Understanding molecular simulation: from algorithms to applications. Acadmic Press: San Diego, CA, 2001.

[26] N. Giovambattista, P. G. Debenedetti, and P. J. Rossky. Effect of surface polarity on water contact angle and interfacial hydration structure. J. Phys. Chem. B, 111(32):9581–9587, 2007.

[27] R. Godawat, S. N. Jamadagni, and S. Garde. Characterizing hydrophobicity of interfaces by using cavity formation, solute binding, and water correlations. Proc. Natl. Acad. Sci. USA, 106(36):15119–15124, 2009.

[28] D. J. Griffiths. Introduction to electrodynamics, 3rd edition. Pearson, 2005.

[29] J.-P. Hansen and I. R. McDonald. Theory of simple liquids, 3rd edition. Academic Press: Amsterdam, 1990.

[30] R. A. Hayes and B. Feenstra. Video-speed electronic paper based on electrowetting. Nature, 425(6956):383–385, 2003.

[31] T. Ho and A. Striolo. Polarizability effects in molecular dynamics simulations of the graphene-water interface. J. Chem. Phys., 138:054117, 2013.

[32] R. W. Hockney and J. W. Eastwood. Computer simulation using particles. McGraw-Hill: New York, 1981.

[33] J. D. Jackson. Classical electrodynamics, 3 edition. Wiley, 1999.

[34] C. Kittel. Introduction to solid state physics, 7th edition. Wiley: New York, 1996.

[35] S. P. Koenig, L. Wang, J. Pellegrino, and J. S. Bunch. Selective molecular sieving through porous graphene. Nat. Nanotechnol., 7(11):728–732, 2012.

[36] J. Köfinger, G. Hummer, and C. Dellago. Single-file water in nanopores. Phys. Chem. Chem. Phys., 13(34):15403–15417, 2011.

[37] C. N. Lau, W. Bao, and J. Velasco. Properties of suspended graphene membranes. Mater. Today, 15(6):238–245, 2012.

[38] C.-P. Lee, B.-Y. Fang, and Z.-H. Wei. Influence of electrolytes on contact angles of droplets under electric field. Analyst, 138(8):2372–2377, 2013.

[39] H. Li, T. Lu, L. Pan, Y. Zhang, and Z. Sun. Electrosorption behavior of graphene in nacl solutions. J. Mater. Chem., 19(37):6773–6779, 2009.

[40] Y.-M. Lin, H.-Y. Chiu, K. A. Jenkins, D. B. Farmer, P. Avouris, and A. Valdes-Garcia. Dual-gate graphene fets with f_T of 50 ghz. IEEE Electron Device Lett., 31(1):68–70, 2010.

[41] H. Liu, Y. Liu, and D. Zhu. Chemical doping of graphene. J. Mater. Chem., 21(10):3335–3345, 2011.

[42] R. A. Marcus. Electron transfer reactions in chemistry. theory and experiment. Rev. Mod. Phys., 65(3):599–610, 1993.

[43] I. Meric, M. Y. Han, A. F. Young, B. Ozyilmaz, P. Kim, and K. L. Shepard. Current saturation in zero-bandgap, top-gated graphene field-effect transistors. Nat. Nanotechnol., 3(11):654–659, Nov 2008.

[44] H. Moon, S. Cho, R. Garrell, and C.-J. Kim. Low voltage electrowetting-on-dielectric. J. Appl. Phys., 92(7):4080–4087, 2002.

[45] F. Mugele and J.-C. Baret. Electrowetting: from basics to applications. J. Phys. Condens. Matter, 17(28):R705–R774, 2005.

[46] W. Nelson and C.-J. Kim. Droplet actuation by electrowetting-on-dielectric (ewod): A review. J. Adhes. Sci. Technol., 26(12-17):1747–1771, 2012.

[47] A. Neto, F. Guinea, N. Peres, K. Novoselov, and A. Geim. The electronic properties of graphene. Rev. Mod. Phys., 81(1):109–162, 2009.

[48] R. A. Nicodemus, S. Corcelli, J. Skinner, and A. Tokmakoff. Collective hydrogen bond reorganization in water studied with temperature-dependent ultrafast infrared spectroscopy. J. Phys. Chem. B, 115(18):5604–5616, 2011.

[49] K. S. Novoselov, A. K. Geim, S. Morozov, D. Jiang, Y. Zhang, S. Dubonos, I. Grigorieva, and A. Firsov. Electric field effect in atomically thin carbon films. Science, 306(5696):666–669, 2004.

[50] J. H. Ostrowski and J. D. Eaves. The tunable hydrophobic effect on electrically doped graphene. J. Phys. Chem. B, 118(2):530–536, 2014.

[51] L. Panchakarla, K. Subrahmanyam, S. Saha, A. Govindaraj, H. Krishnamurthy, U. Waghmare, and C. Rao. Synthesis, structure, and properties of boron-and nitrogen-doped graphene. Adv. Mater., 21(46):4726–4730, 2009.

[52] S. Plimpton. Fast parallel algorithms for short-range molecular dynamics. J. Comput. Phys., 117(1):1–19, 1995.

[53] J. Rafiee, X. Mi, H. Gullapalli, A. V. Thomas, F. Yavari, Y. Shi, P. M. Ajayan, and N. A. Koratkar. Wetting transparency of graphene. Nat. Mater., 11(3):217–222, 2012.

[54] K. K. F. Riley. Mathematical methods for physics and engineering, 3rd edition. Cambridge University Press; New York, 2006.

[55] P. Roura and J. Fort. Local thermodynamic derivation of young's equation. J. Colloid Interface Sci., 272(2):420–429, 2004.

[56] V. Srinivasan, V. K. Pamula, and R. B. Fair. An integrated digital microfluidic lab-on-a-chip for clinical diagnostics on human physiological fluids. Lab Chip, 4(4):310–315, 2004.

[57] X. Tan, J. Yang, P. Zeng, E. Kim, C. Huard, and M. Cheng. Electrowetting on flexible, transparent and conducting single-layer graphene. IEEE 25th Int. Conf. MEMS, pages 1037–1040, 2012.

[58] X. Tan, Z. Zhou, and M. M.-C. Cheng. Electrowetting on dielectric experiments using graphene. Nanotechnology, 23(37):375501, 2012.

[59] B. Toshev. Gibbs' thermodynamics of wetting. Int. J. Mech. Eng. Edu., 34(3):256–262, 2006.

[60] K. Vetter. Electrochemical kinetics: theoretical and experimental aspects. Academic Press: New York, 1967.

[61] T. Werder, J. Walther, R. Jaffe, T. Halicioglu, and P. Koumoutsakos. On the water-carbon interaction for use in molecular dynamics simulations of graphite and carbon nanotubes. J. Phys. Chem. B, 107(6):1345–1352, 2003.

[62] A. R. Wheeler. Putting electrowetting to work. Science, 322(5901):539–540, 2008.

[63] A. P. Willard and D. Chandler. Instantaneous liquid interfaces. J. Phys. Chem. B, 114(5):1954–1958, 2010.

[64] P. Xu, Y. Yang, S. Barber, M. Ackerman, J. Schoelz, I. A. Kornev, S. Barraza-Lopez, L. Bellaiche, and P. Thibado. Giant surface charge density of graphene resolved from scanning tunneling microscopy and first-principles theory. Phys. Rev. B, 84(16):161409, 2011.

[65] I.-C. Yeh and M. Berkowitz. Ewald summation for systems with slab geometry. J. Chem. Phys., 111(7):3155–3162, 1999.

[66] T. Young. An essay on the cohesion of fluids. Philos. Trans. R. Soc. London, 95:65–87, 1805.

[67] L. Zhao, R. He, K. Rim, T. Schiros, K. Kim, H. Zhou, C. Gutiérrez, S. Chockalingam, C. Arguello, L. Pálová, D. Nordlund, M. Hybertsen, D. Reichman, T. Heinz, P. Kim, A. Pinczuk, G. Flynn, and A. Pasupathy. Visualizing individual nitrogen dopants in monolayer graphene. Science, 333(6045):999–1003, 2011.

Chapter 3

Nonequilibrium Methodology for Simulating Fluid Flow

3.1 Introduction

Novel nanoporous membrane materials and geometries have become ubiquitous with the advancements made in nanoscale etching and material preparation.[1;19;25;34] Understanding fluid flow through nanochannels at a fundamental level is important for material design of nanofilters.[26;36] If fluctuations in the fluid density, temperature, and so on are smooth enough that continuum mechanics applies, hydrodynamics can describe, in great detail, the emergent velocity flow fields. On the molecular length scales appropriate for fluid flow through a two-dimensional sheet, however, fluctuations destroy these assumptions. While atomistic molecular dynamics is an invaluable tool for modeling systems at thermal equilibrium,[6;23] it remains rather unclear how to extend these simulation methods to systems that are driven from their thermal equilibrium.

If such driven systems are to maintain a steady-state, just as in thermal systems, there needs to be a balance between the driving force and its dissipation. Various methods for controlling temperature, for example, while seemingly straightforward, give spurious and incorrect results for some model systems.[3] This is the fundamental challenge this chapter addresses.

In systems at equilibrium, the steady-state is known by equilibrium statistical mechanics.[24] By maximizing the statistical entropy under various constraints, one obtains distribution functions for various ensembles. Likewise, in molecular dynamics simulations, placing constraints on the system leads to equations of motion not only consistent with the constraints, but that are also consistent with expectations for static distribution functions from statistical mechanics.

We propose an approach very similar to those mentioned. In our method, the current, rather than the gradient, is a constraint on the system. While in equilibrium systems, one can test the correctness of a method against its ability to generate known distribution functions, there is no such procedure for systems away from equilibrium. Steady-states are defined as having spatially-dependent quantities such as the density, temperature, and particle mass current that fluctuate about some fixed average values.[32] In nonequilbrium simulations a local steady-state thermodynamic equilibrium can be achieved, for example if the number of particles, temperature, and volume are held constant, as within the canonical ensemble.[24]

Fluid flow in molecular dynamics simulations has generally been performed using only two approaches, the piston and pump methods (§1.1.2).[22;39;43;44] These two methods are ad-hoc, but seem to give reasonable results in some model cases.[5;37;39] How closely these methodologies can simulate reality remains to be fully assessed. We will compare fluid flow simulations through select pipe-like channels using the pump method and what we will call the Gauss method, which we will develop below.

Fluid collisions with a membrane wall will exchange momentum and decrease the flow of the fluid. An external driving force must be applied to the fluid to maintain flow. The temperature of the system in the presence of an external driving force must be controlled using a thermostat or heat bath.[15] However, application of equilibrium thermostats to nonequilibrium simulations remains to be fully understood.[3;14] Naïve application of equilibrium thermostats to nonequilibrium simulations has been shown to give spurious results.[3;14]

Nonequilibrium flow simulations must maintain the Maxwell-Boltzmann distribution of velocities.[35] If "local equilibrium" holds, one expects that the microscopic velocity distribution at a (slowly-varying) spatial point in the fluid should be distributed as $P(\mathbf{v}) \sim exp\left[-(\mathbf{v}-\mathbf{u}(\mathbf{r},t))^2/k_BT\right]$, where $\mathbf{u}(\mathbf{r},t)$ is the streaming velocity of the fluid relative to the lab frame (Equation (3.15)).[13] The streaming velocity itself comes from a spatial and temporal averaging, or "coarse-graining," of the fluid motion. In equilibrium simulations, the Maxwell-Boltzmann distribution of velocities is centered about zero. In nonequilibrium flow simulations, the distribution of velocities will be centered

about a nonzero value while still maintaining the Maxwell-Boltzmann distribution. One expects the velocity for particle i to obey, $\mathbf{v}_i(t) = \delta\mathbf{v}_i(t) + \mathbf{u}(\mathbf{r}, t)$. The quantity $\delta\mathbf{v}_i(t)$ is the peculiar velocity and the streaming velocity $\mathbf{u}(\mathbf{r}, t)$ is the velocity that the fluid moves, on average, relative to the lab frame.

We will focus on fluid flow through two-dimensional pipe-like channels with widths between the molecular and nanoscopic scale. The fluid dynamics through small channels will have contributions due to the molecular nature of the particles. Larger channels should give results commensurate with that predicted by continuum mechanics.[2;7] Our goal is to develop an atomistic simulation methodology capable of giving results commensurate with that expected from continuum hydrodynamics while still maintaining velocity distributions from statistical mechanics.

Continuum hydrodynamics predicts that the fluid velocity profile is quadratic perpendicular the fluid flow direction.[7;28;29] This has been observed to break down for channel widths between five and ten molecular diameters, independent of the magnitude of the fluid flow.[40] However, as we will show, the linear relationship between the pressure gradient and the fluid mass transport through the channel predicted by Hagen-Poiseuille's law, a result from continuum hydrodynamics, still holds for small channels only several atoms wide.

3.2 Simulation Methodology and Theory

We developed a methodology for simulating steady-state nonequilibrium flow of a fluid. A constraint on the total velocity of the fluid was included into the equations of motion for the fluid particles. There are two types of constraints in classical mechanics, holonomic and nonholonomic.[17;30] If the constraints are holonomic, as in the case of bond distance constraints, for example, one minimizes the action with constraints using Langrange multipliers. Instead, the relevant cost function is not the Langrangian action but instead Newton's equation of motion. This method is called Gauss's principle of minimum constraint, and was first introduced into molecular dynamics simulations to maintain constant temperature.[9;12;13]

3.2.1 Gauss's Principle of Least Constraint for Flow

The total velocity of the fluid will be fixed and included as a hard constraint within the fluid equations of motion, along with a constraint on the temperature of the fluid. The resultant fluid flux through the pore will fluctuate about some value, proportional to the total flow of the simulation, but which cannot be known *a priori* as it depends on the channel properties, e.g. the channel length and width.

Gauss's principle of least constraint provides a powerful method yet relatively straightforward way to constrain the equations of motion in molecular dynamics simulations.[9;11;12;41;42] The principle states that the actual particle accelerations will be those that minimize a cost function, $\mathscr{C}$.[13] Given knowledge of the particle positions, the force on each particle, $\mathbf{F}_i$, is calculated according to the prescribed interatomic potential. The cost function can be written[13]

$$\mathscr{C}(\{\ddot{r}_\alpha\}) = \frac{1}{2}\sum_{i=1}^{N} m_i\left(\ddot{r}_{i,\alpha} - \frac{F_{i,\alpha}}{m_i}\right)^2 - \lambda_{flow,\alpha}g_{flow,\alpha} - \lambda_{T,\alpha}g_{T,\alpha}, \tag{3.1}$$

where m_i is the mass of particle i, $\{\ddot{r}_\alpha\}$ denotes the set of the acceleration component α for all particles, $\ddot{r}_{i,\alpha}$, N is the total number of fluid particles in the simulation, and $\lambda_{flow,\alpha}$ and $\lambda_{T,\alpha}$ are Lagrange multipliers[31] for the constraint on the flow, $g_{flow,\alpha}$, and temperature, $g_{T,\alpha}$.

The cost function in Equation (3.1) will be minimized with respect to the ith particle acceleration to find the unknown Lagrange multipliers that satisfy the constraints on the flow and temperature. We will write two constraints in terms of the particle accelerations and derive the equations of motion for the fluid particles. It is easiest to do this for each dimension separately. We will write the final equations of motion after we have solved for the unknown Lagrange multipliers.

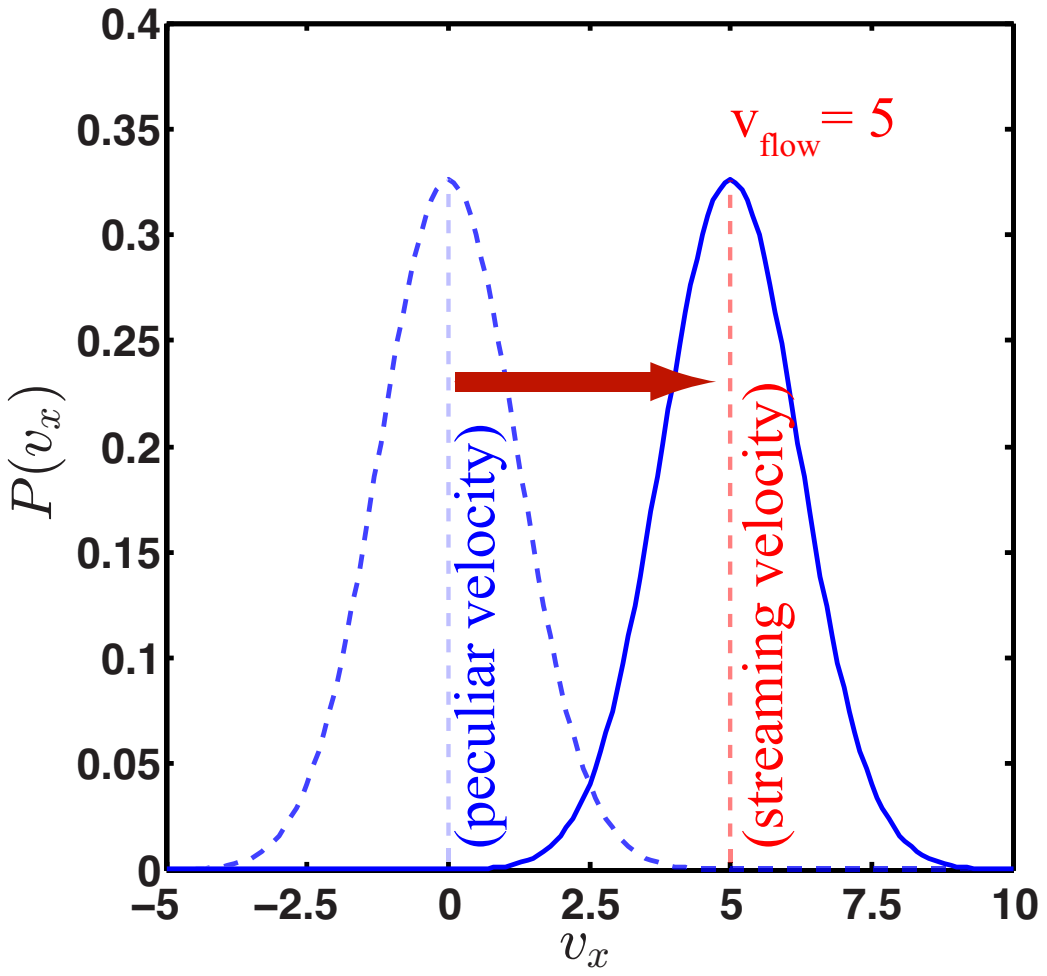

Figure 3.1: Peculiar and streaming velocities for a Lennard-Jones fluid. The peculiar velocity is defined with respect to the lab frame. In a system without flow, the Maxwell-Boltzmann distribution of velocities is centered about zero (blue dashed line). In a system under flow, the velocity distribution must maintain the Maxwell-Boltzmann distribution, however it will be centered about a nonzero value (red dashed line). The offset of the distribution is the added per-particle velocity, v_{flow}, initially assigned to each fluid particle. In this example $v_{flow} = 5$ (Lennard-Jones reduced units) for illustrative purposes. In practice, the shift of the distribution will be much smaller.

The constraint on the fluid velocity, written in the homogenous form, is

$$g_{flow,\alpha} \equiv \frac{d}{dt} \sum_{i=1}^{N} [\dot{r}_{i,\alpha} - u_\alpha(r_{i,\alpha})] = \sum_{i=1}^{N} \ddot{r}_{i,\alpha} = 0 \tag{3.2}$$

where $\dot{r}_{i,\alpha}$ is the velocity component α of particle i. As the fluid flows through the course of

the simulation, the total velocity will remain constant but will become redistributed amongst the particles. While there will be an overall flow of particles in one direction of the simulation, the average of local properties such as the density, temperature, or pressure will be constant, i.e. a steady-state will be achieved. Local streaming velocities will be established, thereby achieving a steady-state flow. Similarly, the constraint on the temperature is

$$g_{T,\alpha} = \frac{d}{dt}\sum_{i=1}^{N} m_i \left(\dot{r}_{i,\alpha} - u_\alpha(r_{i,\alpha})\right)^2 - Nk_bT = 0 \tag{3.3}$$

$$= \sum_{i=1}^{N} m_i \left(\dot{r}_{i,\alpha} - u_\alpha(r_{i,\alpha})\right) \cdot \ddot{r}_{i,\alpha} = 0. \tag{3.4}$$

Let us now turn to finding the equations of motion for the fluid particles under constraint Equation 3.2. Minimize the cost function, Equation (3.1), with respect to the acceleration component α of particle i,

$$\Rightarrow \frac{\partial}{\partial \ddot{r}_{i,\alpha}}\mathscr{C} = \left(\ddot{r}_{i,\alpha} - \frac{1}{m_i}F_{i,\alpha}\right) - \lambda_{flow} - \lambda_T m_i \left(\dot{r}_{i,\alpha} - u_\alpha(r_{i,\alpha})\right) = 0 \tag{3.5}$$

$$\Rightarrow \ddot{r}_{i,\alpha} = \frac{1}{m_i}F_{i,\alpha} + \lambda_{flow} + \lambda_T m_i \left(\dot{r}_{i,\alpha} - u_\alpha(r_{i,\alpha})\right) \tag{3.6}$$

$$\Rightarrow \sum_{i=1}^{N} \ddot{r}_{i,\alpha} = \sum_{i=1}^{N} \frac{1}{m_i}F_{i,\alpha} + \lambda_{flow}N + \lambda_T \sum_{i=1}^{N} m_i \left(\dot{r}_{i,\alpha} - u_\alpha(r_{i,\alpha})\right) = 0 \tag{3.7}$$

where in the last step we made use of the constraint, $g_{flow,\alpha}$. The distribution of particle velocities in the last term will be distributed according to a Gaussian distribution. Using the central limit theorem, as the number of fluid particles becomes large, we will assume that contributions due to this term are negligible.[31] Solving for the Lagrange multiplier, λ_{flow},

$$\Rightarrow \lambda_{flow,\alpha} = -\frac{1}{N}\sum_{j=1}^{N}\frac{F_{j,\alpha}}{m_j}. \tag{3.8}$$

We observe that the Lagrange multiplier for the flow constraint is a sum of all the interatomic forces acting on the fluid. As mentioned, we will fix the average temperature by application of a Nose-Hoover thermostat.[8;15] The Nose-Hoover thermostat is an extended Lagrangian method that fixes the average temperature and maintains the canonical distribution for systems at equilibrium.[15;24] For systems at nonequilibrium, subtracting off the local streaming velocity from the lab frame

velocities retains only the peculiar velocity contribution to the temperature and the distribution of velocities. The Lagrange multiplier for the Nose-Hoover thermostat is[15]

$$\lambda_{T,\alpha} = \xi \left[\dot{r}_{i,\alpha} - u(r_{i,\alpha}) \right] \tag{3.9}$$

where ξ is the Nose-Hoover thermodynamic friction coefficient.[10;15] The Nose-Hoover thermostat couples the system to a heat bath, that exchanges energy in an oscillatory fashion.[33] This is different from the constraint on the flow, which is a hard constraint that is satisfied at every timestep. The temperature will fluctuate about an average temperature. Finally, writing the equations of motion including the two constraints,

$$m_i \ddot{\mathbf{r}}_i = \mathbf{F}_i + \mathbf{f}_{add} - \xi \left[\dot{\mathbf{r}}_i - \mathbf{u}\left(\mathbf{r}_i\right) \right] \tag{3.10}$$

where the additional force, $\mathbf{f}_{add} = -\frac{1}{N} \sum_{i=1}^{N} \mathbf{F}_j$. This force can be interpreted as a fluctuating gravitational field. The additional force performs work on the fluid to maintain the prescribed flow, against the virtual work that the membrane, fixed in space, does on the fluid. The term, $\xi \left[\dot{\mathbf{r}}_i - \mathbf{u}(\mathbf{r}_i) \right]$, is a profile-unbiased implementation of the Nose-Hoover thermostat, which acts only on the peculiar part of the velocity of each particle.[14] Subtracting off the local streaming velocity permits application of the usual Nose-Hoover thermostat.[10;15] The term "profile unbiased" means that the thermostat damps motion relative to the streaming velocity, not the lab frame.[10] Previous work has shown that this feature corrects spurious predictions from "non Gallilean invariant" thermostats.[18] Typical nonequilbrium simulations use a profile-biased thermostat, where the local streaming velocity is assumed to be linearly proportional to the shear of the fluid.[13;16] It has been shown that profile-biased thermostats can lead to artificial alignment of fluid particles in large flows.[14] This could affect particle dynamics through the channels in uncontrollable ways.

There are a number of thermostatting schemes possible for simulations involving fluid passage through a membrane.[3] One can set up simulations that thermostat the fluid and keep the membrane fixed,[44] or one can thermostat the membrane and let the fluid dissipate energy through collisions with the membrane.[16] We chose to thermostat the fluid while keeping the membrane

rigid. Using the profile-unbiased Nose-Hoover thermostat allows the fluid to reach steady-state flow while still allowing the system to develop unbiased and natural velocity streamlines. The strength of performing the simulations this way is that we need not assume any form of the velocity profiles or temperature gradients, but simply allow the fluid to move according to the equations of motion. Equation 3.10 was used for all Gauss method simulations presented in this chapter.

3.2.2 System Geometry and Simulation Description

To characterize the Gauss method, a fluid and pipe-like membrane system composed of Lennard-Jones particles was studied. Simulations were performed in two dimensions to minimize particle number and reduce computational cost. The basic system geometry is shown in Figure 3.2, and is composed of a fixed membrane with a channel of a prescribed length, L_{pipe}, and width which we denote d_{pipe}, in analogy to a pipe diameter in three dimensions. The system is periodic in both dimensions. When a nonequilibrium mass flux is induced in the $+\hat{x}$ direction, fluid particles may pass only through the channel at the center of the simulation box. The membrane is composed of a face-centered-cubic lattice chosen such that fluid particles cannot pass through the membrane wall. The fluid-channel interactions were modeled using the Weeks-Chandler-Anderson potential, which is a purely repulsive potential.[4]

Fluid particles were initially placed on a cubic lattice with velocities chosen from the Maxwell-Boltzmann distribution.[15;24] A prescribed additional velocity, v_{flow}, was added to each fluid particle. This defines a total flow for the simulation that is kept constant for each timestep of the simulation.

The temperature of the fluid particles was maintained using a profile-unbiased[14] implementation of the Nose-Hoover thermostat with a spatially prescribed local grid scheme to define a local temperature (see Appendix §3.5.1 for more details).[21] The channel particles were held fixed throughout the simulation. Slight differences have been observed for simulations that thermostat the fluid compared to those that thermostat the membrane.[3]

We will compare simulation results from both the pump and Gauss methods. See §1.1.2 for a

discussion of the pump method. All flow is produced in the $+\hat{x}$ direction. The input parameters for the two methods are different. Therefore, individual simulations between the two methods cannot be easily compared. In the spirit of simulations already reported in the literature,[22;37;38;44] we report the studied pump simulations in terms of the external force applied, $\mathbf{f}_{ext} = 0.0, 0.1, 0.3, 0.5, 1.0\hat{x}$. For the Gauss method we studied $\mathbf{v}_{flow} = 0.0, 0.01, 0.02, 0.03, 0.04\hat{x}$. All units are in reduced Lennard-Jones units. Additional simulation details are provided in Appendix §3.5.1.

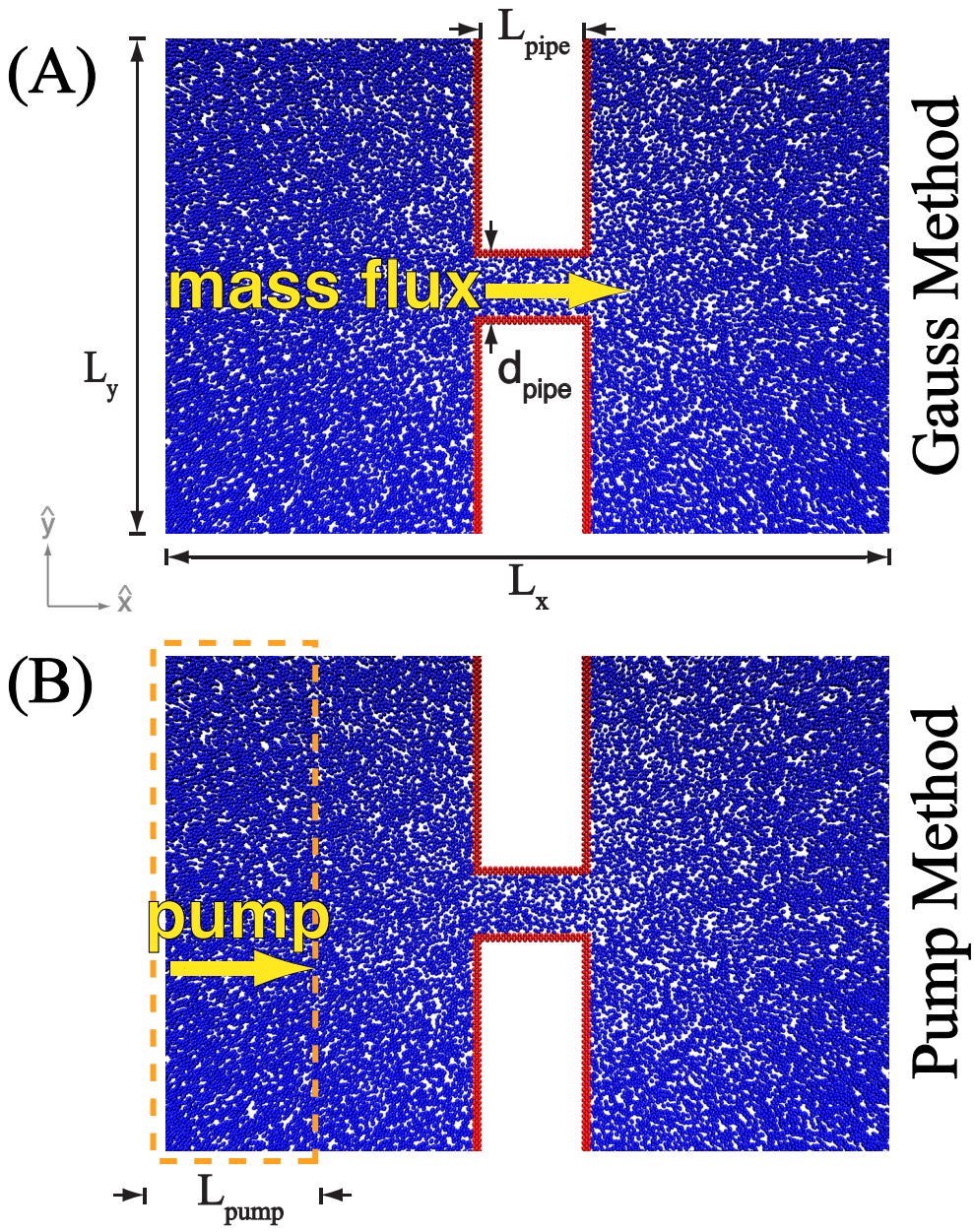

Figure 3.2: Two nonequilibrium methods for studying flow through nanoscopic channels. L_{pipe} and d_{pipe} are the channel length and width respectively. L_x and L_y are the total lengths of the simulation box. (A) In the Gauss method, an additional force is applied to all particles to maintain the constraint on the total velocity of the fluid particles and produce a mass flux in the $+\hat{x}$ direction. (B) In the pump method, an external force is applied to fluid particles occupying a prescribed pump region, of prescribed width L_{pump}. Membrane atoms are in red, and the fluid particles are in blue. The membrane atoms are held fixed throughout the simulations for computational efficiency.

3.3 Results and Discussion

The implementation of the Gauss method according to Equation 3.10 was studied for the Lennard-Jones fluid and channel system shown in Figure 3.2. The simulation box extends well beyond the vicinity of the membrane. It is important to have a large reservoir of fluid particles that extends well beyond the vicinity of the membrane to avoid finite size effects of the simulation. First and foremost, the constraint on the total fluid velocity according to Equation 3.2 was satisfied at every timestep of the simulation. The total fluid momentum in the x dimension was held constant throughout the simulation runs.

The additional external force shows small fluctuations throughout the course of the simulation, see Figure 3.3. Although the flow is taken to be only in the $+\hat{x}$ direction, we applied a corrective force for both dimensions. We observe that the corrective force is of a similar magnitude in both the x and y dimensions.

The velocity field in the vicinity of the channel is shown in Figure 3.4 for Gauss method simulations. As the flow increases, the velocity field streamlines extend beyond the vicinity of the channel, stretching out into the fluid reservoirs on either side of the membrane. The persistence of the velocity streamlines require the use of large box dimensions for the simulations in order to minimize artificial correlations between fluid particles across the periodic x dimension. Navier-Stokes is a statement of Newton's second law for fluid.[7] For an incompressible fluid,*

$$\nabla \mathbf{P} = \mathbf{f} - \rho \frac{D}{Dt}\mathbf{v} \tag{3.11}$$

where $\nabla \mathbf{P}$ is the gradient of the pressure tensor, ρ is the density of the fluid, $\mathbf{v}$ is the fluid velocity, $D/Dt = \partial_t \mathbf{v} + \mathbf{v} \cdot \nabla \mathbf{v}$ is the material derivative, and $\mathbf{f}$ is any external force applied to the fluid. For the pump method, $\mathbf{f} = \mathbf{f}_{ext}$, and for the Gauss method $\mathbf{f} = \mathbf{f}_{add}$. The pressure is calculated from the velocity streamlines using the method-of-planes.[20]

Navier-Stokes predicts that the larger the gradient in the velocity field, the larger the gradient in the pressure. As the flow increases in Figure 3.4, the pressure gradient is therefore expected to

* For an incompressible fluid the density remains constant, or equivalently that $\nabla \cdot \mathbf{v} = 0$.

increase. We will show later on that this is indeed the case (Figure 3.8).

The center of mass velocity is well maintained throughout the course of the simulation (Figure 3.5). This is to be expected because the additional force is applied homogeneously to every fluid particle in the system. If the additional flow per particle is subtracted, v_{flow}, the center-of-mass velocity for both the x and y dimensions is seen to be on the order of numerical precision. Importantly, the Gauss method maintains the Maxwell-Boltzmann distribution of velocities (Figure 3.10).

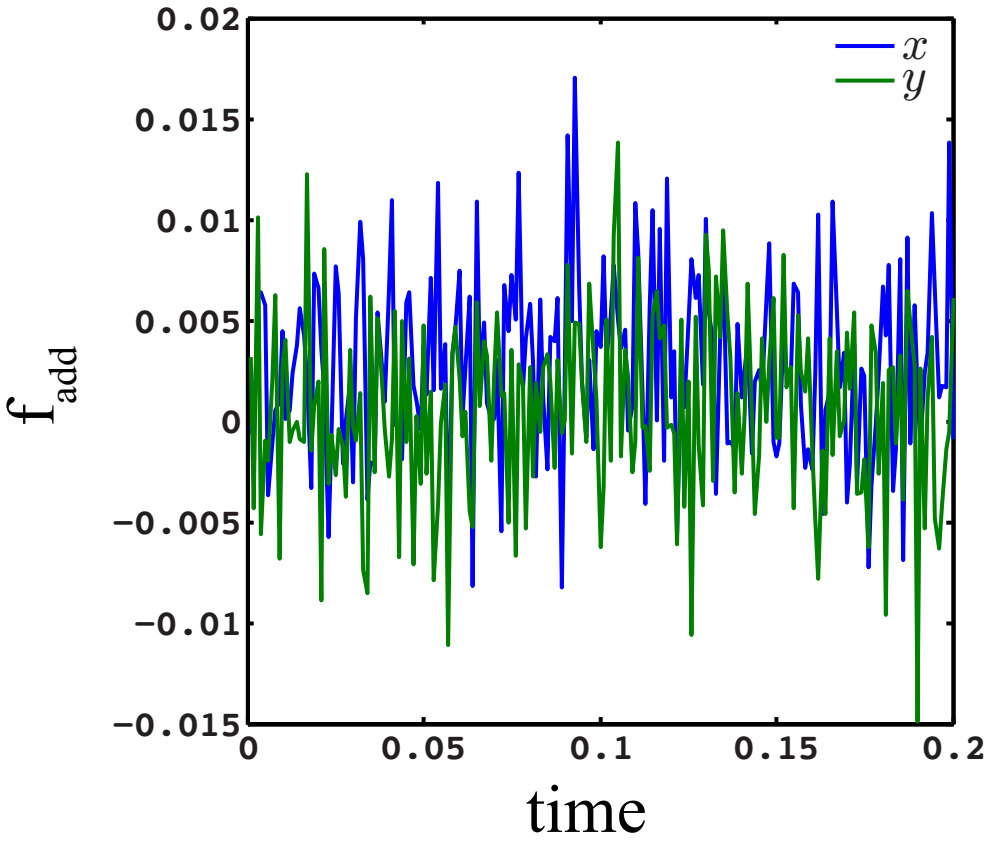

Figure 3.3: Additional nonequilibrium constraint force for constant flow as a function of time. $\mathbf{f}_{add}$ is the additional force added to each fluid particle in the simulation, given by Equation 3.10. For the data shown, $f_{add,x} = (1.28 \pm 14.1) \times 10^{-2}$ and $f_{add,y} = (-9.29 \pm 132.) \times 10^{-2}$. This data is for the channel shown in Figure 3.2, with $v_{flow} = 0.04$, $L_{pipe} = 37.57$ and $d_{pipe} = 20.00$.

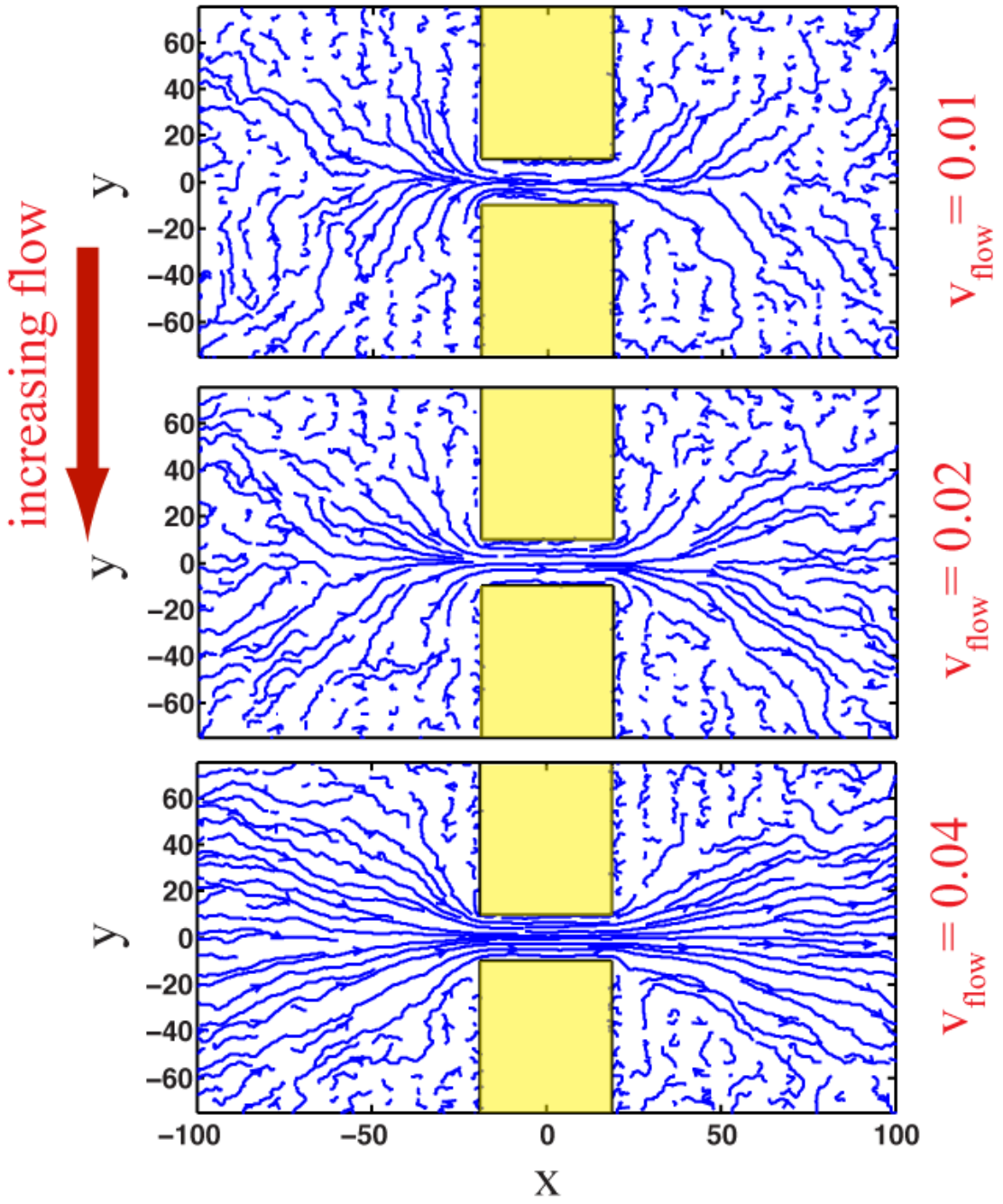

Figure 3.4: Velocity flow field with increasing nonequilibrium fluid flow through a channel of length, L_{pipe} = 37.57, and width, d_{pipe} = 20.00 using the Gauss method. v_{flow} is the initial additive per-particle velocity assigned at the start of the simulation. The direction of flow is in the $+\hat{x}$ direction. The simulation box is larger than the area shown (L_x = 327.57,L_y = 227.04). Velocity fields from the pump method simulations are qualitatively similar (not shown).

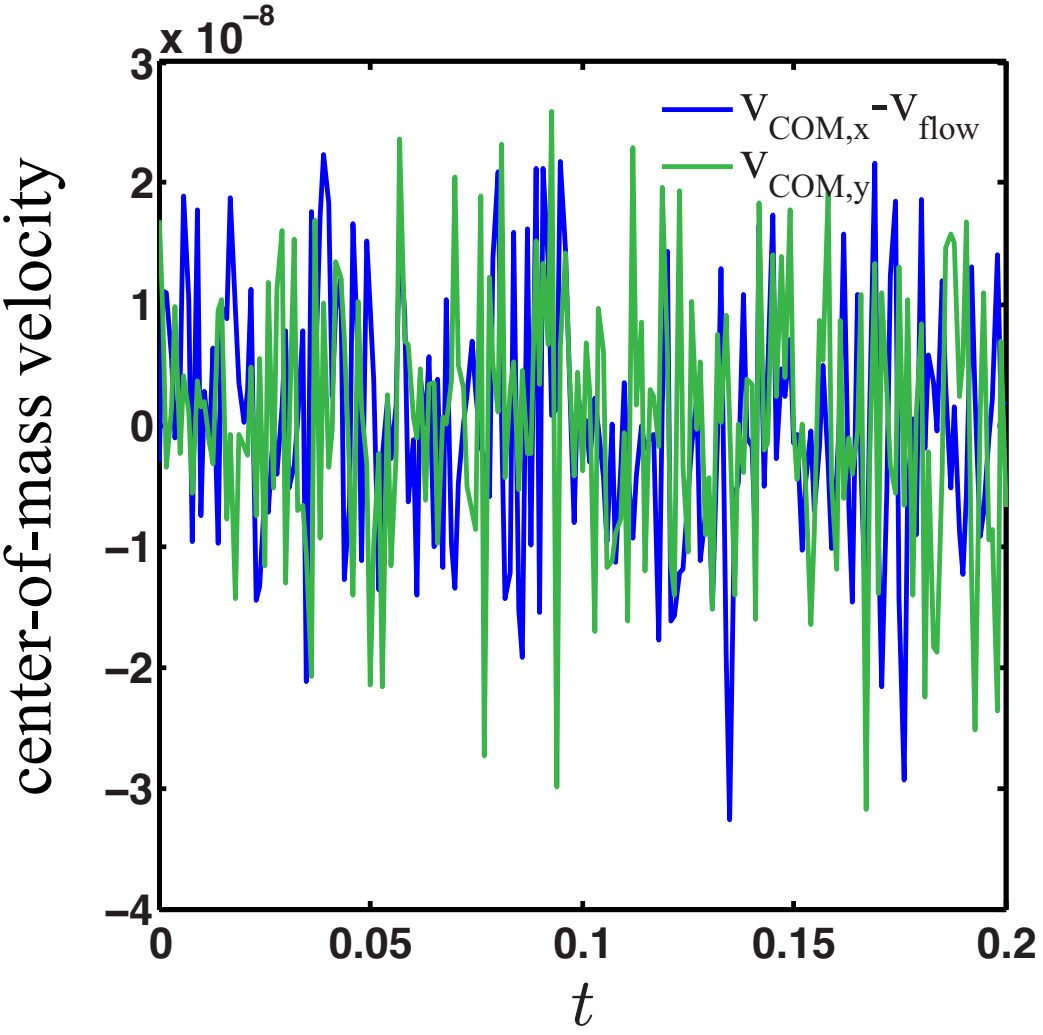

Figure 3.5: Center-of-mass velocity as a function of time. The center-of-mass velocity is well maintained throughout the simulation in both the x and y dimensions. The nonequilibrium flow in the $+\hat{x}$ direction, v_{flow}, is subtracted off the x component of the center-of-mass velocity, $v_{COM,x}$ for ease of comparison. Similar fluctuations are seen for the y component center-of-mass velocity, $v_{COM,y}$. Fluctuations about zero for both components are on the order of numerical precision.

3.3.1 Comparison of Gauss Method with Pump Method

Continuum hydrodynamics predicts that the velocity component parallel the direction of flow is quadratic along the direction perpendicular the flow, cf. Equation (3.61).[7;28;29] Figure 3.6 shows

that this is indeed the case for both the Gauss and pump simulations studied with $d_{pipe} = 20.00$. The velocity profile deviates from this prediction for $d_{pipe} = 5.00$, as expected due to the atomic size of the channel. For the smaller channel, it appears that particle packing plays a role. The velocity profile exhibits oscillations or bumps commensurate with the particle size. This has also been seen previously for channels between five and ten molecular diameters.[40]

In the current implementations, we note that there is no direct way to set up quantitatively comparable Gauss and pump simulations. The fluid flow in the channel depends on the geometry of the channel. One could develop a method whereby a subvolume of the simulation is used to adjust the applied force and thereby the fluid flux, but is beyond the scope of the current work. The Gauss method requires a prescribed v_{flow}, which determines the total velocity of the simulation. For the pump method, the external force $\mathbf{f}_{ext}$ is defined and applied to a prescribed region well away from the channel. The pressure or density gradient, along with the flow of the fluid, are developed as a result of these prescriptions. If the channel length, L_{pipe}, or width, d_{pipe}, is changed so too will the pressure and flux.

The temperature of the simulations for both methods are well maintained at the prescribed temperature (Figure 3.7). The temperature is shown as a function of x, along the direction of flow for two selective slices in y. The temperature was calculated according to Equation (3.17). The temperature for the nonequilibrium simulations exhibit a temperature gradient in the vicinity of the channel, that is hard to quantity given the statistical noise. The pump simulation, $\mathbf{f}_{ext} = 0.3\hat{x}$, was chosen such that total flow is qualitatively comparable to the Gauss method simulation with $\mathbf{v}_{flow} = 0.04\hat{x}$. As mentioned, it is not possible to have quantitatively comparable simulations for the two methods. It is worth noting that the temperature gradient inside the channel is larger for higher magnitudes of flow (not shown).

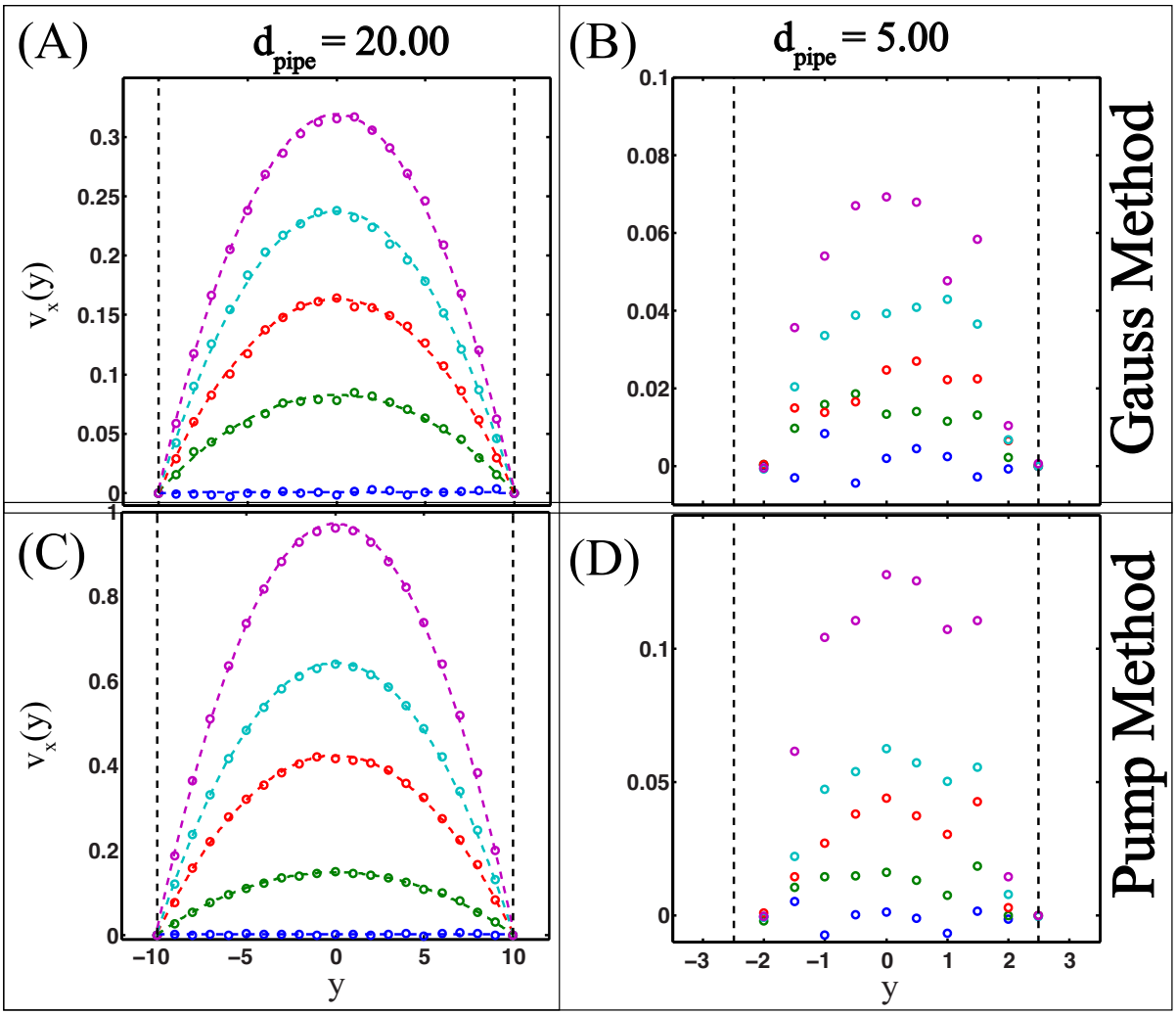

Figure 3.6: Fluid velocity profile in the channel as a function of the dimension perpendicular the $+\hat{x}$ fluid flow. (A,B) Gauss method simulations, with $\mathbf{v}_{flow} = 0.0, 0.01, 0.02, 0.03, 0.04\hat{x}$ going from bottom to top respectively. (C,D) Pump method simulations, with $\mathbf{f}_{ext} = 0.0, 0.1, 0.3, 0.5, 1.0\hat{x}$ going from bottom to top respectively. The velocity profiles for both methods are quadratic for the larger pipe, $d_{pipe} = 20.00$ (A,C), as expected from continuum hydrodynamics, cf. Equation (3.64). Circles are data and the dashed lines are quadratic fits. The profiles are nonquadratic for simulations with $d_{pipe} = 5.00$ (C,D). The velocity data shown here are taken from the same simulations as that appearing in Figure 3.8.

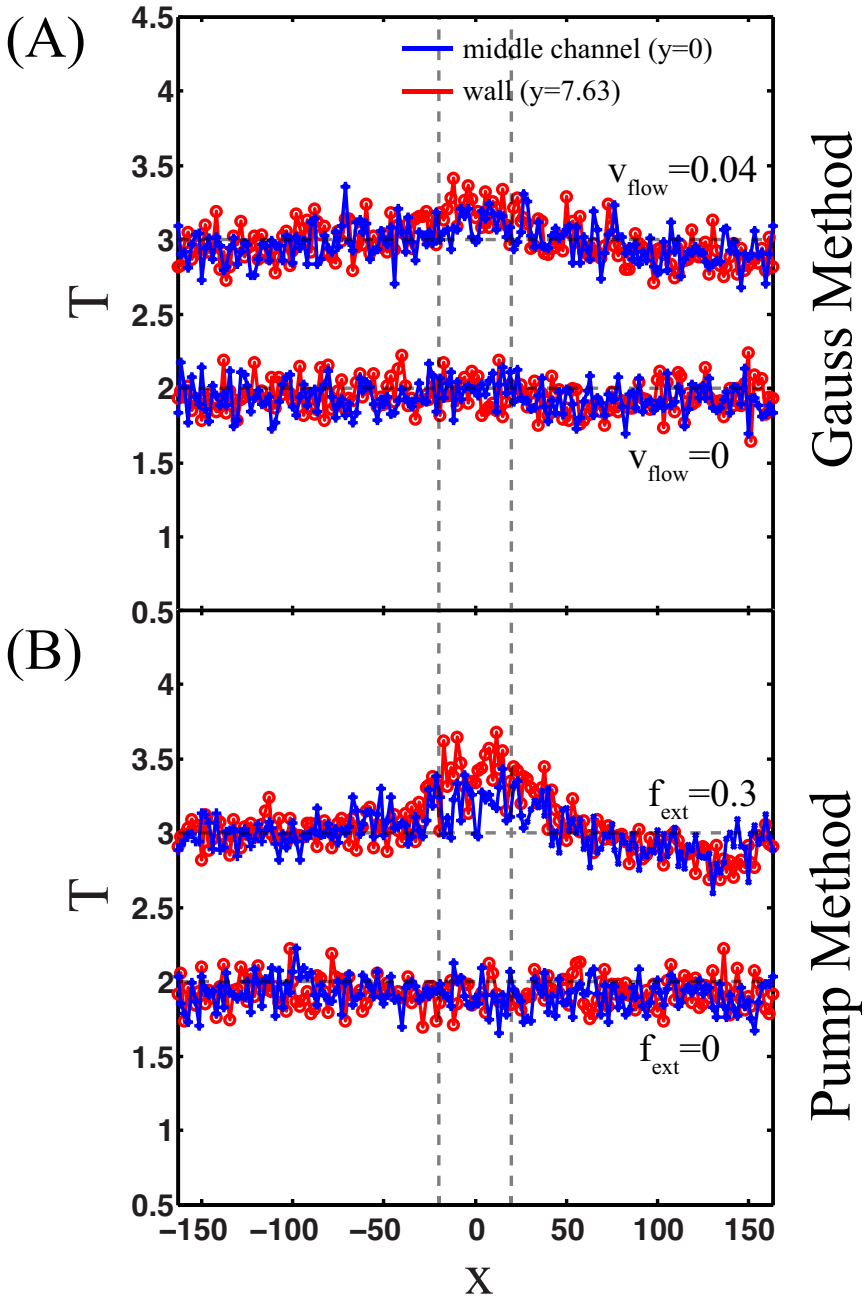

Figure 3.7: Temperature, T, as a function of x, along the direction of flow, for both Gauss (A) and pump (B) simulations. The temperature was calculated according to Equation (3.17). The temperature data for nonzero flow simulations (v_{flow} = 0.04 and f_{ext} = 0.3), are offset from the prescribed temperature, T = 2.0 for clarity. For nonzero fluid flow the temperature is observed to slightly rise inside the channel. Vertical dashed lines show the boundaries of the channel. The data is shown through the middle of the channel (y=0, blue line), and near the channel wall (y=7.63, red line).

3.3.2 Hagen-Poiseuille's Law for Gauss and Pump Method Simulations

The pressure gradient inside the channel was calculated using Equation 3.16. Statistical noise is greater in the density (not shown) than in the pressure. The microscopic flux was calculated from numerical integration of the velocity profile according to Equation 3.64. Hagen-Poiseuille's law for an incompressible fluid predicts a linear relationship between the flux and pressure gradient.[2] Figure 3.8 shows that this is indeed the case for both channel geometries studied for both the Gauss and pump simulations.

An overview of the two methods is provided in Table 3.1. The Gauss and pump methods each have advantages and disadvantages. Both methods are incapable of prescribing a fluid flow *a priori* inside the channel because it depends on the channel geometry, and exhibit a linear relationship between the flux J and change in pressure ΔP. Both methods are difficult to converge with respect to simulation box dimension (not shown).

One distinct advantage of the Gauss method is that the simulation requires only one parameter, v_{flow}. Prescribing v_{flow} is the same as fixing the total momentum of the fluid, that is held constant throughout the simulation. The particles are then propagated according to the equations of motion. This is in contrast to the pump simulations that require a prescribed external force, the width of the pump region, and the pump position. However, the flow range is larger for the pump method than the Gauss method. For higher v_{flow} than those presented, the density in the Gauss method simulation oscillates wildly and the density is depleted on the exit side of the channel (not shown). Care must therefore be taken in choosing v_{flow} so as to not excessively drive the simulation.

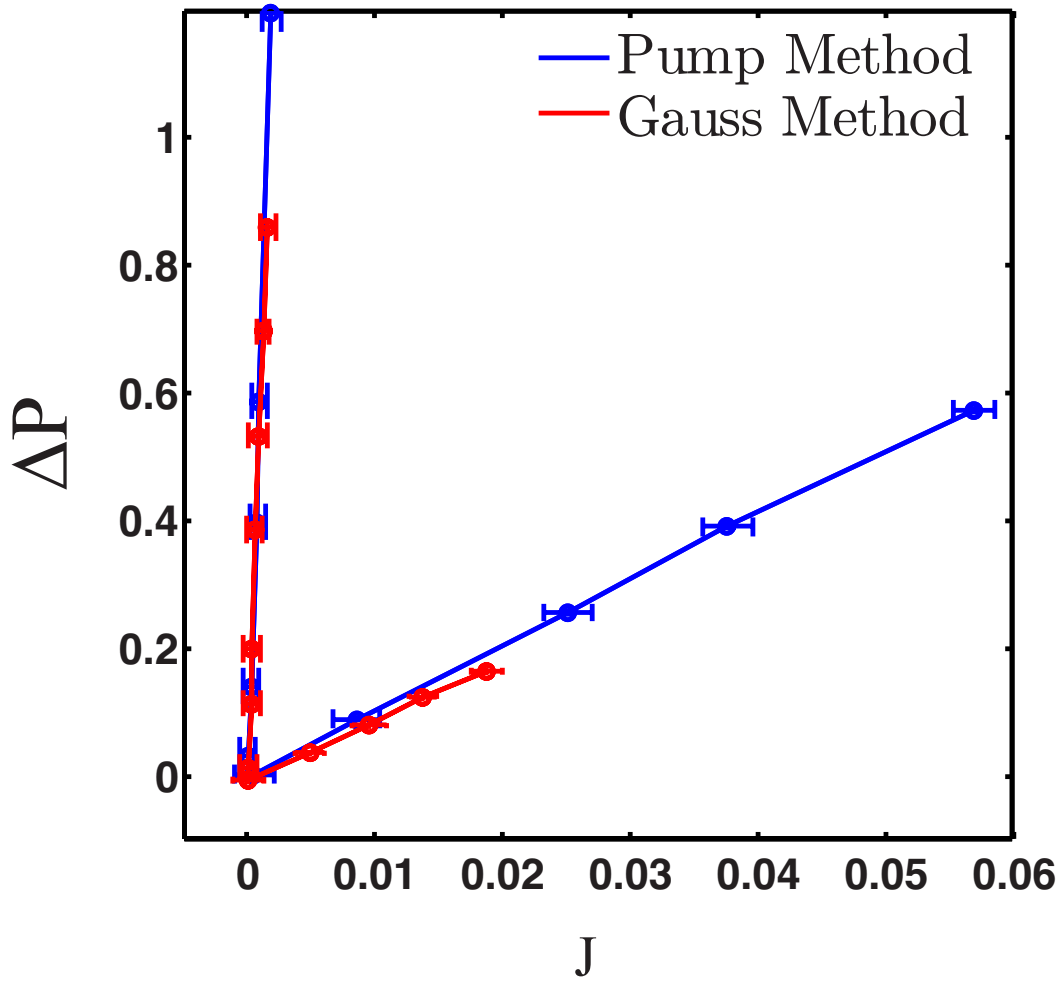

Figure 3.8: Fluid flux, J, versus change in pressure, ΔP, for both Gauss and pump method simulations. The data for the two pipes follows a linear relationship as expected from Hagen-Poiseuille's law, Equation (3.64). Both the Gauss and pump methods are seen to exhibit the linear trend expected from the Hagen-Poiseuille law. For the two pipe dimensions studied, the two methods are seen to qualitatively agree for the range of flux studied here. Error bars are one standard deviation, and are shown for both dimensions. The uncertainty in J is much larger than the uncertainty in ΔP (difficult to see on this scale). The flux was calculated according to Equation 3.64.

	Gauss Method	Pump Method
Advantages	• density relaxes naturally throughout the simulation	• driving force prescribed in terms of the chemical potential difference between two sides of a membrane. • mimics a hydrostatic pressure.
Disadvantages	• smaller accessible flow range	• pump needs to be "far enough away" from membrane • discontinuity in potential

Table 3.1: Comparative summary of the Gauss and pump methodologies. The pump method prescribes a region in which particles experience a discontinuity in the potential. This causes a sudden change in the density near the vicinity of the pump. In contrast, the density in the Gauss method simulations relax naturally throughout the simulation. The pump method has the advantage that it mimics a hydrostatic pressure. However, one needs to prescribe the size of the pump region. In practice it is nontrivial to prescribe this region such that fluid dynamics in the channel are independent of its size or location. The Gauss method is applicable to smaller flow ranges. If a system is prescribed with an excessively large v_{flow}, the density shows wild oscillations in the density (not shown).

3.4 Conclusion

A steady-state nonequilibrium flow of a Lennard-Jones fluid was simulated using molecular dynamics with a constraint on the total flow of the simulation using Gauss's principle of least constraint. The method defines the total momentum of the fluid as a constant of the simulation, and is held constant at each timestep. The method was shown to be comparable to simulations

where an external force is applied to a region of the simulation commonly used in the literature. Importantly, the Maxwell-Boltzmann distribution of velocities was maintained for the developed method. The quadratic velocity profile expected from continuum hydrodynamics was observed for both methods applied to a pipe-like channel with width 20.00. Hagen-Poiseuille's law, that predicts a linear relationship between the flux and pressure gradient, was confirmed for channel widths of 20.00 and 5.00 using both the pump and Gauss methods. The developed method will allow for further study of nonequilibrium fluid flow through nanoscopic channels.

3.5 Appendix

3.5.1 Additional Simulation Details

Unless otherwise specified, all Lennard-Jones fluid and channel simulations were performed with the set of parameters provided in Table 3.2. All simulations were performed using a modified version of the LAMMPS molecular dynamics software.[27]

The potential between the fluid particles was modeled using the Lennard-Jones 12-6 potential, with a hard cutoff at 2.5.

$$V_{Lennard-Jones}(r) = 4\epsilon_{fluid-fluid}\left[\left(\frac{\sigma_{fluid-fluid}}{r}\right)^{12} - \left(\frac{\sigma_{fluid-fluid}}{r}\right)^{6}\right] \tag{3.12}$$

where r is the interatomic distance between fluid particles, and $\epsilon_{fluid-fluid}$ is the potential well depth. Similar to Reference 16, we modeled the fluid-channel interactions using the Weeks-Chandler-Anderson (WCA) potential,[4]

$$V_{WCA}(r) = 4\epsilon_{fluid-channel}\left[\left(\frac{\sigma_{fluid-channel}}{r}\right)^{12} - \left(\frac{\sigma_{fluid-channel}}{r}\right)^{6}\right] + \epsilon \qquad \text{for } r < 2^{1/6}\sigma, \tag{3.13}$$

with $V_{WCA}(r \geq 2^{1/6}\sigma) = 0$. The addition of ϵ makes the WCA potential a purely repulsive potential.

The initial density, ρ_0 was calculated using a similar convention as Muller et al.,[16]

$$\rho_0 = \frac{N_{fluid}}{A_{accessible}} = \frac{N_{fluid}}{L_x L_z - \left(L_{pipe} + 2\sigma\right)\left(L_z - d_{pipe} + 2\sigma\right)} \tag{3.14}$$

where N_{fluid} is the number of fluid particles and $A_{accessible}$ is the area accessible to the fluid. The subtraction of 2σ is an approximation to account for the repulsion of the membrane walls. Table 3.2 provides additional simulation parameters.

L_{pump}	a_{memb}	ρ_0	$\sigma_{fluid-fluid}$	$\sigma_{fluid-channel}$	$\epsilon_{fluid-fluid}$	$\epsilon_{fluid-channel}$	m_{fluid}	T
5.0	1.7472	0.545	1.0	1.0	1.0	1.0	1.0	2.0

dt	t_{damp}
0.001	0.05

Table 3.2: Simulation parameters for Lennard-Jones for fluid and channel systems. All parameters are given in the standard Lennard-Jones reduced units. L_{pump} is the length of the pump region as defined in Figure 3.2, a_{memb} is the lattice constant of the face-centered-cubic channel membrane, ρ_0 is the initial simulation density calculated according to Equation (3.14), the various σ's and ϵ's denote the Lennard-Jones 12-6 potential's inter-particle distance and well depth respectively, m_{fluid} is the mass of the fluid particles, T is the overall temperature of the fluid, dt is the simulation time step, and t_{damp} is the Nose-Hoover thermostat damping coefficient.

The streaming velocity corresponds to the shift of the center for the Maxwell-Boltzmann velocity distribution (Figure 3.1),

$$\mathbf{u}(\mathbf{r},t) = \frac{1}{\rho(\mathbf{r})}\sum_{i\in E(\mathbf{r})} m_i\dot{\mathbf{r}}_i\delta\left(\mathbf{r}-\mathbf{r}_i\right) = \frac{\sum_{i\in\Omega(\mathbf{r})} m_i\dot{\mathbf{r}}_i\delta\left(\mathbf{r}-\mathbf{r}_i\right)}{\sum_{i\in\Omega(\mathbf{r})} m_i\dot{\mathbf{r}}_i\delta\left(\mathbf{r}-\mathbf{r}_i\right)}. \tag{3.15}$$

3.5.2 Pressure in Channel

The pressure drop across the channel is a key quantity for characterizing the flow through our channel geometries, and should be proportional to the density drop. We need only concern ourselves with the pressure drop in the direction of flow, taken to be the $\pm\hat{x}$ direction, and therefore need only calculate the pressure tensor component $\bar{p}_{xx}$ (Reference 20, Equation 8). In two dimensions

$$\bar{p}_{xx}(d_{pipe},x) = \frac{1}{d_{pipe}\Delta x}\langle\sum_{i\in(d_{pipe}\Delta x)} m_i v_{i,x}^2\rangle + \frac{1}{2d_{pipe}}\langle\sum_{x_n\cap L_y(x)}\sum_{i=1}^{N} F_{ix}sgn(x_i-x)\rangle \tag{3.16}$$

where F_{ix} is the x component of the force on atom i, and $L_y(x)$ is the line perpendicular the flow between the point x and x_i. Figure 3.9 shows pictorially how we discretize space inside the channel to calculate the pressure. F_{ix} includes only those interactions which dissect the line $L_y(x)$.

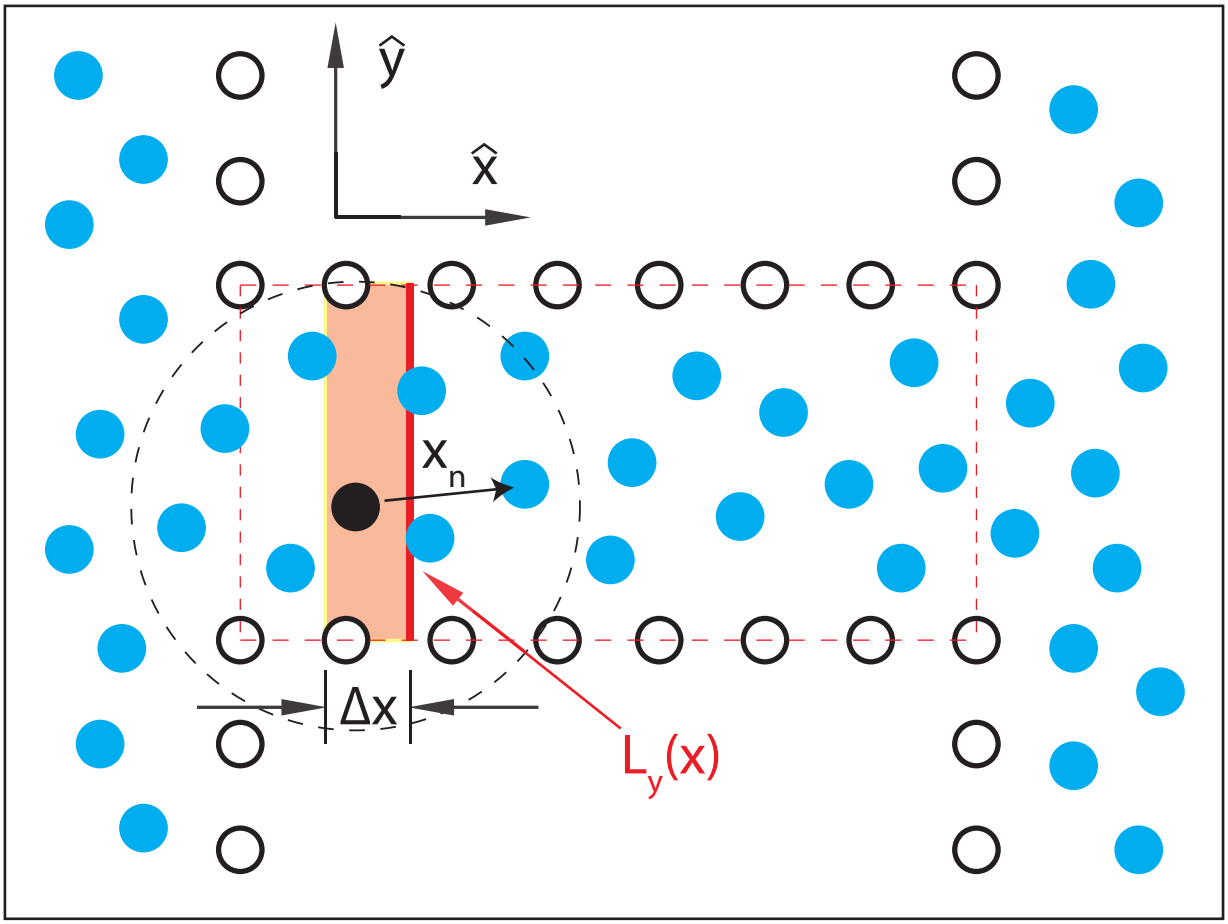

Figure 3.9: Calculating pressure as function of x in the channel configuration. Particles inside the pipe are enclosed in the red dashed rectangle, drawn between atom centers of the channel. The black dashed circle illustrates the Lennard-Jones cutoff. All forces acting on the chosen particle within the dashed circle would be included, i.e. the particle in a given slab will experience a force from channel atoms and those outside the pipe if they are within the Lennard-Jones cutoff.

3.5.3 Additional Physical Quantities

3.5.3.1 Maxwell-Boltzmann Distribution of Velocities

Simulations performed using the Gauss method maintain the Maxwell-Boltzmann distribution of velocities (Figure 3.10). The data presented in Figure 3.10 was taken from simulation of a channel with a width of 44σ and $v_{flow} = 0.4$. Particles near the channel wall and in the middle of the channel maintain a Gaussian-shaped distribution.

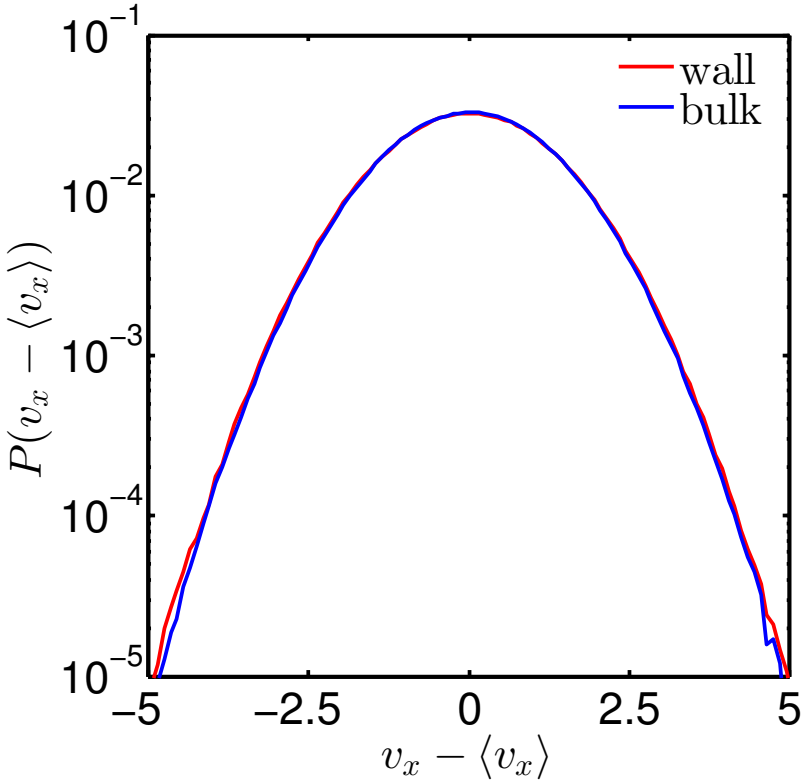

Figure 3.10: Maxwell-Boltzmann distribution of velocities for flow through a pipe using Gauss method with $v_{flow} = 0.4$. The distribution is Gaussian near the channel wall (red line) and in the middle of the channel (blue line) as expected. This data was taken from simulation of a channel with a width of 44σ. The channel extended across the periodic dimension in the direction of flow in order to gather good statistics.

3.5.3.2 Temperature

The local temperature was calculated using

$$T(x,y) = \langle \frac{1}{N_{dof}} \frac{\sum_{i=1}^{N} \delta(x-x_i)\delta(y-y_i)m_i v_i^2}{N(x,y)} \rangle \tag{3.17}$$

where the angle brackets denote a time average, and N_{dof} the number of degrees of freedom (2 for the two-dimensional simulations). The total number of particles was calculated

$$N(x,y) = \sum_{i=1}^{N} \delta(x-x_i)\delta(y-y_i). \tag{3.18}$$

3.5.3.3 Microscopic Fluid Flux

The fluid flux was calculated from trajectory positional and velocity data. The number of particles passing through per unit time, dN/dt, can be written, in three dimensions

$$\frac{dN}{dt} = \int dV \left(\vec{\nabla} \cdot \vec{J}\right) = \int d\vec{A} \cdot \vec{J} = \int dA \hat{n} \cdot \mathbf{J} \tag{3.19}$$

$$= \int dx \int dy\, \rho(x,y) v_x + \int dx \int dz \rho(x,z) v_y + \int dy \int dz \rho(y,z) v_x \tag{3.20}$$

$$[=] length^2 \frac{1}{length^3} \frac{length}{time} = \frac{1}{time} \tag{3.21}$$

where we made use of the divergence theorem (also known as Gauss's theorem). To be clear, since one dimension had to be integrated over,

$$\rho(\alpha,\beta) = \frac{1}{L_\gamma} \sum_{i=1}^{N} \delta(\alpha-\alpha_i)\delta(\beta-\beta_i)\ [=] \frac{1}{volume} \tag{3.22}$$

where $\alpha, \beta, \gamma = x, y$ or z. This has the correct dimensions. Now, in two dimensions

$$\frac{dN}{dt} = \int dA\, (\nabla \cdot \mathbf{J}) = \oint_C ds\ \hat{n} \cdot \mathbf{J} \tag{3.23}$$

$$= \int dx\, \rho(x) v_y + \int dy\, \rho(y) v_x \tag{3.24}$$

$$[=] length \frac{1}{length^2} \frac{length}{time} = \frac{1}{time}, \tag{3.25}$$

where again, being explicit

$$\rho(\alpha) = \frac{1}{L_\beta} \sum_{i=1}^{N} \delta(\alpha-\alpha_i)\ [=] \frac{1}{area}, \tag{3.26}$$

where an integration was already performed over one of the dimensions. We are only interested in the flux associated with the flow in the x dimension, and so define

$$\frac{dN_x(x,y)}{dt} = \int_{y-\Delta y/2}^{y+\Delta y/2} dy' \rho(x,y') v_x \; [=] \frac{1}{time} \tag{3.27}$$

$$\Rightarrow J_x(x) = \int dy \; \frac{dN_x(x,y)}{dt} = \int dy \left\{ \int_{y-\Delta y/2}^{y+\Delta y/2} dy' \rho(x,y') v_x \right\} [=] \frac{length}{time} \tag{3.28}$$

$$= \int dy \left\{ \int_{y-\Delta y/2}^{y+\Delta y/2} dy' \sum_{i=1}^{N} \delta(x - x_i)\delta(y' - y_i) v_{xi} \right\}. \tag{3.29}$$

3.5.4 Hagen-Poiseuille's Law for Fluid Flow

3.5.4.1 Circular Pipe in 3D

The parabolic velocity for a 3D circular pipe is (with flow in the $\hat{z}$ direction) (2, 10-21)

$$u_z(r) = \frac{1}{4\mu} \frac{dp}{dz} \left(r_0^2 - r^2 \right). \tag{3.30}$$

Integrating the velocity over the pipe area to get the volumetric flux,

$$Q = \int_0^{r_0} dr \; 2\pi r u_z(r) = 2\pi \int_0^{r_0} dr \; \left[\frac{1}{4\mu} \frac{dp}{dz} \left(r r_0^2 - r^3 \right) \right] = \frac{\pi}{2\mu} \frac{dp}{dz} \left[r_0^2 \frac{r^2}{2} - \frac{r^4}{4} \right] \Bigg|_{r=0}^{r=r_0} \tag{3.31}$$

$$= \frac{\pi}{2\mu} \frac{dp}{dz} \left[\frac{r_0^4}{2} - \frac{r_0^4}{4} \right] = \frac{\pi r_0^4}{8\mu} \frac{dp}{dz}. \tag{3.32}$$

Taking the change in pressure over the length of the pipe, $dp \to \Delta P$ and $dz \to L$,

$$\Rightarrow Q = \frac{\pi r_0^4}{8\mu} \frac{\Delta P}{L} \tag{3.33}$$

where $\Delta P > 0$. This is a familiar result for a circular pipe. Importantly, it tells us that the volumetric flux is simply the integration of the velocity profile over the area through which the fluid passes.

3.5.4.2 Rectangular Pipe in 3D

Consider first the case of a rectangular pipe in 3D. The 2D case will easily follow from this discussion. We will make use of the coordinate system shown in Figure 3.11.

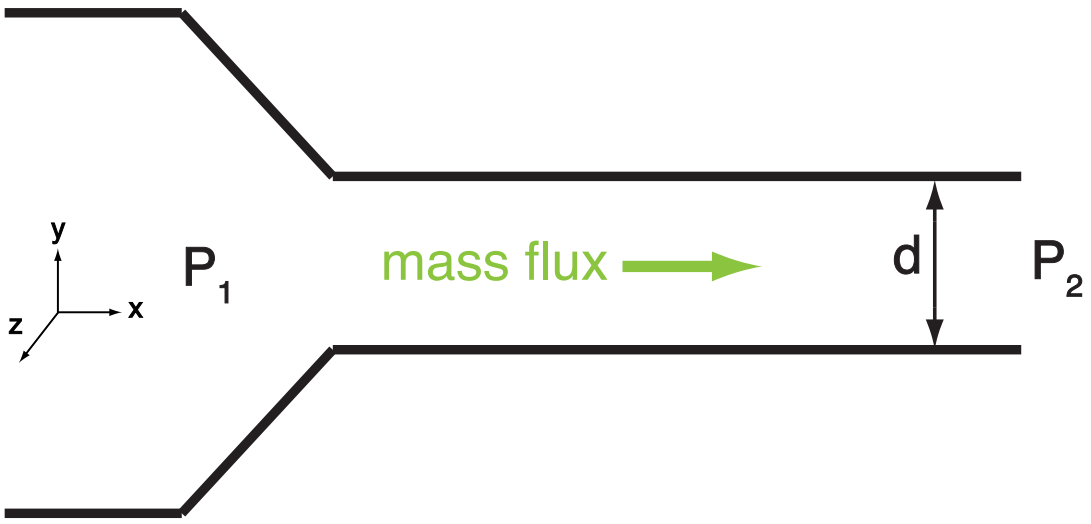

Figure 3.11: Geometry for Hagen-Poiseuille derivation. The membrane is parallel to the x, z plane. The pressure P_2 is taken to be less than P_1, and the mass flux therefore flows in the $\hat{x}$ direction.

The y and z velocity components are independent of time, and

$$v_y = v_z = 0 \tag{3.34}$$

$$\Rightarrow \frac{\partial v_y}{\partial y} + \frac{\partial v_z}{\partial z} = 0. \tag{3.35}$$

Requiring mass continuity or mass conservation (§3.5.5),

$$\frac{\partial v_x}{\partial x} = 0 \tag{3.36}$$

and by Navier-Stokes for an incompressible fluid (§3.5.6)

$$-\frac{\partial P}{\partial x} + \mu \frac{\partial^2 v_x}{\partial y^2} = 0 \tag{3.37}$$

$$\Rightarrow \frac{\partial P}{\partial x} = \mu \frac{\partial^2 v_x}{\partial y^2}. \tag{3.38}$$

The gradient of the pressure must be equal to a constant, so we must have

$$\frac{\partial P}{\partial x} = c_1 \Rightarrow P = c_1 x + c_2. \tag{3.39}$$

Use the boundary conditions

$$x = 0 \qquad P = P_1 \Rightarrow c_2 = P_1 \tag{3.40}$$

$$x = L \qquad P = P_2 \Rightarrow c_1 = -\frac{P_1 - P_2}{L} = -\frac{\Delta P}{L} \tag{3.41}$$

$$\Rightarrow P = P_1 - \frac{\Delta P}{L} x \tag{3.42}$$

$$\Rightarrow \frac{\partial P}{\partial x} = -\frac{\Delta P}{L} \tag{3.43}$$

$$\xRightarrow{\textit{Equation } 3.38} -\frac{\Delta P}{L} = \mu \frac{\partial^2 v_x}{\partial y^2} \Rightarrow \frac{\partial^2 v_x}{\partial y^2} = -\frac{\Delta P}{\mu L} \tag{3.44}$$

$$\Rightarrow \frac{\partial v_x}{\partial y} = -\frac{\Delta P}{\mu L} y + c_3 \tag{3.45}$$

$$\Rightarrow v_x = -\frac{\Delta P}{2\mu L} y^2 + c_3 y + c_4. \tag{3.46}$$

Using no slip boundary conditions, $v_x(y = d/2) = 0$, $v_x(y = -d/2) = 0$, (Reference 7, Equations

6.2-9)

$$\Rightarrow 0 = -\frac{\Delta P}{2\mu L}\frac{d^2}{4} + \frac{d}{2}c_3 + c_4 \tag{3.47}$$

$$0 = -\frac{\Delta P}{2\mu L}\frac{d^2}{4} - \frac{d}{2}c_3 + c_4 \tag{3.48}$$

$$\xRightarrow{\textit{Equation 3.47+Equation 3.48}} C_4 = \frac{\Delta P}{2\mu L}\frac{d^2}{4} \tag{3.49}$$

$$\xRightarrow{\textit{Equation 3.47}-\textit{Equation 3.48}} C_3 = 0 \tag{3.50}$$

$$\Rightarrow v_x = -\frac{\Delta P}{2\mu L}y^2 + \frac{\Delta P}{\mu L}\frac{d^2}{4} = \frac{\Delta P}{2\mu L}\left[\frac{d^2}{4} - y^2\right] \tag{3.51}$$

$$\Rightarrow v_x = \frac{\Delta P}{2\mu L}\left[\frac{d^2}{4} - y^2\right] \tag{3.52}$$

which is the well-known result predicing a parabolic velocity profile.[7] Integrating the velocity profile to find the flow rate,

$$Q = \int_{-d/2}^{d/2} v_x(y)\, dy \int_0^w dz\ [=]\frac{volume}{time} \tag{3.53}$$

$$\Rightarrow Q = w\int_{-d/2}^{d/2} dy\ v_x(y) = w\int_{-d/2}^{d/2} dy \left\{\frac{\Delta P}{2\mu L}\left[\frac{d^2}{4} - y^2\right]\right\} \tag{3.54}$$

$$= w\frac{\Delta P}{2\mu L}\left\{\frac{d^2}{4}\left[\left(\frac{d}{2}\right) - \left(\frac{-d}{2}\right)\right] - \frac{y^3}{3}\Big|_{y=-d/2}^{y=d/2}\right\} = w\frac{\Delta P}{2\mu L}\left\{\frac{d^3}{4} - \left[\frac{(d/2)^3}{3} - \frac{(-d/2)^3}{3}\right]\right\} \tag{3.55}$$

$$= w\frac{\Delta P}{12\mu L}d^3 \tag{3.56}$$

$$\Rightarrow \Delta P = \frac{12\mu L}{d^3 w}Q \tag{3.57}$$

where w is the width of the rectangular pipe in the z dimension. Averaging Q by the cross-sectional area, $w \times d$,

$$\Rightarrow Q = \frac{\Delta P d^2}{12\mu L} \tag{3.58}$$

$$\Rightarrow \Delta P = \frac{12\mu L}{d^2}Q. \tag{3.59}$$

This result for a rectangular pipe is known (Reference 39, Equation 7). Taking a look at units, note

$$Q[=]\frac{(Pressure)\left(length^2\right)}{(Pressure\ time)\,(length)} = \frac{length}{time}. \tag{3.60}$$

3.5.4.3 Rectangular Pipe in 2D

The results for fluid flow through a two-dimensional pipe are identical up to Equation 3.52, again we predict for the velocity profile (Reference 7, Equations 6.2-9)

$$\Rightarrow v_x = \frac{\Delta P}{2\mu L}\left[\frac{d^2}{4} - y^2\right]. \tag{3.61}$$

Integrate the velocity profile and average over the channel width (was cross-sectional area in 3D),

$$\Rightarrow Q = \frac{1}{d}\int_{-d/2}^{d/2} v_x(y)\, dy = \frac{1}{d}\left(\frac{\Delta P}{12\mu L} d^3\right) \tag{3.62}$$

$$\Rightarrow Q = \frac{\Delta P}{12\mu L} d^2 [=] \frac{(Pressure)}{(Pressure\ time)\,(length)}\left(length^2\right) = \frac{length}{time} \tag{3.63}$$

$$\Rightarrow \Delta P = \frac{12\mu L}{d^2} Q, \tag{3.64}$$

which is the same as the 3D case (Equation (3.60)).

3.5.5 Continuity Equation for Mass Conservation

The continuity equation is a statement of mass balance. The mass continuity can be written using the following train of thought,[13] the total mass in a prescribed volume is written

$$M = \int_V d\mathbf{r}\, \rho(\mathbf{r}, t). \tag{3.65}$$

Mass flowing through an enclosed surface is the velocity times the density (Reference 13, Equation 2.2),

$$\frac{dM}{dt} = -\int_S d\mathbf{S} \cdot \rho(\mathbf{r}, t)\, \mathbf{u}(\mathbf{r}, t) = -\int_V d\mathbf{r}\, \nabla \cdot [\rho(\mathbf{r}, t)\, \mathbf{u}(\mathbf{r}, t)], \tag{3.66}$$

where the divergence theorem has been used. An alternative way to write the change in density is (Reference 13, Equation 2.3)

$$\frac{dM}{dt} = \int_V d\mathbf{r} \frac{\partial \rho(\mathbf{r}, t)}{\partial t}. \tag{3.67}$$

Using the preceding, we can equate (Reference 13, Equation 2.4)

$$\frac{\partial \rho(\mathbf{r},t)}{\partial t} = -\nabla\cdot\left[\rho(\mathbf{r},t)\,\mathbf{u}(\mathbf{r},t)\right] \tag{3.68}$$

$$\Rightarrow \frac{\partial \rho(\mathbf{r},t)}{\partial t} + \nabla\cdot\left[\rho(\mathbf{r},t)\,\mathbf{u}(\mathbf{r},t)\right] = 0 \tag{3.69}$$

$$\Rightarrow \frac{\partial \rho(\mathbf{r},t)}{\partial t} + \nabla\cdot\mathbf{J} = 0 \tag{3.70}$$

where we defined the flux, $\mathbf{J} = \rho(\mathbf{r},t)\,\mathbf{u}(\mathbf{r},t)$. Manipulating these equations more,

$$\frac{\partial \rho}{\partial t} + \nabla\cdot\mathbf{J} = 0$$

$$= \frac{\partial \rho}{\partial t} + \nabla\cdot(\rho\mathbf{v}) = 0$$

$$= \frac{\partial \rho}{\partial t} + \nabla\rho\cdot\mathbf{v} + \rho\nabla\cdot\mathbf{v} = 0 \tag{3.71}$$

$$= \frac{\partial \rho}{\partial t} + \left(\frac{\partial \rho}{\partial x}v_x + \frac{\partial \rho}{\partial y}v_y + \frac{\partial \rho}{\partial z}v_z\right) + \left(\rho\frac{\partial v_x}{\partial x} + \rho\frac{\partial v_y}{\partial y} + \rho\frac{\partial v_z}{\partial z}\right) = 0. \tag{3.72}$$

The total derivative of the density reads

$$\frac{d\rho}{dt} = \frac{\partial \rho}{\partial t} + \frac{\partial \rho}{\partial x}\frac{\partial x}{\partial t} + \frac{\partial \rho}{\partial y}\frac{\partial y}{\partial t} + \frac{\partial \rho}{\partial z}\frac{\partial z}{\partial t} \tag{3.73}$$

$$= \frac{\partial \rho}{\partial t} + \nabla\rho\cdot\mathbf{v}. \tag{3.74}$$

For an incompressible fluid

$$\frac{d\rho}{dt} = 0 \tag{3.75}$$

$$\Rightarrow \frac{\partial \rho}{\partial t} = -\nabla\rho\cdot\mathbf{v} \tag{3.76}$$

$$\Rightarrow \rho\nabla\cdot\mathbf{v} = 0 \tag{3.77}$$

$$\Rightarrow \nabla\cdot\mathbf{v} = 0 \tag{3.78}$$

$$\Rightarrow \frac{\partial v_x}{\partial x} + \frac{\partial v_y}{\partial y} + \frac{\partial v_z}{\partial z} = 0. \tag{3.79}$$

We note that in the above, for an incompressible fluid,

$$\nabla\cdot\mathbf{v} = 0. \tag{3.80}$$

If the density in a volume element changed with time, this would have meant that the fluid compressed or expanded, which would then be properly termed a compressible fluid.

3.5.6 Navier-Stokes

The Navier-Stokes equation in Cartesian coordinates, for the x component reads (Table 5-7 of Reference 7),

$$\rho\left[\frac{\partial v_x}{\partial t} + v_x\frac{\partial v_x}{\partial x} + v_y\frac{\partial v_x}{\partial y} + v_z\frac{\partial v_x}{\partial z}\right] = \rho f_x - \frac{\partial P}{\partial x} + \mu\left[\frac{\partial^2 v_x}{\partial x^2} + \frac{\partial^2 v_y}{\partial y^2} + \frac{\partial^2 v_z}{\partial z^2}\right]. \tag{3.81}$$

For all of our simulations, we will consider flow in the x direction. We have $v_y = v_z = \frac{\partial v_x}{\partial t} = 0$, and so

$$\Rightarrow \frac{\partial P}{\partial x} = \mu\frac{\partial^2 v_x}{\partial x^2}, \tag{3.82}$$

having set the external force, $f_x = 0$. If this were included, it would simply be a constant shift.

Bibliography

[1] L. A. Baker and S. P. Bird. Nanopores: A makeover for membranes. Nat. Nanotechnol., 3(2):73–74, 2008.

[2] C. O. Bennett and J. E. Myers. Momentum, heat, and mass transfer. McGraw-Hill New York, 1982.

[3] S. Bernardi, B. Todd, and D. J. Searles. Thermostating highly confined fluids. J. Chem. Phys., 132(24):244706, 2010.

[4] D. Chandler, J. D. Weeks, and H. C. Andersen. Van der waals picture of liquids, solids, and phase transformations. Science, 220(4599):787–794, 1983.

[5] D. Cohen-Tanugi and J. Grossman. Water desalination across nanoporous graphene. Nano Lett., 12(7):3602–3608, 2012.

[6] R. F. Cracknell, D. Nicholson, and N. Quirke. Direct molecular dynamics simulation of flow down a chemical potential gradient in a slit-shaped micropore. Phys. Rev. Lett., 74(13):2463, 1995.

[7] W. M. Deen. Analysis of transport phenomena, volume 3. Oxford University Press, New York, 1998.

[8] A. M. . T. D.J. Computer simulation of liquids. Oxford University Press: New York, 1989.

[9] R. Edberg, D. J. Evans, and G. Morriss. Constrained molecular dynamics: Simulations of liquid alkanes with a new algorithm. J. Chem. Phys., 84(12):6933–6939, 1986.

[10] D. J. Evans and B. L. Holian. The nose–hoover thermostat. J. Chem. Phys., 83(8):4069–4074, 1985.

[11] D. J. Evans, W. G. Hoover, B. H. Failor, B. Moran, and A. J. Ladd. Nonequilibrium molecular dynamics via gauss's principle of least constraint. Phys. Rev. A, 28(2):1016, 1983.

[12] D. J. Evans and G. Morriss. Isothermal-isobaric molecular dynamics. Chem. Phys., 77(1):63–66, 1983.

[13] D. J. Evans and G. Morriss. Statistical mechanics of nonequilibrium liquids. Cambridge University Press, 2008.

[14] D. J. Evans and G. P. Morriss. Shear thickening and turbulence in simple fluids. Phys. Rev. Lett., 56(20):2172, 1986.

[15] D. Frenkel and B. Smit. Understanding molecular simulation: from algorithms to applications. Acadmic Press: San Diego, CA, 2001.

[16] H. Frentrup, C. Avendaño, M. Horsch, A. Salih, and E. A. Müller. Transport diffusivities of fluids in nanopores by non-equilibrium molecular dynamics simulation. Molecular Simulation, 38(7):540–553, 2012.

[17] H. Goldstein, C. Poole., and J. Safko. Classical mechanics. Addison Wesley, 2002.

[18] R. D. Groot. A local galilean invariant thermostat. J. Chem. Theory Comput., 2(3):568–574, 2006.

[19] C. C. Harrell, Z. S. Siwy, and C. R. Martin. Conical nanopore membranes: controlling the nanopore shape. Small, 2(2):194–198, 2006.

[20] H. Heinz. Calculation of local and average pressure tensors in molecular simulations. Molecular Simulation, 33(9-10):747–758, 2007.

[21] W. G. Hoover. Canonical dynamics: equilibrium phase-space distributions. Phys. Rev. A, 31(3):1695, 1985.

[22] C. Huang, P. Y. Choi, and L. W. Kostiuk. A method for creating a non-equilibrium NT(P1-P2) ensemble in molecular dynamics simulation. Phys. Chem. Chem. Phys., 13(46):20750–20759, 2011.

[23] J. MacElroy. Nonequilibrium molecular dynamics simulation of diffusion and flow in thin microporous membranes. J. Chem. Phys., 101(6):5274–5280, 1994.

[24] D. McQuarrie. Statistical mechanics. University Science Books: Sausalito, CA, 2000.

[25] B. N. Miles, A. P. Ivanov, K. A. Wilson, F. Doğan, D. Japrung, and J. B. Edel. Single molecule sensing with solid-state nanopores: novel materials, methods, and applications. Chem. Soc. Rev., 42(1):15–28, 2013.

[26] D. R. Mott, E. S. Oran, and C. R. Kaplan. Microfilter simulations and scaling laws. J. Thermophys. Heat Transfer, 15(4):473–477, 2001.

[27] S. Plimpton. Fast parallel algorithms for short-range molecular dynamics. J. Comput. Phys., 117(1):1–19, 1995.

[28] V. Priymak and T. Miyazaki. Accurate navier–stokes investigation of transitional and turbulent flows in a circular pipe. J. Comput. Phys., 142(2):370–411, 1998.

[29] V. Průša. On the influence of boundary condition on stability of hagen–poiseuille flow. Comp. Math. Appl., 57(5):763–771, 2009.

[30] J. R. Ray. Nonholonomic constraints and gauss's principle of least constraint. Am. J. Phys., 40(1):179–183, 1972.

[31] K. K. F. Riley. Mathematical methods for physics and engineering, 3rd edition. Cambridge University Press; New York, 2006.

[32] A. Røsjorde, D. Fossmo, D. Bedeaux, S. Kjelstrup, and B. Hafskjold. Nonequilibrium molecular dynamics simulations of steady-state heat and mass transport in condensation: I. local equilibrium. J. Colloid Interface Sci., 232(1):178–185, 2000.

[33] V. Rühle. Berendsen and nose-hoover thermostats. Am. J. Phys, 2007.

[34] T. Schmidt, M. Zhang, S. Yu, and J. Linnros. Fabrication of ultra-high aspect ratio silicon nanopores by electrochemical etching. Appl. Phys. Lett., 105(12):123111, 2014.

[35] D. Simon and J. McQuarrie. Physical chemistry: a molecular approach. University Science Books: Sausalito, CA, 1997.

[36] A. Subramani, N. Voutchkov, and J. G. Jacangelo. Desalination energy minimization using thin film nanocomposite membranes. Desalination, 350:35–43, 2014.

[37] M. Suk and N. Aluru. Molecular and continuum hydrodynamics in graphene nanopores. RSC Adv., 3(24):9365–9372, 2013.

[38] M. E. Suk and N. Aluru. Water transport through ultrathin graphene. J. Phys. Chem. Lett., 1(10):1590–1594, 2010.

[39] H. Takaba, Y. Onumata, and S.-i. Nakao. Molecular simulation of pressure-driven fluid flow in nanoporous membranes. J. Chem. Phys., 127(5):054703, 2007.

[40] K. P. Travis, B. Todd, and D. J. Evans. Departure from navier-stokes hydrodynamics in confined liquids. Phys. Rev. E, 55(4):4288, 1997.

[41] B. Vujanovic. The practical use of gauss principle of least constraint. Appl. Phys. Lett., 43(3):491–496, 1976.

[42] B. Vujanovic and B. Bačlić. Applications of gauss's principle of least constraint to the nonlinear heat-transfer problem. Int. J. Heat Mass Transfer, 19(7):721–730, 1976.

[43] F. Zhu, E. Tajkhorshid, and K. Schulten. Collective diffusion model for water permeation through microscopic channels. Phys. Rev. Lett., 93(22):224501, 2004.

[44] F. Zhu, E. Tajkhorshid, and K. Schulten. Theory and simulation of water permeation in aquaporin-1. Biophys. J., 86(1):50–57, 2004.

Bibliography

[1] P. W. Atkins and J. De Paula. Physical chemistry. Oxford University Press, Oxford, 1994.

[2] J. L. Baker, A. Widmer-Cooper, M. F. Toney, P. L. Geissler, and A. P. Alivisatos. Device-scale perpendicular alignment of colloidal nanorods. Nano Lett., 10(1):195–201, 2009.

[3] L. A. Baker and S. P. Bird. Nanopores: A makeover for membranes. Nat. Nanotechnol., 3(2):73–74, 2008.

[4] V. Ballenegger, A. Arnold, and J. Cerda. Simulations of non-neutral slab systems with long-range electrostatic interactions in two-dimensional periodic boundary conditions. J. Chem. Phys., 131:094107, 2009.

[5] W. Bao, G. Liu, Z. Zhao, H. Zhang, D. Yan, A. Deshpande, B. LeRoy, and C. N. Lau. Lithography-free fabrication of high quality substrate-supported and freestanding graphene devices. Nano Res., 3(2):98–102, 2010.

[6] W. Bao, K. Myhro, Z. Zhao, Z. Chen, W. Jang, L. Jing, F. Miao, H. Zhang, C. Dames, and C. N. Lau. In situ observation of electrostatic and thermal manipulation of suspended graphene membranes. Nano Lett., 12(11):5470–5474, 2012.

[7] C. O. Bennett and J. E. Myers. Momentum, heat, and mass transfer. McGraw-Hill New York, 1982.

[8] H. Berendsen, J. Grigera, and T. Straatsma. The missing term in effective pair potentials. J. Phys. Chem., 91(24):6269–6271, 1987.

[9] B. Berge and J. Peseux. Variable focal lens controlled by an external voltage: An application of electrowetting. Eur. Phys. J. E, 3(2):159–163, 2000.

[10] S. Bernardi, B. Todd, and D. J. Searles. Thermostating highly confined fluids. J. Chem. Phys., 132(24):244706, 2010.

[11] M. K. Borg, D. A. Lockerby, and J. Reese. Coupled continuum hydrodynamics and molecular dynamics method for multiscale simulation. In 3rd Micro. Nano Flows Conf., MNF11, 2011.

[12] A. W. Bott. Electrochemistry of semiconductors. Curr. Sep., 17:87–92, 1998.

[13] D. Bratko, C. D. Daub, K. Leung, and A. Luzar. Effect of field direction on electrowetting in a nanopore. J. Am. Chem. Soc., 129(9):2504–2510, 2007.

[14] T. Y. Cath, A. E. Childress, and M. Elimelech. Forward osmosis: principles, applications, and recent developments. J. Membr. Sci., 281(1):70–87, 2006.

[15] D. Chandler. Hydrophobicity: Two faces of water. Nature, 417(6888):491–491, 2002.

[16] D. Chandler, J. D. Weeks, and H. C. Andersen. Van der waals picture of liquids, solids, and phase transformations. Science, 220(4599):787–794, 1983.

[17] D. Cohen-Tanugi and J. Grossman. Water desalination across nanoporous graphene. Nano Lett., 12(7):3602–3608, 2012.

[18] D. Cohen-Tanugi and J. C. Grossman. Water permeability of nanoporous graphene at realistic pressures for reverse osmosis desalination. J. Chem. Phys., 141(7):074704, 2014.

[19] D. Cohen-Tanugi, R. K. McGovern, S. H. Dave, J. H. Lienhard, and J. C. Grossman. Quantifying the potential of ultra-permeable membranes for water desalination. Energy Environ. Sci., 7(3):1134–1141, 2014.

[20] M. Craciun, S. Russo, M. Yamamoto, and S. Tarucha. Tuneable electronic properties in graphene. Nano Today, 6(1):42–60, 2011.

[21] R. F. Cracknell, D. Nicholson, and N. Quirke. Direct molecular dynamics simulation of flow down a chemical potential gradient in a slit-shaped micropore. Phys. Rev. Lett., 74(13):2463, 1995.

[22] T. Cramer, F. Zerbetto, and R. García. Molecular mechanism of water bridge buildup: Field-induced formation of nanoscale menisci. Langmuir, 24(12):6116–6120, 2008.

[23] S. Das Sarma, S. Adam, E. H. Hwang, and E. Rossi. Electronic transport in two-dimensional graphene. Rev. Mod. Phys., 83:407–470, May 2011.

[24] C. Daub, D. Bratko, and A. Luzar. Electric control of wetting by salty nanodrops: Molecular dynamics simulations. J. Phys. Chem. C, 115(45):22393–22399, 2011.

[25] C. D. Daub, D. Bratko, K. Leung, and A. Luzar. Electrowetting at the nanoscale. J. Phys. Chem. C, 111(2):505–509, 2007.

[26] W. M. Deen. Analysis of transport phenomena, volume 3. Oxford University Press, New York, 1998.

[27] M. Deserno and C. Holm. How to mesh up ewald sums. ii. an accurate error estimate for the particle–particle–particle-mesh algorithm. J. Chem. Phys., 109:7694–7701, 1998.

[28] A. M. . T. D.J. Computer simulation of liquids. Oxford University Press: New York, 1989.

[29] X. Du, I. Skachko, A. Barker, and E. Y. Andrei. Approaching ballistic transport in suspended graphene. Nat. Nanotechnol., 3(8):491–495, 2008.

[30] J. D. Eaves, A. Tokmakoff, and P. L. Geissler. Electric field fluctuations drive vibrational dephasing in water. J. Phys. Chem. A, 109(42):9424–9436, 2005.

[31] R. Edberg, D. J. Evans, and G. Morriss. Constrained molecular dynamics: Simulations of liquid alkanes with a new algorithm. J. Chem. Phys., 84(12):6933–6939, 1986.

[32] B. Efron. The jackknife, the bootstrap and other resampling plans. Society for Industrial and Applied Mathematics: Philadelphia, 1982.

[33] M. Elimelech and W. A. Phillip. The future of seawater desalination: energy, technology, and the environment. Science, 333(6043):712–717, 2011.

[34] D. J. Evans and B. L. Holian. The nose–hoover thermostat. J. Chem. Phys., 83(8):4069–4074, 1985.

[35] D. J. Evans, W. G. Hoover, B. H. Failor, B. Moran, and A. J. Ladd. Nonequilibrium molecular dynamics via gauss's principle of least constraint. Phys. Rev. A, 28(2):1016, 1983.

[36] D. J. Evans and G. Morriss. Isothermal-isobaric molecular dynamics. Chem. Phys., 77(1):63–66, 1983.

[37] D. J. Evans and G. Morriss. Statistical mechanics of nonequilibrium liquids. Cambridge University Press, 2008.

[38] D. J. Evans and G. P. Morriss. Shear thickening and turbulence in simple fluids. Phys. Rev. Lett., 56(20):2172, 1986.

[39] D. B. Farmer, R. Golizadeh-Mojarad, V. Perebeinos, Y.-M. Lin, G. S. Tulevski, J. C. Tsang, and P. Avouris. Chemical doping and electron-hole conduction asymmetry in graphene devices. Nano Lett., 9(1):388–392, 2008.

[40] M. Ferrario, M. Haughney, I. R. McDonald, and M. L. Klein. Molecular-dynamics simulation of aqueous mixtures: Methanol, acetone, and ammonia. J. Chem. Phys., 93:5156, 1990.

[41] M. W. Feyereisen, D. Feller, and D. A. Dixon. Hydrogen bond energy of the water dimer. J. Phys. Chem., 100(8):2993–2997, 1996.

[42] F. Fowkes and W. Harkins. The state of monolayers adsorbed at the interface solid-aqueous solution. J. Am. Chem. Soc., 62(12):3377–3386, 1940.

[43] I. Frank, D. M. Tanenbaum, A. Van der Zande, and P. L. McEuen. Mechanical properties of suspended graphene sheets. J. Vac. Sci. Technol. B, 25(6):2558–2561, 2007.

[44] D. Frenkel and B. Smit. Understanding molecular simulation: from algorithms to applications. Acadmic Press: San Diego, CA, 2001.

[45] H. Frentrup, C. Avendaño, M. Horsch, A. Salih, and E. A. Müller. Transport diffusivities of fluids in nanopores by non-equilibrium molecular dynamics simulation. Molecular Simulation, 38(7):540–553, 2012.

[46] C. Fritzmann, J. Löwenberg, T. Wintgens, and T. Melin. State-of-the-art of reverse osmosis desalination. Desalination, 216(1):1–76, 2007.

[47] Q. Ge, M. Ling, and T.-S. Chung. Draw solutions for forward osmosis processes: developments, challenges, and prospects for the future. J. Membr. Sci., 442:225–237, 2013.

[48] A. M. Gilau and M. J. Small. Designing cost-effective seawater reverse osmosis system under optimal energy options. Renewable Energy, 33(4):617–630, 2008.

[49] N. Giovambattista, P. G. Debenedetti, and P. J. Rossky. Effect of surface polarity on water contact angle and interfacial hydration structure. J. Phys. Chem. B, 111(32):9581–9587, 2007.

[50] R. Godawat, S. N. Jamadagni, and S. Garde. Characterizing hydrophobicity of interfaces by using cavity formation, solute binding, and water correlations. Proc. Natl. Acad. Sci. USA, 106(36):15119–15124, 2009.

[51] H. Goldstein, C. Poole., and J. Safko. Classical mechanics. Addison Wesley, 2002.

[52] L. F. Greenlee, D. F. Lawler, B. D. Freeman, B. Marrot, and P. Moulin. Reverse osmosis desalination: water sources, technology, and today's challenges. Water Research, 43(9):2317–2348, 2009.

[53] D. J. Griffiths. Introduction to electrodynamics, 3rd edition. Pearson, 2005.

[54] R. D. Groot. A local galilean invariant thermostat. J. Chem. Theory Comput., 2(3):568–574, 2006.

[55] J. Han, J. Fu, and R. B. Schoch. Molecular sieving using nanofilters: past, present and future. Lab Chip, 8(1):23–33, 2008.

[56] J.-P. Hansen and I. R. McDonald. Theory of simple liquids, 3rd edition. Academic Press: Amsterdam, 1990.

[57] C. C. Harrell, Z. S. Siwy, and C. R. Martin. Conical nanopore membranes: controlling the nanopore shape. Small, 2(2):194–198, 2006.

[58] R. A. Hayes and B. Feenstra. Video-speed electronic paper based on electrowetting. Nature, 425(6956):383–385, 2003.

[59] H. Heinz. Calculation of local and average pressure tensors in molecular simulations. Molecular Simulation, 33(9-10):747–758, 2007.

[60] T. Ho and A. Striolo. Polarizability effects in molecular dynamics simulations of the graphene-water interface. J. Chem. Phys., 138:054117, 2013.

[61] R. W. Hockney and J. W. Eastwood. Computer simulation using particles. McGraw-Hill: New York, 1981.

[62] P. Hoogerbrugge and J. Koelman. Simulating microscopic hydrodynamic phenomena with dissipative particle dynamics. Europhys. Lett., 19(3):155, 1992.

[63] W. G. Hoover. Canonical dynamics: equilibrium phase-space distributions. Phys. Rev. A, 31(3):1695, 1985.

[64] C. Huang, P. Y. Choi, and L. W. Kostiuk. A method for creating a non-equilibrium NT(P1-P2) ensemble in molecular dynamics simulation. Phys. Chem. Chem. Phys., 13(46):20750–20759, 2011.

[65] J. D. Jackson. Classical electrodynamics, 3 edition. Wiley, 1999.

[66] J. Johnson and M. Busch. Engineering aspects of reverse osmosis module design. Desalin. Water Treat., 15(1-3):236–248, 2010.

[67] T. Z. Jubery, A. S. Prabhu, M. J. Kim, and P. Dutta. Modeling and simulation of nanoparticle separation through a solid-state nanopore. Electrophoresis, 33(2):325–333, 2012.

[68] G. Karniadakis, A. Beskok, and N. Aluru. Microflows and nanoflows: fundamentals and simulation, volume 29. Springer, 2006.

[69] C. Kittel. Introduction to solid state physics, 7th edition. Wiley: New York, 1996.

[70] S. P. Koenig, L. Wang, J. Pellegrino, and J. S. Bunch. Selective molecular sieving through porous graphene. Nat. Nanotechnol., 7(11):728–732, 2012.

[71] J. Köfinger, G. Hummer, and C. Dellago. Single-file water in nanopores. Phys. Chem. Chem. Phys., 13(34):15403–15417, 2011.

[72] A. Lafuma and D. Quéré. Superhydrophobic states. Nat. Mater., 2(7):457–460, 2003.

[73] C. N. Lau, W. Bao, and J. Velasco. Properties of suspended graphene membranes. Mater. Today, 15(6):238–245, 2012.

[74] C.-P. Lee, B.-Y. Fang, and Z.-H. Wei. Influence of electrolytes on contact angles of droplets under electric field. Analyst, 138(8):2372–2377, 2013.

[75] H. Li, T. Lu, L. Pan, Y. Zhang, and Z. Sun. Electrosorption behavior of graphene in nacl solutions. J. Mater. Chem., 19(37):6773–6779, 2009.

[76] Y.-M. Lin, H.-Y. Chiu, K. A. Jenkins, D. B. Farmer, P. Avouris, and A. Valdes-Garcia. Dual-gate graphene fets with f_T of 50 ghz. IEEE Electron Device Lett., 31(1):68–70, 2010.

[77] H. Liu, Y. Liu, and D. Zhu. Chemical doping of graphene. J. Mater. Chem., 21(10):3335–3345, 2011.

[78] H. K. Lonsdale. The evolution of ultrathin synthetic membranes. J. Membr. Sci., 33(2):121–136, 1987.

[79] J. MacElroy. Nonequilibrium molecular dynamics simulation of diffusion and flow in thin microporous membranes. J. Chem. Phys., 101(6):5274–5280, 1994.

[80] R. A. Marcus. Electron transfer reactions in chemistry. theory and experiment. Rev. Mod. Phys., 65(3):599–610, 1993.

[81] D. McQuarrie. Statistical mechanics. University Science Books: Sausalito, CA, 2000.

[82] I. Meric, M. Y. Han, A. F. Young, B. Ozyilmaz, P. Kim, and K. L. Shepard. Current saturation in zero-bandgap, top-gated graphene field-effect transistors. Nat. Nanotechnol., 3(11):654–659, Nov 2008.

[83] B. N. Miles, A. P. Ivanov, K. A. Wilson, F. Doğan, D. Japrung, and J. B. Edel. Single molecule sensing with solid-state nanopores: novel materials, methods, and applications. Chem. Soc. Rev., 42(1):15–28, 2013.

[84] E. Moeendarbary, T. Ng, and M. Zangeneh. Dissipative particle dynamics: introduction, methodology and complex fluid applicationsa review. Int. J. Appl. Mech., 1(04):737–763, 2009.

[85] H. Moon, S. Cho, R. Garrell, and C.-J. Kim. Low voltage electrowetting-on-dielectric. J. Appl. Phys., 92(7):4080–4087, 2002.

[86] D. R. Mott, E. S. Oran, and C. R. Kaplan. Microfilter simulations and scaling laws. J. Thermophys. Heat Transfer, 15(4):473–477, 2001.

[87] F. Mugele and J.-C. Baret. Electrowetting: from basics to applications. J. Phys. Condens. Matter, 17(28):R705–R774, 2005.

[88] W. Nelson and C.-J. Kim. Droplet actuation by electrowetting-on-dielectric (ewod): A review. J. Adhes. Sci. Technol., 26(12-17):1747–1771, 2012.

[89] A. Neto, F. Guinea, N. Peres, K. Novoselov, and A. Geim. The electronic properties of graphene. Rev. Mod. Phys., 81(1):109–162, 2009.

[90] R. A. Nicodemus, S. Corcelli, J. Skinner, and A. Tokmakoff. Collective hydrogen bond reorganization in water studied with temperature-dependent ultrafast infrared spectroscopy. J. Phys. Chem. B, 115(18):5604–5616, 2011.

[91] A. Nicolaï, B. G. Sumpter, and V. Meunier. Tunable water desalination across graphene oxide framework membranes. Phys. Chem. Chem. Phys., 16(18):8646–8654, 2014.

[92] K. S. Novoselov, A. K. Geim, S. Morozov, D. Jiang, Y. Zhang, S. Dubonos, I. Grigorieva, and A. Firsov. Electric field effect in atomically thin carbon films. Science, 306(5696):666–669, 2004.

[93] J. H. Ostrowski and J. D. Eaves. The tunable hydrophobic effect on electrically doped graphene. J. Phys. Chem. B, 118(2):530–536, 2014.

[94] L. Panchakarla, K. Subrahmanyam, S. Saha, A. Govindaraj, H. Krishnamurthy, U. Waghmare, and C. Rao. Synthesis, structure, and properties of boron-and nitrogen-doped graphene. Adv. Mater., 21(46):4726–4730, 2009.

[95] S. Plimpton. Fast parallel algorithms for short-range molecular dynamics. J. Comput. Phys., 117(1):1–19, 1995.

[96] A. S. Prabhu, T. Z. N. Jubery, K. J. Freedman, R. Mulero, P. Dutta, and M. J. Kim. Chemically modified solid state nanopores for high throughput nanoparticle separation. J. Phys. Condens. Matter, 22(45):454107, 2010.

[97] V. Priymak and T. Miyazaki. Accurate navier–stokes investigation of transitional and turbulent flows in a circular pipe. J. Comput. Phys., 142(2):370–411, 1998.

[98] V. Pr*ůša*. On the influence of boundary condition on stability of hagen–poiseuille flow. Comp. Math. Appl., 57(5):763–771, 2009.

[99] T. Qian and X.-P. Wang. Driven cavity flow: from molecular dynamics to continuum hydrodynamics. Multiscale Model. Simul., 3(4):749–763, 2005.

[100] J. Rafiee, X. Mi, H. Gullapalli, A. V. Thomas, F. Yavari, Y. Shi, P. M. Ajayan, and N. A. Koratkar. Wetting transparency of graphene. Nat. Mater., 11(3):217–222, 2012.

[101] J. R. Ray. Nonholonomic constraints and gauss's principle of least constraint. Am. J. Phys., 40(1):179–183, 1972.

[102] K. K. F. Riley. Mathematical methods for physics and engineering, 3rd edition. Cambridge University Press; New York, 2006.

[103] A. Røsjorde, D. Fossmo, D. Bedeaux, S. Kjelstrup, and B. Hafskjold. Nonequilibrium molecular dynamics simulations of steady-state heat and mass transport in condensation: I. local equilibrium. J. Colloid Interface Sci., 232(1):178–185, 2000.

[104] P. Roura and J. Fort. Local thermodynamic derivation of young's equation. J. Colloid Interface Sci., 272(2):420–429, 2004.

[105] V. Rühle. Berendsen and nose-hoover thermostats. Am. J. Phys, 2007.

[106] F. Rupp, L. Scheideler, N. Olshanska, M. De Wild, M. Wieland, and J. Geis-Gerstorfer. Enhancing surface free energy and hydrophilicity through chemical modification of microstructured titanium implant surfaces. J. Biomed. Mater. Res., Part A, 76(2):323–334, 2006.

[107] T. Schmidt, M. Zhang, S. Yu, and J. Linnros. Fabrication of ultra-high aspect ratio silicon nanopores by electrochemical etching. Appl. Phys. Lett., 105(12):123111, 2014.

[108] N. Shenogina, R. Godawat, P. Keblinski, and S. Garde. How wetting and adhesion affect thermal conductance of a range of hydrophobic to hydrophilic aqueous interfaces. Phys. Rev. Lett., 102(15):156101, 2009.

[109] G. B. Sigal, M. Mrksich, and G. M. Whitesides. Effect of surface wettability on the adsorption of proteins and detergents. J. Am. Chem. Soc., 120(14):3464–3473, 1998.

[110] D. Simon and J. McQuarrie. Physical chemistry: a molecular approach. University Science Books: Sausalito, CA, 1997.

[111] V. Srinivasan, V. K. Pamula, and R. B. Fair. An integrated digital microfluidic lab-on-a-chip for clinical diagnostics on human physiological fluids. Lab Chip, 4(4):310–315, 2004.

[112] A. Subramani, N. Voutchkov, and J. G. Jacangelo. Desalination energy minimization using thin film nanocomposite membranes. Desalination, 350:35–43, 2014.

[113] M. Suk and N. Aluru. Molecular and continuum hydrodynamics in graphene nanopores. RSC Adv., 3(24):9365–9372, 2013.

[114] M. E. Suk and N. Aluru. Water transport through ultrathin graphene. J. Phys. Chem. Lett., 1(10):1590–1594, 2010.

[115] H. Takaba, Y. Onumata, and S.-i. Nakao. Molecular simulation of pressure-driven fluid flow in nanoporous membranes. J. Chem. Phys., 127(5):054703, 2007.

[116] X. Tan, J. Yang, P. Zeng, E. Kim, C. Huard, and M. Cheng. Electrowetting on flexible, transparent and conducting single-layer graphene. IEEE 25th Int. Conf. MEMS, pages 1037–1040, 2012.

[117] X. Tan, Z. Zhou, and M. M.-C. Cheng. Electrowetting on dielectric experiments using graphene. Nanotechnology, 23(37):375501, 2012.

[118] B. Toshev. Gibbs' thermodynamics of wetting. Int. J. Mech. Eng. Edu., 34(3):256–262, 2006.

[119] K. P. Travis, B. Todd, and D. J. Evans. Departure from navier-stokes hydrodynamics in confined liquids. Phys. Rev. E, 55(4):4288, 1997.

[120] K. Vetter. Electrochemical kinetics: theoretical and experimental aspects. Academic Press: New York, 1967.

[121] B. Vujanovic. The practical use of gauss principle of least constraint. Appl. Phys. Lett., 43(3):491–496, 1976.

[122] B. Vujanovic and B. Bačlić. Applications of gauss's principle of least constraint to the nonlinear heat-transfer problem. Int. J. Heat Mass Transfer, 19(7):721–730, 1976.

[123] P. B. Warren. Dissipative particle dynamics. Curr. Opin. Colloid Interface Sci., 3(6):620–624, 1998.

[124] T. Werder, J. Walther, R. Jaffe, T. Halicioglu, and P. Koumoutsakos. On the water-carbon interaction for use in molecular dynamics simulations of graphite and carbon nanotubes. J. Phys. Chem. B, 107(6):1345–1352, 2003.

[125] A. R. Wheeler. Putting electrowetting to work. Science, 322(5901):539–540, 2008.

[126] A. P. Willard and D. Chandler. Instantaneous liquid interfaces. J. Phys. Chem. B, 114(5):1954–1958, 2010.

[127] A. P. Willard and D. Chandler. The molecular structure of the interface between water and a hydrophobic substrate is liquid-vapor like. J. Chem. Phys., 141(18):18C519, 2014.

[128] P. Xu, Y. Yang, S. Barber, M. Ackerman, J. Schoelz, I. A. Kornev, S. Barraza-Lopez, L. Bellaiche, and P. Thibado. Giant surface charge density of graphene resolved from scanning tunneling microscopy and first-principles theory. Phys. Rev. B, 84(16):161409, 2011.

[129] I.-C. Yeh and M. Berkowitz. Ewald summation for systems with slab geometry. J. Chem. Phys., 111(7):3155–3162, 1999.

[130] T. Young. An essay on the cohesion of fluids. Philos. Trans. R. Soc. London, 95:65–87, 1805.

[131] Q. Zaib and H. Fath. Application of carbon nano-materials in desalination processes. Desalin. Water Treat., 51(1-3):627–636, 2013.

[132] L. Zhao, R. He, K. Rim, T. Schiros, K. Kim, H. Zhou, C. Gutiérrez, S. Chockalingam, C. Arguello, L. Pálová, D. Nordlund, M. Hybertsen, D. Reichman, T. Heinz, P. Kim, A. Pinczuk, G. Flynn, and A. Pasupathy. Visualizing individual nitrogen dopants in monolayer graphene. Science, 333(6045):999–1003, 2011.

[133] F. Zhu, E. Tajkhorshid, and K. Schulten. Collective diffusion model for water permeation through microscopic channels. Phys. Rev. Lett., 93(22):224501, 2004.

[134] F. Zhu, E. Tajkhorshid, and K. Schulten. Theory and simulation of water permeation in aquaporin-1. Biophys. J., 86(1):50–57, 2004.